

Dual-polarization (HH/HV) RADARSAT-2
ScanSAR Observations of New, Young and First-
year Sea Ice

by

John Alexander Casey

A thesis
presented to the University of Waterloo
in fulfillment of the
thesis requirement for the degree of
Master of Science
in
Geography

Waterloo, Ontario, Canada, 2010

©John Alexander Casey 2010

AUTHOR'S DECLARATION

I hereby declare that I am the sole author of this thesis. This is a true copy of the thesis, including any required final revisions, as accepted by my examiners.

I understand that my thesis may be made electronically available to the public.

Abstract

Observations of sea ice from space are routinely used to monitor sea ice extent, concentration and type to support human marine activity and climate change studies. In this study, eight dual-polarization (dual-pol) (HH/HV) RADARSAT-2 ScanSAR images acquired over the Gulf of St. Lawrence during the winter of 2009 are analysed to determine what new or improved sea ice information is provided by dual-pol C-band synthetic aperture radar (SAR) data at wide swath widths, relative to single co-pol data. The objective of this study is to assess how dual-pol RADARSAT-2 ScanSAR data might improve operational ice charts and derived sea ice climate data records. In order to evaluate the dual-pol data, ice thickness and surface roughness measurements and optical remote sensing data were compared to backscatter signatures observed in the SAR data. The study found that: i) dual-pol data provide improved separation of ice and open water, particularly at steep incidence angles and high wind speeds; ii) the contrast between new, young and first-year (FY) ice types is reduced in the cross-pol channel; and iii) large areas of heavily deformed ice can reliably be separated from level ice in the dual-pol data, but areas of light and moderately ridged ice cannot be resolved and the thickness of heavily deformed ice cannot be determined. These results are limited to observations of new, young and FY ice types in winter conditions. From an operational perspective, the improved separation of ice and open water will increase the accuracy of ice edge and total ice concentration estimates while reducing the time required to produce image analysis charts. Further work is needed to determine if areas of heavily ridged ice can be separated from areas of heavily rafted ice based on knowledge of ice conditions in the days preceding the formation of high backscatter deformed ice. If rafted and ridged ice can be separated, tactical ridged ice information should be included on image analysis charts. The dual-pol data can also provide small improvements to ice extent and concentration data in derived climate data records. Further analysis of dual-pol RADARSAT-2 ScanSAR data over additional ice regimes and seasons is required.

Acknowledgements

I would like to thank my supervisor Dr. Richard Kelly for his invaluable guidance, support, and intellectual insight. It has been a pleasure to work with you over the past few years. Thanks also to committee member Dr. Claude Duguay and readers Dr. David Clausi and Dr. Stephen Howell for their valuable input. I would like to express my sincere gratitude to Dr. Roger De Abreu, Matt Arkett and Steve McCourt of the Canadian Ice Service (CIS) for their guidance in data processing and analysis. Thank you for inspiring me to carry out sea ice research. I look forward to future collaborations. Thanks also to Dr. Simon Prinsenber and Dr. Ingrid Peterson of the Bedford Institute of Oceanography (BIO) for allowing me to participate in the SGULF09 field campaign and for providing field data and technical assistance, and to the Canadian Coast Guard and pilot Bob Duff for helicopter logistic support.

I wish to thank my family and friends for their love and support over the past two years. To my classmates, thank you for the memories and the much needed breaks from work. To Mom and Dad, thank you for providing me with the opportunity to undertake graduate studies and for your endless support throughout my academic endeavours. And finally to Lisa – your endless patience, support and love have carried me through these past two years. Now on to another four!

This research was supported by NSERC Canada through an Alexander Graham Bell Canada Graduate Scholarship. The IcePic was developed and built by Geosensors Inc. for the BIO sea ice program with funding from the Panel on Energy Research and Development and through the Canadian Coast Guard R&D program. RADARSAT-2 data and products © MacDonald, Dettwiler and Associates Ltd 2009 – all rights reserved. RADARSAT is an official mark of the Canadian Space Agency. Envisat data © European Space Agency 2009. The RADARSAT-2 and Envisat data were shared through a joint project between Environment Canada, the CIS and the University of Waterloo.

Table of Contents

List of Figures	vii
List of Tables	xi
List of Abbreviations	xii
Chapter 1 Introduction.....	1
1.1 Study Context	1
1.2 Goals and Objectives	5
1.3 Structure of Thesis.....	6
Chapter 2 Background and Literature Review	7
2.1 Introduction	7
2.2 Operational Sea Ice Monitoring	7
2.2.1 CIS Ice Charts.....	9
2.2.2 Ice Chart Symbology: The Egg Code.....	10
2.3 Physical Properties of Sea Ice	12
2.3.1 Sea Ice Formation and Growth.....	13
2.3.2 Sea Ice Deformation	14
2.3.3 Sea Ice Decay	15
2.4 Electromagnetic Properties of Sea Ice.....	15
2.4.1 Pure Ice.....	16
2.4.2 Brine Inclusions.....	16
2.4.3 Air Bubbles.....	17
2.4.4 Snow Cover	17
2.4.5 Surface Roughness	17
2.5 Multi-polarization SAR.....	18
2.5.1 Polarization Concepts.....	18
2.5.2 Multi-polarization C-band Observations of Sea Ice	20
2.6 Conclusions	32
Chapter 3 Study Site, Data and Methods.....	33
3.1 Study Site	33
3.1.1 Physical Characteristics of the Gulf of St. Lawrence	33
3.1.2 Ice in the Gulf of St. Lawrence.....	35
3.2 SGULF09 Data Sets	40

3.2.1 Satellite Imagery	40
3.2.2 Field Data.....	43
3.3 Methods.....	53
3.3.1 Evaluating Ice and Open Water Discrimination	53
3.3.2 Evaluating Ice Typing.....	55
3.3.3 Evaluating Level and Deformed Ice Discrimination	57
Chapter 4 Results and Discussion.....	58
4.1 Introduction.....	58
4.2 Ice and Open Water Discrimination.....	58
4.2.1 Dual-polarization Backscatter From Open Water	60
4.2.2 Identification of the Ice Edge.....	64
4.2.3 Separation of Ice and Open Water Within Mobile Pack Ice	72
4.3 Ice Typing	84
4.4 Level and Deformed Ice Separation.....	93
4.4.1 Bright Ice Features Observed in the RADARSAT-2 Imagery.....	94
4.4.2 Backscatter from Ridged Ice Identified in Observed Ice Charts.....	111
Chapter 5 Conclusions and Recommendations.....	118
5.1 Conclusions.....	118
5.2 Recommendations.....	122
5.3 Future Work.....	123
Appendix A Egg Code Definition.....	125
References.....	126

List of Figures

Figure 2.1: The egg code (adapted from MSC, 2005).....	11
Figure 2.2: A horizontally polarized EM wave.	19
Figure 2.3: C-band HH backscatter from sea ice and open water from JPL/AIRSAR data (symbols) and from model results (curves).	22
Figure 2.4: C-band HV backscatter from sea ice and open water from JPL/AIRSAR data (symbols) and from model results (curves).	23
Figure 3.1: Oceanographic features and weather stations in the Gulf of St. Lawrence.....	33
Figure 3.2: Bathymetry of the Gulf of St. Lawrence.....	34
Figure 3.3: Water currents in the Gulf of St. Lawrence (adapted from CIS, 2001).	35
Figure 3.4: Median dates of sea ice freezeup and breakup in the Gulf of St. Lawrence, 1971-2000 (adapted from CIS, 2001).	36
Figure 3.5: Weekly ice coverage in the Gulf of St. Lawrence, winter 2008/2009.	38
Figure 3.6: Historical ice coverage in the Gulf of St. Lawrence for the week of February 26, 1969-2010.....	39
Figure 3.7: Image footprints for the SAR data acquired during SGULF09.	41
Figure 3.8: The location of IcePic and video data profiles and GPS ice beacon data acquired during SGULF09.	46
Figure 3.9: CIS Ice Tracker output.....	49
Figure 3.10: Hourly air temperature data recorded at EC weather stations around the southern Gulf of St. Lawrence, February 24 (00:00) to March 6 (23:00).....	50
Figure 3.11: Hourly winds in the southern Gulf of St. Lawrence, February 24 (00:00) to March 6 (23:00).	52
Figure 4.1: Poor discrimination between ice and open water in the near range of an Envisat/ASAR WSM HH image (March 5, 2009, 14:19).....	59
Figure 4.2: HH and HV ocean backscatter in a RADARSAT-2 SCNA image (March 5, 21:47).....	61
Figure 4.3: HH and HV ocean backscatter in a RADARSAT-2 SCWA image (March 1, 22:04).....	62
Figure 4.4: The ice edge in Cabot Strait on February 26 as observed in a) RADARSAT-2 SCWA HH data (21:52), b) MODIS/Aqua 367 false colour composite (17:15), and c) MYD29 sea ice extent data (17:15).	66
Figure 4.5: The ice edge in Cabot Strait on February 26 as observed in RADARSAT-2 SCWA HV data (21:52).....	68

Figure 4.6: The ice edge in Cabot Strait, March 5, as observed in dual-pol RADARSAT-2 SCNA imagery (21:47).....	69
Figure 4.7: The ice edge in Cabot Strait as observed in dual-pol RADARSAT-2 SCNB imagery (March 2, 10:14).	70
Figure 4.8: RADARSAT-2 SCNA imagery (March 5, 21:47) and image analysis chart vectors in the vicinity of the Iles de la Madeleine.....	73
Figure 4.9: Mosaic of video frames 40420-40436 over FY ice and open water south of the Iles de la Madeleine, March 5 (20:17).....	74
Figure 4.10: Dual-pol RADARSAT-2 SCNA imagery (March 5, 21:47) illustrating the improved visual separation of ice and open water within the FY ice pack when using a colour composite (R-HH; G-HH; B-HV).	75
Figure 4.11: Subset of the March 1 observed ice chart (Chaleurs Bay, DASH-8 recon #00024, 13:25-21:50) illustrating the increase in ice thickness from west to east between NB and PEI.	76
Figure 4.12: RADARSAT-2 SCWA imagery (March 1, 22:04) and image analysis chart vectors in western Northumberland Strait.	77
Figure 4.13: Dual-pol RADARSAT-2 SCWA (March 1, 22:04) imagery illustrating the improved separation of ice and open water when using a colour composite (R-HH; G-HH; B-HV).....	78
Figure 4.14: Subset of the February 26 observed ice chart (Baie de Gaspé, CGDX recon #00073, 12:30-13:35) illustrating the presence of new and young ice in Baie de Gaspé.	79
Figure 4.15: RADARSAT-2 SCWA data (February 26, 21:52) and image analysis chart vectors near Baie de Gaspé.	80
Figure 4.16: Dual-pol RADARSAT-2 SCWA imagery (February 26, 21:52) illustrating the improved separation of ice and open water when using a colour composite (R-HH; G-HH; B-HV).....	81
Figure 4.17: RADARSAT-2 SCWA data (21:52) and IcePic ice thickness data (16:14-18:02) acquired on February 26.	85
Figure 4.18: RADARSAT-2 SCWA data (February 26, 21:52) illustrating the reduced floe structure information and enhanced speckle in the HV channel.....	86
Figure 4.19: Dual-pol RADARSAT-2 SCWA imagery (February 26, 21:52) of ice in the Madeleine Shallows visualized using a colour composite (R-HH; G-HH; B-HV).	87
Figure 4.20: Ice type and thickness data for February 26 over the Madeleine Shallows.....	88
Figure 4.21: RADARSAT-2 SCWA imagery (10:27) and IcePic ice thickness data (14:42-14:47) acquired on March 5.	89

Figure 4.22: False colour composite (R-HH; G-HH; B-HV) of dual-pol RADARSAT-2 SCWA data (March 5, 10:27).....	90
Figure 4.23: Ice type and thickness data for March 5, east of PEI.	91
Figure 4.24: The relative roughness symbol provided in MANICE for use on image analysis charts (adapted from MSC, 2005).....	93
Figure 4.25: RADARSAT-2 and Envisat/ASAR imagery of a high backscatter feature north of Tracadie Bay, PEI.....	95
Figure 4.26: IcePic ice thickness data and video flight paths over the bright ice feature observed in the February 26 (21:52) dual-pol RADARSAT-2 data.	97
Figure 4.27: Photo of the pancake-like ice observed north of Tracadie Bay (February 26).	98
Figure 4.28: Ice thickness and roughness profiles measured over the bright ice feature north of Tracadie Bay, PEI (February 26, 18:16).	99
Figure 4.29: Mosaic of video frames 270-290 over deformed ice north of Tracadie Bay, PEI (February 26, 19:33).....	100
Figure 4.30: Mosaic of video frames 11200-11215 over deformed ice north of Tracadie Bay, PEI (February 26, 21:55).....	100
Figure 4.31: Mean backscatter ± 1 standard deviation for field validated deformed and level ice features observed in the February 26 (21:52) RADARSAT-2 data.	102
Figure 4.32: March 5 afternoon video flight paths and the location of derived video mosaics northeast of Tracadie Bay, PEI.	103
Figure 4.33: Video mosaics of March 5 ice conditions northeast of Tracadie Bay, PEI.....	104
Figure 4.34: Mean backscatter ± 1 standard deviation for field validated deformed ice (pancake-like ice and rubble), heavily ridged ice, and level ice features observed in the March 5 (10:27) RADARSAT-2 data.	105
Figure 4.35: Dual-pol (HH/HV) RADARSAT-2 (SCWA 10:17; SCNA 21:47) and single-pol (HH) Envisat/ASAR (14:19) imagery of a high backscatter feature near southwestern Cape Breton, March 5.....	106
Figure 4.36: Helicopter flight path for the morning of March 5. Ice thickness data acquired at 14:15 are overlaid on the Envisat/ASAR (HH) image (14:19).....	107
Figure 4.37: Rafted pancake ice with well-developed rims observed in eastern Northumberland Strait, March 5.....	108

Figure 4.38: Ice thickness and surface roughness profiles in the vicinity of the bright linear feature observed in eastern Northumberland Strait, between PEI and Cape Breton (March 5, 14:13-14:17).	109
Figure 4.39: Ice thickness and surface roughness profiles over rafted pancake ice in eastern Northumberland Strait, between PEI and Cape Breton (March 5, 14:15).	110
Figure 4.40: Mean backscatter ± 1 standard deviation for observed ice polygons of varying ridged ice concentration (CGDN recon #00025, 11:00-20:30), February 26.	112
Figure 4.41: Mean backscatter ± 1 standard deviation for observed ice polygons of varying ridge concentration (CGYG recon #00019, 19:25-20:40), February 26.	114

List of Tables

Table 2.1: Ice stages of development observed during SGULF09 (Adapted from MSC, 2005).....	12
Table 2.2 Forms of ice observed during SGULF09 (Adapted from MSC, 2005).	12
Table 2.3: Sea Ice Nomenclature for ice types observed during SGULF09 (after WMO, 1970).	13
Table 3.1: Summary of available SAR imagery.....	40
Table 3.2: Summary of RADARSAT-2 and ENVISAT/ASAR beam mode characteristics (MDA, 2009; ESA, 1998).....	42
Table 3.3: Summary of MODIS images with limited cloud cover.....	42

List of Abbreviations

AP	Alternating Polarization
ASAR	Advanced Synthetic Aperture Radar
CCG	Canadian Coast Guard
CIS	Canadian Ice Service
DFO	Department of Fisheries and Oceans Canada
EC	Environment Canada
EM	Electromagnetic
FY ice	First-year ice
ISS	Ice Service Specialist
IST	Ice Surface Temperature
JPL	Jet Propulsion Laboratory
MANICE	Manual of Standard Procedures for Observing and Reporting Ice Conditions
MODIS	Moderate Resolution Imaging Spectroradiometer
MY ice	Multi-year ice
NB	New Brunswick
NDSI	Normalized Difference Snow Index
NESZ	Noise-equivalent sigma-zero
PEI	Prince Edward Island
pol	Polarization (prefixed by single-, dual-, quad-, co- or cross-)
ROI	Region of interest
SAR	Synthetic aperture radar
SCN	ScanSAR Narrow
SCW	ScanSAR Wide
SGULF09	Southern Gulf of St Lawrence sea ice field survey 2009
SIR-C	Spaceborne Imaging Radar-C
UTC	Coordinated Universal Time
WMO	World Meteorological Organization
WSM	Wide Swath Mode

Chapter 1

Introduction

1.1 Study Context

The polar oceans cover 7% of the Earth's surface, an area greater than Europe and North America combined (Wadhams, 2000). Sea ice is a perennial feature in the polar oceans and it is also present as a seasonal feature in some adjacent mid-latitude regions, including the Gulf of St. Lawrence on Canada's east coast. In the Northern Hemisphere, sea ice reaches its annual maximum extent of approximately $15 \times 10^6 \text{ km}^2$ in March (Parkinson and Cavalieri, 2008). This is equivalent to one and a half times the area of Europe. The presence (or absence) of sea ice in these regions has a considerable impact on local, regional and global climates, as well as on human activity in marine environments.

Sea ice has numerous properties that make it critical to the Earth's climate system. Perhaps most importantly sea ice has a much greater albedo than open water, especially when snow covered. Typical ranges for the albedo of first-year (FY) ice, fresh snow, and open water are 0.30-0.60, 0.70-0.90 and 0.06-0.10, respectively (Serreze and Barry, 2005). The greater albedo of snow and ice relative to open water results in increased reflection of incoming solar radiation when sea ice is present. As sea ice extent decreases, more incoming solar radiation is absorbed by the ocean increasing ocean surface temperatures, which results in an increased melt rate of sea ice, generating a positive feedback loop referred to as the sea ice albedo feedback (Curry et al., 1995). This feedback mechanism is a primary component of the theory of Arctic amplification of climate change (Manabe and Stouffer, 1980). This amplification is apparent in nearly all climate model simulations (Holland and Bitz, 2003) and analysis of atmospheric reanalysis datasets indicates that this surface-based Arctic amplification has begun to emerge in recent years (Serreze et al., 2009).

Sea ice also plays a critical role in oceanic surface heat and salinity fluxes. Given the low thermal conductivity of sea ice (and of overlying snow), sea ice acts as an effective insulator between the cold

atmosphere and relatively warmer ocean; however, heat is lost rapidly in areas of open water and thin ice. The resulting ice growth in these areas leads to increased salinity in the ocean surface layer as brine is expelled during the formation of ice crystals from seawater. These heat and salt fluxes are crucial to thermohaline circulation as they contribute the most significant source of dense water for the World Ocean (Carsey et al., 1991). This source of dense, oxygen rich water is critical to life in the Earth's deep ocean (Wadhams, 2000). During the melt period the reverse occurs with the relatively low salinity sea ice acting as a freshwater supply to the upper ocean (Carsey et al., 1991). Near the ice edge (i.e. the marginal ice zone) the transition from sea ice to open water creates horizontal gradients in temperature and ocean density. This can influence cyclone development and mesoscale oceanic phenomena (e.g. eddies, upwelling). This zone is also an area of high biological activity (Serreze and Barry, 2005).

Lemke et al. (2007) identified several sea ice characteristics that need to be monitored for climate studies. They are: its concentration; its extent; the total area of ice within its extent; the area of multi-year (MY) ice within its extent; its thickness (and the thickness of snow on top of it); its velocity; and its growth and melt rates. Over the past three decades, sea ice observations indicate that considerable changes are occurring to the ice regime of the Northern Hemisphere. In particular observations of summer sea ice extent from passive microwave data show a significant decreasing trend at $-7.6 \pm 1.3\%$ decade⁻¹ over the period of 1979-2006 (Parkinson and Cavalieri, 2008). This observed rate of decrease in ice extent is greater than that predicted by general circulation models (Stroeve et al., 2007). Additionally, recent evidence suggests that the area of MY ice in the Arctic is declining and that the Arctic ice pack is thinning (Kwok et al., 2009). In order to better understand the role and impacts of sea ice in the climate system continued observations must be collected and new technologies should be exploited to reduce the uncertainty in these observations. Improved

observations will help to reduce the uncertainty in sea ice climate data records allowing us to better understand the observed changes and to better predict future changes in sea ice regimes.

In addition to the critical role that sea ice plays in the Earth's climate system, it also has considerable impacts on human activities at a more immediate timescale. This is particularly true during the Northern Hemisphere's spring when sea ice extends to mid-latitudes. The greatest impact on human activity is the considerable hazard that sea ice poses to marine navigation. In particular, ridged FY ice and MY ice present a serious hazard due to their thickness and strength. Commercial shipping and cruise tourism in Northern regions are affected by the presence of sea ice. In addition to navigational concerns ice is also a hazard to offshore infrastructure (e.g. bridges, oil platforms). The thickness and mobility of ice also affect its stability and hence its suitability for use as a platform by humans (and mammals). In northern communities sea ice plays an important role in the traditional way of life, as the fast ice edge is a productive hunting ground; however, traditional knowledge is becoming less reliable as sea ice regimes alter under a changing climate. Knowing the location of the fast ice edge in near-real time is critical to the safety and success of hunting trips in these communities (Laidler et al., 2009). Ice also provides habitat for many animals including polar bears and seals and the observed declining trend in Northern Hemisphere sea ice extent will impact these species. An accurate understanding of current ice conditions and changes occurring to ice regimes is needed to help preserve at risk species, such as the polar bear, and to ensure a sustainable harvest and proper management of seal populations (Stirling and Parkinson, 2006; Johnston et al., 2005). In order to support human marine activity, ice extent, concentration, stage of development, and drift need to be monitored and reported in near-real time.

Given the impact of sea ice on both the Earth's climate system and human marine activity, it is critical that sea ice conditions be monitored. To answer this need eighteen nations worldwide provide some form of routine ice information through operational ice services (WMO, 2006). These

institutions issue ice and iceberg information products (e.g. charts, bulletins, warnings and forecasts) to support marine navigation and to create climate data records of sea ice conditions to support climate change studies (Bertoia et al., 2004). The Canadian Ice Service (CIS) is one such institution. The mandate of the CIS is to monitor ice conditions in Canada's navigable waters and to report these conditions in a timely and accessible manner. Due to the large extent of sea ice and its rapidly changing nature, sea ice observations must provide wide areal coverage with short revisit times. Additionally, derived ice information products must be available to clients within a few hours of data acquisition to be useful for decision making in the field (Raney and Falkingham, 1994). Earth observation satellites are the only source of data that can fully meet these requirements.

Since the early 1990s synthetic aperture radar (SAR) has been the primary data source for operational ice centres. SAR systems are ideal for ice monitoring because they can acquire data independent of solar illumination and the impact of atmospheric conditions is negligible (i.e. they are all-weather systems). Traditionally operational ice centres have relied heavily on single-polarization, co-polarized (co-pol) C-band (wavelength $\lambda \approx 5.6$ cm) SAR data. In particular data from RADARSAT-1 and Envisat Advanced SAR (ASAR) were ideal for ice operations given the availability of wide swath (ScanSAR) beam modes. In the past few years several new SAR systems, which provide data previously unavailable to operational ice centres, have successfully been launched. These include RADARSAT-2 (C-band), ALOS/PALSAR (L-band), and TerraSAR-X (X-band). Each of these systems is capable of acquiring dual-polarization (dual-pol) data; however, only RADARSAT-2 is capable of acquiring dual-pol data at ScanSAR beam widths. Currently research is needed to determine what new ice information can be provided by these new SAR technologies in an operational context, especially at ScanSAR beam widths.

In this study, the sea ice information provided by dual-pol RADARSAT-2 ScanSAR data will be analysed and validated using field observations acquired during the Southern Gulf of St. Lawrence

2009 sea ice field survey (SGULF09). These field data include observations of new, young and FY ice. While previous studies have investigated the potential ice information available from dual- and quad-pol C-band SAR data, these studies have been limited almost exclusively to airborne SAR systems and more recently to narrow swath spaceborne SAR data. Therefore, their results may not apply to lower spatial resolution ScanSAR data, which are required in an operational context. This work will contribute to the effective utilization of RADARSAT-2 data at operational ice centres and will also aid in preparation for forthcoming C-band SAR constellation missions (Europe's Sentinel-1 Mission and Canada's RADARSAT Constellation Mission).

1.2 Goals and Objectives

The principal goal of this study is to identify how dual-pol RADARSAT-2 ScanSAR data can be utilized most effectively in support of operational ice monitoring activities. Additionally, this study aims to identify how improvements in operational ice charts could affect derived sea ice climate data records. In order to achieve these goals the following objectives have been set:

- i) To determine what new or improved sea ice information can be derived from dual-pol RADARSAT-2 ScanSAR data relative to single co-pol C-band SAR data.
- ii) To determine how any new or improved sea ice information derived from dual-pol RADARSAT-2 ScanSAR data could be utilized to improve the accuracy of operational ice charts in support of human marine activity.
- iii) To determine how any new or improved sea ice information derived from dual-pol RADARSAT-2 ScanSAR data could affect sea ice climate data records derived from future operational ice charts.

- iv) To recommend whether or not operational ice centres should implement a wholesale change from single- to dual-pol image acquisitions, or to identify situations where occasional dual-pol image acquisitions would be most beneficial.

1.3 Structure of Thesis

Chapter 2 provides a brief background on operational sea ice monitoring, followed by a discussion of the physical properties of sea ice and microwave interactions with sea ice. A review of the multi-polarization SAR observations of sea ice over the past several decades is also provided. Chapter 3 provides a description of the study site, the Gulf of St. Lawrence, with an emphasis on its sea ice regime. This is followed by a discussion of the various datasets employed in this study's analysis and the methods used to achieve the study objectives. Chapter 4 presents the results and key findings of the analysis, and the results are discussed in relation to the study's objectives. Chapter 5 provides a summary of the study results and discussion and provides recommendations for operational ice centres with regards to the acquisition of dual-pol data. Finally, areas where further research is required are identified.

Chapter 2

Background and Literature Review

2.1 Introduction

Over the past two decades extensive research has been carried out to better understand multi-polarization SAR backscatter signatures of sea ice. This chapter reviews the research that has been carried out to date and is organized as follows. First, a brief description of operational sea ice monitoring is provided, and the strategic and tactical ice information requirements of ice centre clients are defined. A description of the ice charts produced at the CIS and the symbology employed on the ice charts is also provided. While this information is presented within the context of operations at the CIS, much of this information is applicable to all operational ice centres. Second, the physical and electromagnetic properties of sea ice are discussed. The discussion of the physical properties of sea ice is focused on the processes of sea ice formation, growth, deformation and decay. The discussion of the electromagnetic properties of sea ice is focused on the effects of each component of sea ice (pure ice, brine, air bubbles and snow) on SAR backscatter signatures. Third, a brief introduction to the concept of polarization is provided. The chapter concludes with a review of the literature pertaining to multi-polarization C-band SAR observations of sea ice.

2.2 Operational Sea Ice Monitoring

Operational ice centres serve a variety of clients including commercial shippers, offshore exploration and development operators, fisheries, the military, regulatory agencies, scientists, and northern communities (Ramsay et al., 1993). Sea ice information requirements for these various users can be categorized into two groups, strategic and tactical, based on the level of detail (i.e. spatial and temporal resolution) required. Strategic requirements refer to information that is used for long-range planning. Tactical requirements refer to information that is used for real-time decision-making in the immediate vicinity of a vessel or platform (Ramsay et al., 1993). In relation to CIS operations,

strategic information is used to create ice analysis charts, as well as ice bulletins and forecasts. In order to meet strategic requirements sea ice data are needed on a daily basis with regional coverage. Tactical information is acquired by CIS Ice Service Specialists (ISS) deployed on Canadian Coast Guard (CCG) icebreakers, helicopters and airplanes. The data collected by ISS are used to create observed ice charts. ISS use the strategic information from ice analysis charts to help ship captains with preliminary route planning, while the tactical information from observed ice charts is used for real time route adjustments (Scheuchl et al., 2004a).

For both strategic and tactical requirements, sea ice parameters of interest for marine users include: location of the ice edge; total ice concentration; ice type and thickness; ice topography (i.e. presence of pressure ridges and rubble fields); presence and location of leads; and state of ice decay (Ramsay et al., 1993). From a strategic perspective the most critical sea ice parameters are the location of the ice edge, total ice concentration and ice type. The ice edge is defined as the boundary between ice and open water. If the ice edge is diffuse the CIS defines open water as having a total ice concentration of $<1/10$ (MSC, 2005). The limit of all known ice, beyond which water is ice-free, must also be known. For strategic purposes the ice edge should be accurate to within 5 km, while ice concentration estimates should be accurate to within $\pm 10\%$ (Scheuchl et al., 2004a). Where possible these primary sea ice parameters should be mapped at a regional scale on a daily basis to meet strategic requirements. The remaining ice parameters (ice topography, presence of leads, and state of decay) are primarily of importance for tactical considerations and ice topography and leads are mapped in observed ice charts. For tactical purposes sea ice data are required in near-real time and at a much higher spatial resolution (e.g. the ice edge should be accurate to within 1 km, while ice concentration estimates should be accurate to $\pm 5\%$) (Scheuchl et al., 2004a). Both strategic and tactical ice information are distributed by the CIS via ice charts.

2.2.1 CIS Ice Charts

Operational sea ice charts produced at the CIS can be categorized as observed ice charts or ice analysis charts. Observed ice charts are created in the field by ISS, while ice analysis charts are created at the CIS by Ice Analysts. Ice analysis charts can be further categorized as image analysis charts, daily ice analysis charts, and regional ice charts. The method of production (specifically the datasets incorporated and the timing of chart dissemination) varies for each chart type.

Observed ice charts are based primarily on visual observations carried out by ISS (from ship decks, helicopters or airplanes). These charts, which are produced whenever a ship or aircraft with an ISS onboard encounters sea ice, provide tactical ice information. Where available, visual observations are supplemented with electronic aids such as airborne SAR (MSC, 2005).

Image analysis charts are created for every SAR image acquired by the CIS. The information in these charts is derived primarily from visual interpretation of the SAR data, although support data are also incorporated. Support data include environmental conditions, ice climatology and coincident observed ice charts. Image analysis charts are a near-real time product, produced on a strict timeline. CIS operational requirements state that SAR data must be received at the CIS within 3 hours of data acquisition (Ramsay et al., 1993), and image analysis charts must be produced within 4 hours of data reception at the CIS (MSC, 2005).

Daily ice analysis charts are produced once per day and are distributed at 18:00 Coordinated Universal Time (UTC). These charts are derived primarily from SAR data (and associated image analysis charts), which are supplemented with additional remote sensing datasets (e.g. NOAA/AVHRR, GOES, SSMI, QUICKSCAT) as well as observed ice charts. The CIS ice model is also used to advance ice conditions if remote sensing observations are not available on a given day. Daily ice analysis charts are the primary dataset used for strategic planning (MSC, 2005).

Regional ice charts provide generalized ice conditions incorporating all available data usually within three days of the chart's valid date. The main data sources incorporated are satellite images and daily ice analysis charts; however, the information from daily ice analysis charts is generalized in order to prevent the smaller map scale regional charts from becoming too cluttered. Regional charts are produced on a weekly, bimonthly or monthly basis depending on the season and ice region. These charts are the primary climatological product issued by the CIS (MSC, 2005).

In this study, the sea ice information content of dual-pol RADARSAT-2 images and the accuracy of derived image analysis charts will be evaluated. Observed ice charts will be utilized as a validation dataset to help guide the interpretation of the dual-pol imagery. Daily ice analysis and regional ice charts, which incorporate additional remote sensing datasets beyond the RADARSAT-2 data are not evaluated.

2.2.2 Ice Chart Symbolology: The Egg Code

The symbolology employed on CIS ice charts is derived from the World Meteorological Organization (WMO) *International system of sea-ice symbols* (WMO, 1989) and *Ice chart colour code standard* (WMO, 2004); however, some symbols specific to the CIS are also utilized and the symbolology varies slightly between observed, image analysis, daily ice analysis and regional ice charts. In order to facilitate the interpretation of ice chart data presented in this paper the foundation of the ice chart symbolology, the 'egg code', is described here. Where necessary additional symbols are discussed later in this paper. The reader is directed to the *Manual of standard procedures for observing and reporting ice conditions* (MANICE) (MSC, 2005) for the complete symbolology of CIS charts.

For each ice polygon digitized in an ice chart an associated egg code is generated. These egg codes store information about the ice properties within each ice polygon. An egg is broken down into four

levels, each storing a different ice parameter. Each level of the egg code may be further broken down into several columns, one for each ice type present within the polygon (Figure 2.1).

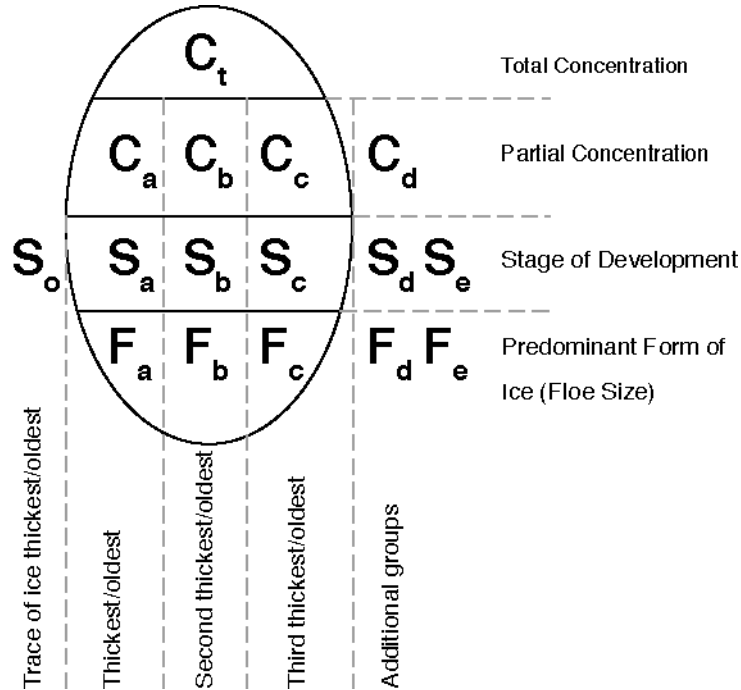


Figure 2.1: The egg code (adapted from MSC, 2005).

The top row defines the total concentration of ice within the polygon (C_t), reported in tenths. The second row defines the partial concentration for each ice type present within the ice polygon (C_a , C_b , C_c), again reported in tenths. The third row defines the stages of development (i.e. types) of ice present within the ice polygon (S_a , S_b , S_c). The fourth and bottom row defines the predominant form of ice (i.e. floe size) (F_a , F_b , F_c). Numeric codes are used to represent the various stages of development (Table 2.1) and forms of ice (Table 2.2) within the egg code. When more than one ice type is present within an ice polygon the columns of the egg code are sorted based on stage of development with the oldest (thickest) ice type on the left. The egg itself can be broken down into three columns. When more ice types are present additional groups can be added outside of the egg on its right side (S_d , S_e). If there is a trace ($< 1/10$ concentration) of ice reported that is older than any ice type within the egg code it is placed to the left of the egg (S_o).

Table 2.1: Ice stages of development observed during SGULF09 (Adapted from MSC, 2005).

Stage of Development	Ice Thickness [†] (cm)	Code
New ice	< 10	1
Nilas; Ice rind	< 10	2
Young ice	10-30	3
Grey ice	10-15	4
Grey-white ice	15-30	5
FY ice	≥ 30	6
Thin FY ice	30-70	7
Medium FY ice	70-120	1•
Thick FY ice	> 120	4•
Brash ice		-
Undetermined, unknown		X

[†]Ice thickness ranges assume level (undeformed) ice conditions.

Table 2.2 Forms of ice observed during SGULF09 (Adapted from MSC, 2005).

Form of Ice	Width [†]	Code
Small ice cake, brash ice	<2 m	1
Ice cake	2-20 m	2
Small floe	20-100 m	3
Medium floe	100-500 m	4
Big floe	500-2000 m	5
Vast floe	2-10 km	6
Fast ice		8
Undetermined, unknown or no form		X
Ice in strips in which concentration is C		~ C

[†]Width refers to the maximum horizontal extent of an ice floe.

2.3 Physical Properties of Sea Ice

In this section the processes of sea ice formation, growth, deformation and decay are discussed in relation to their effects on the physical properties of sea ice. The *WMO Sea Ice Nomenclature* (WMO, 1970) is adopted for the definition of all sea ice types in order to correspond with the terminology used at operational ice centres. Definitions of the various stages of development of ice referenced in this study are provided in Table 2.3.

Table 2.3: Sea Ice Nomenclature for ice types observed during SGULF09 (after WMO, 1970).

Stage of Development (Ice Type)	Definition
New ice	A general term for recently formed ice. These types of ice are composed of ice crystals, which are only weakly frozen together (if at all) and have a definite form only while they are afloat. Here, new ice refers collectively to frazil, grease ice, nilas and pancake ice.
Frazil ice	Fine spicules or plates of ice, suspended in water.
Grease ice	A later stage of freezing than frazil ice when the crystals have coagulated to form a soupy layer on the surface. Grease ice reflects little light giving the sea a matte appearance.
Nilas	A thin elastic crust of ice easily bending on waves and swell and under pressure, thrusting in a pattern of interlocking “fingers” (finger rafting). Has a matte surface and is up to 10 cm in thickness.
Pancake ice	Predominantly circular pieces of ice from 30 cm – 3 m in diameter, and up to about 10 cm in thickness, with raised rims due to the pieces striking against one another.
Young ice	Ice in the transition stage between nilas and FY ice, 10-30 cm in thickness. May be subdivided into grey and grey-white ice.
Grey ice	Young ice 10-15 cm thick. Less elastic than nilas and breaks on swell. Usually rafts under pressure.
Grey-white ice	Young ice 15-30 cm thick. Under pressure more likely to ridge than to raft.
FY ice	Sea ice of not more than one winter’s growth, developing from young ice; thickness 30 cm – 2 m. May be subdivided into thin FY ice (30-70 cm thick), medium FY ice (70-120 cm thick) and thick FY ice (over 120 cm thick).

2.3.1 Sea Ice Formation and Growth

The formation of sea ice begins with the development of frazil ice crystals. Frazil begins to form when seawater reaches its salinity adjusted freezing point. For a typical ocean salinity of 35 psu the freezing point is -1.8°C (Wadhams, 2000). As cooling continues and frazil accumulates, grease ice, which suppresses surface waves, begins to form. The sea state determines what ice type forms as grease ice continues to cool. Under calm conditions nilas ice forms, while in rough sea states nilas cannot form (or it is broken up) due to the divergent and convergent forces applied by wind stress. Pancake ice forms in these conditions. Pancake ice, like nilas, is very saline; however, the surface

roughness of pancake ice is much greater due to the raised rims that form as frazil is splashed over the edges of the pancakes and freezes to its surface. Eventually pancakes freeze together forming a continuous sheet of consolidated ice (Wadhams, 2000). Collectively, frazil, grease ice, nilas and pancake ice are termed new ice, and all of these ice types have high salinities. The orientation of ice crystals is random for these ice types of frazil origin (Wadhams, 2000).

Once ice reaches a thickness of ~10 cm the mechanism of ice growth changes and congelation growth (water molecules freezing to ice crystals at the ice-sea water interface) becomes dominant. Due to the structure of ice crystals congelation growth favours the development of crystals with a horizontal c-axis, resulting in columnar ice growth (Wadhams, 2000). As ice crystals form from sea water, dissolved salts are expelled. While ice crystals themselves are salt free the brine-rich water between ice crystals can become entrapped within a growing ice sheet by the formation of ice bridges between ice platelets. Air bubbles can also be included into sea ice by this ice bridging process. The walls of brine inclusions freeze until the brine is saline enough that the salinity adjusted freezing point of the brine is in equilibrium with the temperature of the surrounding ice (Wadhams, 2000). As congelation ice growth continues through the young and FY stages of development the salinity of ice is continually reduced through the processes of brine cell migration, brine expulsion and gravity drainage. These desalination processes act continually throughout sea ice development; therefore, new and young ice types are the more saline (~10 psu) than FY ice (~4-6 psu) (Wadhams, 2000).

2.3.2 Sea Ice Deformation

When ice is subject to compacting ice motion (due to convergent ice drift) the stress results in deformation. Deformed ice is “a general term for ice which has been squeezed together and in places forced upwards (and downwards),” while level ice is “sea ice which is unaffected by deformation,” (WMO, 1970). Deformed ice can be further separated into rafted ice and ridged ice. Rafted ice is formed when one piece of ice overrides another. A ridge is a line or wall of broken ice forced

upwards and downwards by pressure (WMO, 1970). The portion of a ridge found above the surrounding level ice is termed the sail, while the submerged volume of broken ice forced downwards is termed the keel. The depth of the keel is typically three to five times the height of the sail (WMO, 2006). When subject to pressure new and grey ice are likely to raft, while grey-white and FY ice are likely to ridge (WMO, 1970). The surface roughness of deformed ice is greater than that of level ice.

2.3.3 Sea Ice Decay

When air or sea surface temperatures rise above the freezing point, sea ice and snow melt. For sea ice and saline (brine-wetted) snow, it is important to note that the temperature of the freezing point is below 0°C (and is dependent on salinity). As the snowpack or ice surface melts, melt ponds can form on the surface of the ice. These ponds are typically shallow for FY ice, which generally has a smooth surface, although the presence of ridges can help to constrain the melt water. Melt ponds preferentially absorb incoming solar radiation relative to higher albedo bare ice, thereby accelerating the ablation of the ice (Wadhams, 2000). Sea ice also ablates from the bottom if the sum of the ocean heat flux and the conductive heat flux through the ice is positive (Serreze and Barry, 2005). As ice ablates melt water flushes brine channels, further reducing the salinity of the ice (Wadhams, 2000). In the Gulf of St. Lawrence all sea ice melts in the spring; therefore, ice in this region does not develop beyond the FY stage of development.

2.4 Electromagnetic Properties of Sea Ice

Sea ice is a mixed medium made up of pure ice crystals, brine inclusions, air bubbles, and at times it is covered by snow. Each of these components of sea ice, in addition to its surface roughness, impact its electromagnetic properties (Nghiem et al., 1995; Morey et al., 1984). In order to interpret backscatter signatures in spaceborne SAR data, an understanding of the electromagnetic properties of each component of sea is necessary. The effects of radar system parameters must also be known.

The electromagnetic properties of sea ice are governed by its relative permittivity ε (or relative complex dielectric constant), defined by the equation

$$\varepsilon = \varepsilon' - j\varepsilon'' \quad (2.1)$$

where $j = \sqrt{-1}$, ε' is the real part of the relative permittivity (or the dielectric constant), ε'' is the imaginary part of the relative permittivity (or the dielectric loss factor) and j indicates that ε'' is an imaginary number (Hallikainen and Winebrenner, 1992). The relative permittivity of sea ice is dependent on the dielectric properties of each of its constituent parts, which determine how incident electromagnetic radiation behaves as it interacts with sea ice (Hallikainen and Winebrenner, 1992). Electromagnetic radiation can be transmitted, scattered, or absorbed at the interface between any two media.

2.4.1 Pure Ice

The dielectric properties of ice are such that microwaves, for the most part, are transmitted through pure ice (Nghiem et al., 1995); therefore, ice crystals themselves have only a small impact on backscatter from sea ice, although their structure is important. The preferential vertical structure of sea ice crystals renders the backscatter signature of sea ice anisotropic, meaning that the backscatter from sea ice is not equal when measured in all directions (Nghiem et al., 1995). This is because brine inclusions, which have a strong effect on the electromagnetic properties of sea ice, follow the preferred vertical orientation of ice crystals.

2.4.2 Brine Inclusions

Brine inclusions have a high permittivity that strongly affects the backscatter from sea ice (Nghiem et al., 1995). In particular, brine has a high dielectric loss factor, meaning that incident microwave radiation is attenuated by brine inclusions (Hallikainen and Winebrenner, 1992). As a result, thin saline ice types typically produce little backscatter. In contrast, older, less saline ice types produce

higher backscatter. Additionally, Morey et al. (1984) found that the real part of the relative permittivity of sea ice was strongly dependent upon brine volume and that the dielectric effects of brine are temperature dependent, because temperature controls the brine volume.

2.4.3 Air Bubbles

Through the processes of desalinization microwaves are able to penetrate deeper into ice due to the reduced lossy brine volume. The dielectric constant and spherical shape of air bubbles (formed either during congelation growth or by the draining of brine inclusions) causes incident radiation to scatter in a diffuse manner (Nghiem et al., 1995). Given the low dielectric loss factor of air bubbles, multiple scattering within the ice volume can occur (Hallikainen and Winebrenner, 1992); therefore, the presence of air bubbles increases the volume scattering component from sea ice, which can greatly increase backscatter for low density, low salinity ice types.

2.4.4 Snow Cover

During the winter, when snow cover is dry, snow has a minimal effect on sea ice backscatter at C-band since incident microwave radiation is transmitted through the snowpack; however, snow can wick brine from the sea ice surface creating a slush layer with a strong dielectric loss factor (Nghiem et al., 1995). During the melt period, the presence of liquid water in the snow alters the relative permittivity of the snow cover, causing attenuation of the incident microwave radiation (Hallikainen and Winebrenner, 1992). When either a brine-rich slush layer or a wet snowpack exists above sea ice the backscatter signature of the underlying sea ice can be masked, making observations of ice type extremely difficult (Arkett et al., 2007).

2.4.5 Surface Roughness

Surface roughness can influence backscatter as it controls whether specular or diffuse scattering occurs at the air-ice (or air-snow and snow-ice) interface(s). When the wavelength of an incident

microwave is similar in size to the surface roughness of a feature diffuse scattering is more likely to occur, increasing backscatter. If the surface roughness is smaller than the wavelength of the incident microwave specular scattering is more likely to occur, reducing backscatter by directing the scattered microwaves away from the SAR sensor; therefore, the frequency at which observations are acquired has a significant impact on how surface roughness affects backscatter (Onstott, 1992).

In addition to the physical properties of ice, radar system parameters (frequency, polarization, incidence angle range and noise-equivalent sigma-zero (NESZ)) can greatly influence sea ice backscatter, complicating the effects of the electromagnetic properties of sea ice (Onstott, 1992). Recent sea ice literature (~1990-present) related to operational sea ice monitoring has focused on characterizing C-band backscatter for various radar parameters. As a result, C-band sea ice backscatter at various polarizations and incidence angles have been defined, as has the impact of NESZ; however, little research has been carried out for multi-polarization C-band data at the spatial resolution and swath width of ScanSAR data.

2.5 Multi-polarization SAR

In this section a brief introduction to radar polarimetry is provided, followed by a thorough review of the literature relating to multi-polarization C-band SAR observations of sea ice.

2.5.1 Polarization Concepts

Under the wave theory, electromagnetic (EM) radiation can be expressed as a pair of orthogonal waves, one representing the electric field component and one representing the magnetic field component. EM waves are transverse waves, meaning that the oscillations of the wave are perpendicular to the direction of travel. The parameter that defines the direction in which the oscillations take place is termed polarization (Woodhouse, 2006). By convention, the polarization of a wave defines the alignment of the electric field of the wave. For linearly polarized systems a wave

can be either horizontally polarized or vertically polarized. When the electric field oscillates only in the x-direction the wave is said to be horizontally polarized (H). When the electric field oscillates only in the y-direction the wave is said to be vertically polarized (V). For SAR applications, the x-axis is defined as being parallel to the surface of the Earth (Woodhouse, 2006). A horizontally polarized wave is illustrated in Figure 2.2.

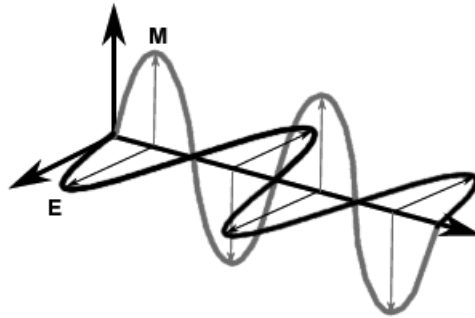


Figure 2.2: A horizontally polarized EM wave. E represents the electric field and M represents the magnetic field (adapted from ESA, 2010).

While polarization can also be circular or elliptical (Woodhouse, 2006), the vast majority of SAR sensors, including RADARSAT-2, are designed as linearly polarized systems; therefore, only linear polarizations are considered in this study. SAR systems can transmit and receive EM radiation in different polarizations. For linearly polarized systems there are two possible transmit polarizations and two possible receive polarizations, resulting in four possible polarization channels, which correspond to the four possible backscatter coefficients σ_{pq}° , where the p -transmit and q -receive polarizations can be H or V. The polarization channels are HH, HV, VH and VV, where the first letter denotes the polarization of the transmitted wave and the second letter denotes the polarization of the received wave. When $p = q$ the polarization channel is said to be co-polarized (co-pol). When $p \neq q$ the polarization channel is said to be cross-polarized (cross-pol). Single-polarization SAR systems can acquire backscatter data at one polarization channel, while dual-polarization SAR systems can acquire backscatter data at two polarization channels, and quad-polarization SARs system can acquire

backscatter data at all four polarization channels. In addition to measuring the amplitude of the backscattered signal, fully polarimetric SAR systems also record the phase of the backscatter at all four polarization channels. For ScanSAR acquisitions RADARSAT-2 is limited to dual-pol data (HH+HV or VV+VH). The dual-pol RADARSAT-2 data for this study are all HH+HV acquisitions. For RADARSAT-2 ScanSAR products only the backscatter amplitude is provided (phase information is not available).

2.5.2 Multi-polarization C-band Observations of Sea Ice

Since the late 1980s numerous studies have examined the potential of multi-polarization SAR data for sea ice monitoring; however, these studies have been limited to a small number of datasets. These observations have primarily been acquired with fully polarimetric airborne SAR systems, including the Jet Propulsion Laboratory's (JPL) AIRSAR (e.g. Drinkwater et al., 1991; Rignot and Drinkwater, 1994; Shokr et al. 1995), the Danish EMISAR (e.g. Thomsen et al., 1998; Dierking et al., 2004), the Canadian CV-580 (e.g. Livingstone, 1994; Flett, 1997; Ramsay et al., 2004) and the Japanese Pi-SAR (e.g. Matsuoka et al., 2001). Each of these fully polarimetric SARs is capable of operating at two or more frequencies. All of these systems, except Pi-SAR, can acquire C-band data. The majority of the research resulting from these airborne campaigns has focused on evaluating the ability to map sea ice types using the complete fully polarimetric, multi-frequency data. While the results (particularly for multi-frequency data) are promising, no existing spaceborne SAR systems are capable of providing either multi-frequency or fully polarimetric observations at wide swath widths. Only RADARSAT-2 can provide multi-polarization data at ScanSAR beam modes and this is limited to dual-pol acquisitions. Additionally, the system parameters of airborne SARs, particularly NESZ, incidence angle range, and spatial resolution, are often not representative of those of spaceborne SARs. In the past decade a limited number of studies of multi-polarization spaceborne C-band SAR data have been undertaken. Datasets for these studies were acquired with the fully polarimetric Spaceborne Imaging

Radar-C (SIR-C) (Scheuchl et al., 2001), and Envisat/ASAR, using the Alternating Polarization (AP) mode (e.g. Scheuchl et al., 2004a; Arkett et al., 2006; Arkett et al., 2007). Once again, the system parameters of SIR-C and Envisat/ASAR AP are not identical to those of RADARSAT-2 ScanSAR data, but the differences are less relative to airborne SAR systems. To date, only Flett et al. (2008) have evaluated dual-pol RADARSAT-2 ScanSAR data for operational sea ice monitoring. Yu (2009) and Yu et al. (submitted) have also evaluated the sea ice information content of dual-pol RADARSAT-2 ScanSAR data in the context of automated image segmentation. In the following sections results from these various campaigns and studies are summarized, with the discussion being limited to results pertaining to C-band dual-pol (HH+HV and VV+VH) data.

2.5.2.1 Ice-Open Water Separation

The first objective in operational sea ice mapping is to delineate the ice edge. In single co-pol (HH or VV) C-band SAR data the contrast in backscatter between ice and open water can vary greatly depending on incidence angle, ice type, and wind conditions (Scheuchl et al., 2004a). Under most circumstances, backscatter from open water is greater than backscatter from ice in the near range; however, the backscatter signal from open water decays significantly across range relative to the backscatter response from ice, resulting in a signature crossover. When such a crossover is present the delineation of the ice edge and estimation of ice concentration are uncertain. The incidence angle at which this crossover occurs is dependent on wind speed and ice type. This crossover is evident in both modelled and observed backscatter data (Figure 2.3).

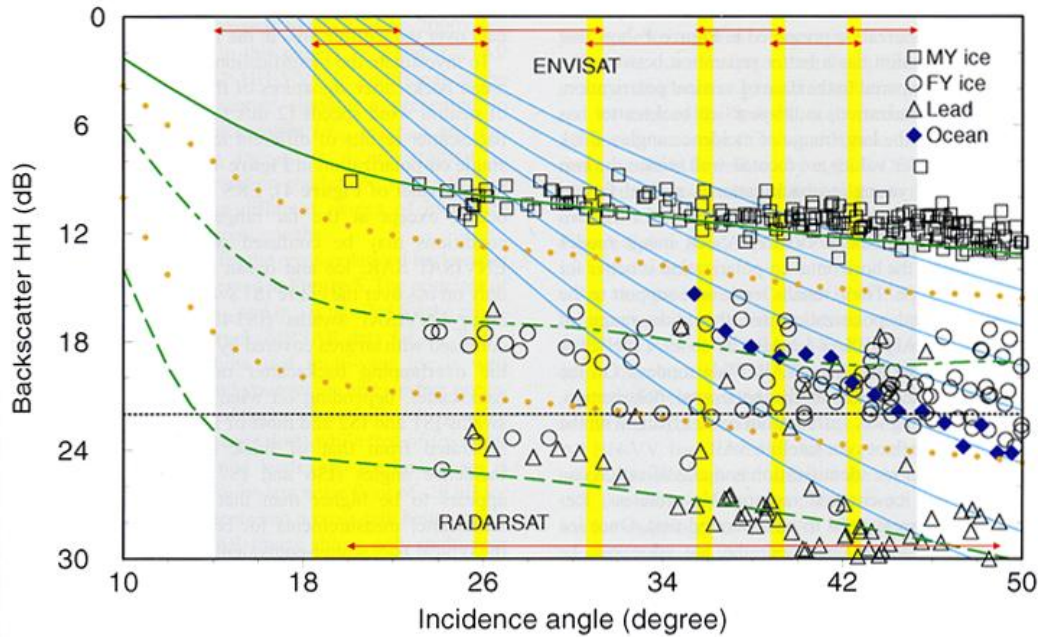


Figure 2.3: C-band HH backscatter from sea ice and open water from JPL/AIRSAR data (symbols) and from model results (curves). Open water backscatter (cyan curves) is modelled for neutral winds of 2 m/s, and 4 m/s to 24 m/s in increments of 4 m/s. Orange dots indicate backscatter thresholds between different ice types. The black dotted line is a NESZ at -22 dB (Nghiem and Bertoia, 2001).

The modelled ice backscatter values in Figure 2.3 are derived from the polarimetric forward backscatter model of Nghiem et al. (1995), and the modelled ocean backscatter values are derived from the empirical geophysical model CMOD3-H1 of Long (1992). The observed ice and ocean backscatter values are derived from JPL/AIRSAR data acquired in the Beaufort and Bering Seas during March 1988 over winter sea ice conditions (Nghiem and Bertoia, 2001). Modelled and observed results for VV polarization (not shown) are similar although differences in backscatter between ice types are reduced relative to the HH data and backscatter from open water is increased, especially at shallow incidence angles (Nghiem and Bertoia, 2001). The modelled improvement in separation of ice types at HH is in agreement with operational experience at the CIS where a preference for HH imagery has developed over two decades of analyzing ERS-1/-2, Envisat/ASAR and RADARSAT-1/-2 data (Scheuchl et al., 2004a). However, single co-pol data at either HH or VV cannot unambiguously separate ice and open water at all incidence angles and wind speeds. Several

authors (e.g. Nghiem and Bertoina, 2001; Thomsen et al., 1998; Scheuchl et al., 2001) have suggested that the co-pol ratio ($\gamma = \sigma_{VV}/\sigma_{HH}$) provides considerable improvements in ice-open water discrimination, especially at shallow incidence angles; however, dual co-pol data (HH+VV) is not available for RADARSAT-2 ScanSAR acquisitions.

In contrast to co-pol data, models and observations indicate that cross-pol backscatter from ice and open water is reasonably stable across range (Figure 2.4).

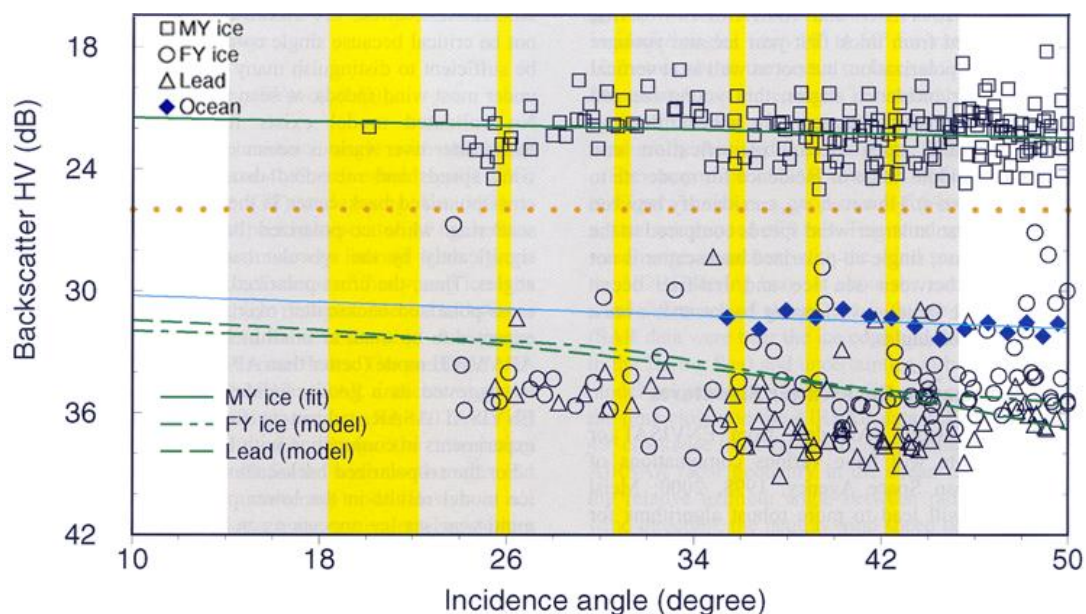


Figure 2.4: C-band HV backscatter from sea ice and open water from JPL/AIRSAR data (symbols) and from model results (curves). Open water backscatter (cyan curve) is modelled from observed values using a linear regression. The wind speed for the observations is estimated as 10 m/s. Orange dots indicate backscatter thresholds between different ice types. The black dashed line is a NESZ at -22 dB (Nghiem and Bertoina, 2001).

Few studies of airborne SAR data discuss cross-pol backscatter from open water. This is in part due to the fact that many of the datasets were acquired in the Arctic in winter conditions and areas of open water were not present in the datasets. Results from EMISAR observations acquired in the Greenland Sea demonstrate that ice and open water have improved contrast at cross-polarizations (Skriver and Pedersen, 1995); however, this result was based on backscatter from MY ice. More recently, ice and

open water separation has been evaluated from SIR-C and Envisat/ASAR AP data. These studies have included observations of new, young and FY ice in addition to MY ice.

Scheuchl et al. (2001) analysed a SIR-C scene acquired over the Gulf of St. Lawrence. The SIR-C data cover a limited range of incidence angles (26° to 31°) and were multi-looked to a pixel size of 100 m by 100m (64 looks). The HV backscatter from open water was found to be effectively constant across range, although it was suggested that the system NESZ likely limited the ocean backscatter. It was determined that a simple threshold (of -23.8 dB) was capable of separating open water from FY ice in the HV channel and that the resulting ice/open water classification was more accurate than results derived from thresholding either HH data or co-pol ratio data. While promising, these results may not apply to RADARSAT-2 ScanSAR data given the limited incidence angle range and the large number of looks (reduced speckle) of the SIR-C data (RADARSAT-2 ScanSAR data has 8 looks).

Envisat/ASAR AP data can be acquired at 7 different Image Mode Swaths (IS1 to IS7), which combined cover incidence angles of 15.0° to 45.2° (ESA, 1998). While any one AP swath covers only a narrow range of incidence angles, datasets comprised of numerous images acquired from each of the seven swaths have provided a more robust evaluation of the impact of incidence angle on ice and ocean backscatter in cross-pol data. Arkett et al. (2007) analyzed 63 AP images acquired in the Canadian Arctic near Resolute, Nunavut. They determined that the HV channel provided improved contrast between ice and open water relative to the HH channel, especially at steep to moderate incidence angles; however, they noted that the contrast between new, young and smooth FY ice was greatly reduced in the HV channel. At shallow incidence angles (IS7, 42.5° to 45.2°) Arkett et al. (2007) observed that new ice could not be separated from open water in the HV channel, likely due to the NESZ limitations of Envisat/ASAR. In contrast new ice was readily identifiable in the HH channel given the low ocean clutter at these shallow incidence angles. As a result, Arkett et al. (2007)

strongly recommended the acquisition of dual-pol data over either single co- or single cross-pol data for ice and open water separation at ScanSAR beam widths.

Scheuchl et al. (2004b) evaluated a Bayesian Wishart (unsupervised) classifier to automatically separate ice types in 13 AP images acquired near Resolute. Qualitative evaluation of the classification output indicated that separation of ice and open water was improved for IS1 through IS5 (15.0° - 39.4°) but that at IS6 (39.1° - 42.8°) the open water class may have contained new ice that could not be identified due to noise limitations. Scheuchl and Cumming (2005) further evaluated the impact of ASAR's NESZ in an IS4 image (31.0° - 36.3°). Estimates of the NESZ across the IS4 swath ranged from -24.5 dB to -20.5 dB. Based on the estimated NESZ, the expected values of the signal to noise ratio (SNR) for open water, and new, young, and smooth FY ice in the cross-pol channel could be <0 dB. As a result, the NESZ of ASAR is expected to impact both visual and automated ice-open water discrimination and ice type classification (Scheuchl and Cumming, 2005). While Scheuchl et al. (2004b) and Arkett et al. (2007) report that FY ice-open water separation is easily achieved in cross-pol data at steep incidence angles, this may not always be the case. Peterson et al. (2006) analyzed an IS2 image (19.2° - 26.7°) acquired in the Amundsen Gulf and found that a lead within a region of smooth FY ice was identified in the HH channel, and high backscatter suggests that the lead contained wind roughened open water, yet the lead could not be separated from the surrounding smooth FY ice in the HV channel. Peterson et al. (2006) suggested that this might be due to the low SNR for both the smooth FY ice and open water.

The NESZ for RADARSAT-2 ScanSAR beam modes is -28.5 ± 2 dB (MDA, 2009). This is a considerable improvement over the NESZ of Envisat/ASAR AP data, which varies between -19.4 dB and -22.0 dB over the various IS swaths (ESA, 1998). Given the improved NESZ, the limitations of cross-pol data observed in ASAR AP data may be reduced or eliminated in RADARSAT-2 data.

Preliminary evaluation of dual-pol RADARSAT-2 ScanSAR data at the CIS (Flett et al., 2008) suggests that the anticipated improvement in ice-open water separation for dual-pol RADARSAT-2 ScanSAR data is achieved and that the separation of new ice and open water is possible in at least some conditions. Results from Yu (2009) indicate that the use of a hierarchical image segmentation algorithm shows considerable potential for separating ice and open water in dual-pol RADARSAT-2 ScanSAR data, although the segmentation process could not be fully automated (user input was required to define the segmentation hierarchy). Unfortunately, Flett et al. (2008) and Yu (2009) were limited to a small number of images and no field data were available to validate the image interpretation or image segmentation results. Based on these results, it is anticipated that cross-pol data should improve the accuracy of ice edge delineation and ice concentration estimates in images where an ice-ocean backscatter crossover exists in the co-pol data; however, the SNR for new, young and smooth FY ice in cross-pol RADARSAT-2 data may still be too low to consistently separate these ice types from open water at all incidence angles. As a result, further evaluation of the separability of new, young and smooth FY ice from open water in RADARSAT-2 data is needed.

2.5.2.2 Ice Typing

Once the ice edge has been delineated and ice concentrations have been determined, the next task in operational ice monitoring is to segment the ice pack into regions with distinct backscatter signatures and to determine the various ice types (stages of development) that are present within each of these regions. With single co-pol C-band SAR data the accuracy of manual ice typing is sufficient for operational requirements, except during the melt period when wet snow or melt ponds mask the backscatter signature of the underlying ice. Under dry conditions new, young, FY, and MY ice are separable in co-pol data, yet there is still the potential that cross-pol data can enhance the accuracy of ice typing, given that it has heightened sensitivity to different scattering mechanisms (primarily volume and multiple surface scatter) relative to co-pol data (primarily single surface scatter). Analysis

of airborne polarimetric SAR data, primarily acquired in the Arctic, has been heavily weighted towards evaluating the potential improvement in the separation of FY and MY ice due to the strong volume scattering component of MY ice cross-pol backscatter (e.g. Rignot and Drinkwater, 1994; Shokr et al., 1995); however, MY ice is not observed in the Gulf of St. Lawrence. The following paragraphs explore the limited evaluations of new, young and FY ice typing in cross-pol data.

New, young and FY ice types are primarily surface scatterers at C-band (assuming level ice conditions). This is in part due to the short penetration depths of these highly saline ice types, which limits volume scattering (e.g. the penetration depth of FY ice with a salinity of 7.5 psu and temperature of -5°C is less than 0.2 m at C-band; Hallikainen and Winebrenner, 1992). Additionally, these ice types are usually smooth meaning that multiple surface scattering is minimal. These ice types are therefore expected to have very low cross-pol backscatter, as has been observed and modelled (Figure 2.4). Given the low backscatter from these ice types there has been considerable concern that noise limitations of spaceborne SAR systems could prevent these ice types from being detected (Arkett et al., 2006).

Analysis of AIRSAR data from the Beaufort Sea has provided mixed results. Rignot and Drinkwater (1994) found that classification of the HH and HV channels combined provided 10% greater accuracy than classifications of the HH channel alone, suggesting that some ice type information is provided by the HV channel. Results from Drinkwater et al. (1991) indicate that the cross-pol ratio ($r_{cross} = \sigma_{HV}/\sigma_{HH}$) can be used to separate thin ice types (< 30 cm) from FY ice; however, Shokr et al. (1995) state that the cross-pol ratio provides no discrimination between ice types. Analysis of EMISAR data from the Beaufort and Greenland Seas do not indicate that the cross-pol channel provides any improvement in ice typing over single co-pol channels. This is apparent as none of the decision rules of the knowledge-based classifier of Dierking et al. (2004) incorporate the cross-pol channel to separate between FY and thin (< 30 cm) ice types.

Analysis of Envisat/ASAR AP data also provide mixed results. Scheuchl and Cumming (2005) state that the separation of new, young and smooth FY ice is expected to be considerably limited at cross-polarizations given the high NESZ. Analysis of a pair of AP images (IS3 and IS6), acquired over McDougall Sound in the Canadian Arctic, supports this statement. In these images the difference in backscatter between new and young ice types is greatly reduced in the HV channel (relative to the HH channel), making discrimination of these ice types impossible when using the HV data alone (Arkett et al., 2006). In contrast to these results, analysis of an IS2 image acquired over the Amundsen Gulf indicated that the contrast between thin ice (< 30 cm) and smooth FY ice was greater in the HV channel than in the HH channel (Peterson et al., 2006). This was attributed to the presence of frost flowers, which produced a high cross-pol backscatter from the thin ice, while the cross-pol backscatter from smooth FY ice was low. Frost flowers, which require extremely cold temperatures to develop (Perovich and Richter-Menge, 1994), are less likely to form in mid-latitude regions than in the Arctic; therefore, it is anticipated that in the Gulf of St. Lawrence the separation of new, young and FY ice would be limited in cross-pol data. Once again, these results must be re-evaluated at the lower NESZ of RADARSAT-2.

Preliminary results from Flett et al. (2008) indicate that cross-pol data from RADARSAT-2 also suffer from reduced detail over new, young and smooth FY ice. This is evident in an image acquired over Chaleur Bay in the Gulf of St. Lawrence where considerable detail is visible in the HH channel but is completely absent from the HV channel. These results suggest that the cross-pol channel likely will not provide any benefits for ice typing of new, young and smooth FY ice. In contrast to these findings, results from an automated image segmentation algorithm applied to a subset of a dual-pol RADARSAT-2 ScanSAR image acquired over the Gulf of St. Lawrence found a ~10% increase in segmentation accuracy using both the HH and HV channels relative to using only the HH channel (Yu et al., submitted); however, the improved segmentation accuracy can be partially attributed to the

improved segmentation of open water in the test scene. Nevertheless, this result indicates that ice typing might be improved using dual-pol data. Given the limited number of RADARSAT-2 scenes evaluated to date and the lack of field data to validate the results, further research is recommended.

2.5.2.3 Level and Deformed Ice Separation

The separation of level and deformed ice is a secondary requirement for operational ice centres and is an important consideration for ship routing decisions as deformed ice is thicker and therefore a greater hazard than level ice of the same stage of development. The ability to discriminate between level and deformed ice in single co-pol C-band SAR data is limited due to variations observed in co-pol signatures which cannot be related to surface roughness conditions with confidence (Arkett et al., 2006). Additionally, the orientation of ridges (relative to the radar look direction) and the fact that ridges are much smaller than the spatial resolution of ScanSAR data can affect the ability to resolve ridged ice. As a result, individual ridges cannot be mapped at the spatial resolution of ScanSAR data (Johnston, 2001). Given these limitations, the CIS does not report ridging or other ice deformation information in image analysis ice charts; however, there are indications that the separation of level and deformed ice may be improved at cross-polarizations as the random orientation of ice blocks is expected to increase multiple surface scatter (Scheuchl et al., 2004c).

Observations from airborne SAR data provide mixed results regarding the separation of level and deformed ice at C-band. Applying the unsupervised segmentation classifier of Rignot et al. (1992) to an AIRSAR scene from the Beaufort Sea, Rignot and Drinkwater (1994) found that the classification accuracy for FY rough ice using HV data was greater than using HH data; however, the increase in accuracy was marginal. When considering ice typing in addition to level and deformed ice separation the use of both HH and HV data provided superior results. Using the fully polarimetric data for this Beaufort AIRSAR scene Scheuchl et al. (2005) applied a Freeman-Durden decomposition classification (Freeman and Durden, 1998) to identify the dominant scattering mechanisms for the

various ice types present in the scene. For level FY ice surface scattering was dominant, while dihedral (double-bounce) scattering dominated only a small portion of the scene, mostly in ridged areas. The dominance of dihedral scattering in ridged areas suggests that backscatter from deformed ice should be greater than the backscatter from level ice at cross-polarizations. In agreement with this conclusion are the results of Flett (1997) who observed an increase in the contrast between smooth and rough FY ice in the cross-pol channels relative to the co-pol channels in CV-580 data acquired near Resolute. Flett (1997) also noted that the cross-pol ratio for FY rough ice was greater than that of FY smooth ice. In contrast to these results, Shokr et al. (1995) state that the cross-pol ratio has very little discriminating power for the separation of rough and smooth FY ice, due to the large variance observed in the cross-pol ratio data. While there is some disagreement, the majority of airborne SAR observations suggest that separation of level and deformed ice should be improved at cross-polarizations for C-band SAR data; however, these results cannot be assumed to be valid for spaceborne SAR data for two reasons. First, the spatial resolution of the airborne SAR systems is much higher than for wide swath spaceborne SAR. For example the spatial resolution of AIRSAR data is 6.6 by 11 m in the slant range and azimuth directions, respectively (Kwok et al., 1995), while that of RADARSAT-2 ScanSAR Wide data is nominally 100 by 100 m (MDA, 2009). Second, airborne systems have much lower NESZ than spaceborne systems. For example, AIRSAR has a NESZ of -35 dB (Drinkwater et al., 1991), relative to -28.5 dB for RADARSAT-2 (MDA, 2009). The higher NESZ of spaceborne SARs, which limits the lower end of the dynamic range of cross-pol data, may reduce the contrast between level and deformed ice relative to the airborne results.

Envisat/ASAR AP data have reduced spatial resolution (30 m) and a considerably higher noise floor (~-20dB) relative to airborne SAR systems, yet results show that level and deformed ice separation is still achieved at cross-polarizations. Analysis of AP data acquired at various swaths (IS1-IS6) in the vicinity of Resolute indicate that there is improved contrast between deformed ice

and level FY ice, and that deformed ice can easily be identified except during the melt period when the contrast is greatly reduced (Scheuchl et al., 2004c). Arkett et al. (2007) also note the improved identification of deformed ice in an image acquired along the Labrador Coast, a region where ice compaction is strong and deformed ice is common. Additionally, Arkett et al. (2006) state that the improved contrast between level and deformed ice can assist in the identification of floe boundaries, which are usually rough. As a result estimates of floe size and shape, both of which are useful for ice typing, can be improved; however, the increase in floe structure information is usually subtle (Arkett et al., 2006). The increase in floe structure detail is likely limited by spatial resolution. Given that Envisat/ASAR has a higher NESZ than RADARSAT-2 it can be assumed that system noise should not limit the separation of level and deformed ice for RADARSAT-2 ScanSAR data; however, the nominal spatial resolution of Envisat/ASAR AP data (30 m) is higher than that of RADARSAT-2 ScanSAR data (60 m for ScanSAR Narrow and 100 m for ScanSAR Wide), so these results cannot be assumed to be valid for ScanSAR data.

Flett et al. (2008) present one RADARSAT-2 ScanSAR image, acquired over Chaleur Bay in the Gulf of St. Lawrence, where rough ice features are present. Qualitative comparison between the HH and HV channels indicate that the contrast between level and deformed ice is improved in the HV channel. Once again, no field measurements were available to validate the interpretation of this image. In combination with the airborne SAR and Envisat/ASAR AP results, dual-pol RADARSAT-2 ScanSAR data is expected to provide improved separation of level and deformed ice although further evaluation is required to determine whether or not level and deformed ice can be separated on a reliable basis to permit the inclusion of deformed ice information in image analysis charts.

2.6 Conclusions

Based on the existing literature it is expected that cross-pol RADARSAT-2 ScanSAR data should provide several improvements over co-pol data (improved FY ice-open water separation and improved level-deformed ice separation); however, the cross-pol channel is also expected to have limitations relative to co-pol data (reduced separation of new ice from open water and reduced separation between new, young and smooth FY ice types). It is therefore anticipated that co- and cross-pol data should be used in tandem. It is important to note that these results are primarily based on airborne SAR and Envisat/ASAR AP data. Differences in radar parameters between these systems and RADARSAT-2 may impact these results. To date very few dual-pol RADARSAT-2 ScanSAR images have been evaluated and the interpretation of these data has not been validated with field measurements; therefore, further evaluation of the potential sea ice information provided by dual-pol RADARSAT-2 ScanSAR data is needed.

In this study extensive field data acquired during the Southern Gulf of St. Lawrence 2009 sea ice field survey (SGULF09) are available to assist in the interpretation of dual-pol RADARSAT-2 ScanSAR data. This study will build upon the results of Flett et al. (2008) by identifying and characterizing specific scenarios where the anticipated benefits and limitations of dual-pol RADARSAT-2 ScanSAR data can be thoroughly evaluated. Additionally, this study is focused on a marginal ice zone, the Gulf of St. Lawrence. This is important, as results to date have been biased to Arctic study sites while case studies in marginal ice zones are limited in number. Given that the level of human marine activity (commercial shipping, fishing, offshore infrastructure etc.) is much greater in mid-latitude marginal ice zones (Ramsay et al., 1993), there is a need for further study of dual-pol SAR observations of the ice regimes specific to these regions.

Chapter 3

Study Site, Data and Methods

3.1 Study Site

The data for this study were collected during SGULF09, a joint field campaign between the CIS and the Department of Fisheries and Oceans Canada (DFO). The field campaign was based in Charlottetown, Prince Edward Island (PEI), and data collection took place over the southern Gulf of St. Lawrence between February 24 and March 6, 2009. The CIS and DFO have undertaken sea ice field surveys in this region since 1996 on a nearly annual basis. A primary objective of these surveys is to validate SAR sea ice signatures and to support operational sea ice monitoring efforts (DFO, 2007). The location of oceanographic features and weather stations referenced in this thesis are provided in Figure 3.1.

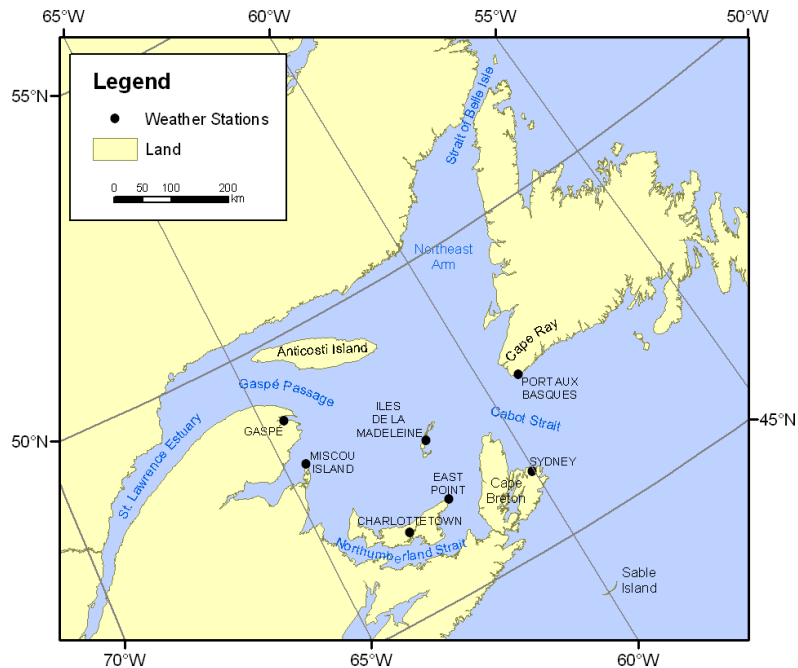


Figure 3.1: Oceanographic features and weather stations in the Gulf of St. Lawrence.

3.1.1 Physical Characteristics of the Gulf of St. Lawrence

The bathymetry, currents and tides of the Gulf of St. Lawrence play an important role in its ice regime. The bathymetry of the Gulf of St. Lawrence is well known and major features include the

Laurentian Channel and the Madeleine Shallows (Figure 3.2). The Laurentian Channel is a deep-water channel that extends from the St. Lawrence Estuary through Gaspé Passage (where it is about 200 m deep) and southeast across the Gulf and out into the Atlantic Ocean through Cabot Strait (where it is about 500 m deep). The northern limit of the Gulf is the Strait of Belle Isle, where the limiting depth is 50 m. South of the Laurentian Channel are the Madeleine Shallows, where depths are <75 m. In Northumberland Strait depths do not exceed 65 m. Bathymetry plays a significant role in the distribution of water masses within the Gulf, thereby affecting ice conditions, particularly in the Estuary where the inflow of deep warm Atlantic waters along the Laurentian Channel are brought to the surface by tidal upwelling (CIS, 2001). During SGULF09 field measurements were acquired over the Madeleine Shallows and Northumberland Strait.

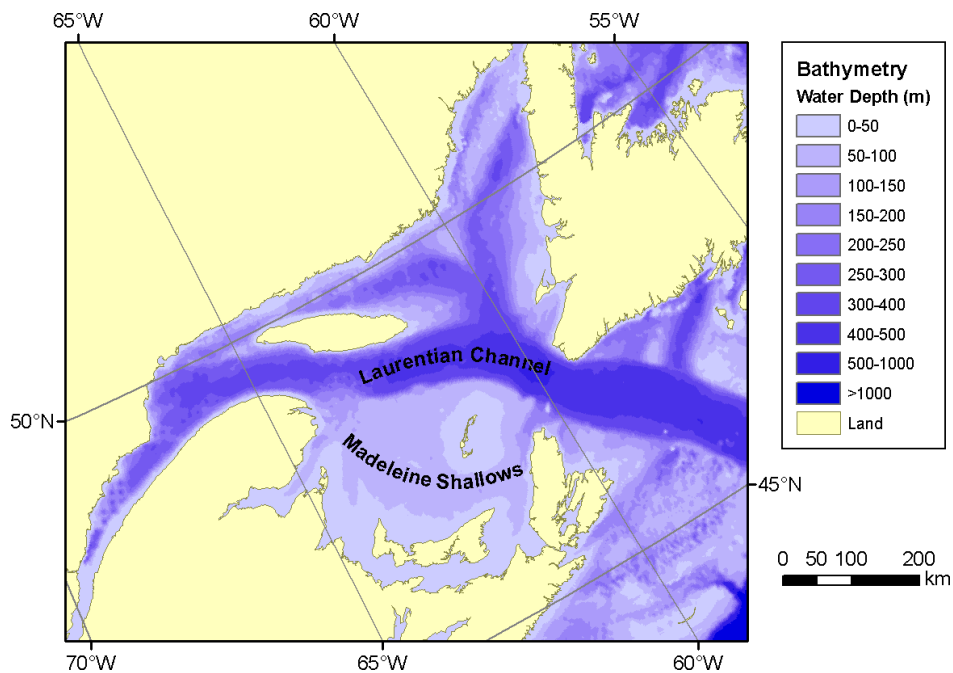


Figure 3.2: Bathymetry of the Gulf of St. Lawrence. Bathymetric data were provided by the National Oceanic and Atmospheric Administration (Amante and Eakins, 2001).

Currents in the Gulf of St. Lawrence generally move water eastward from the Estuary towards Cabot Strait (Figure 3.3). The currents are strongest along the shore of Gaspé Peninsula. In the southern Gulf, currents spread over the Madeleine Shallows, drifting towards Cabot Strait. Currents

also flow southeast across the Gulf above the Laurentian Channel. Upon reaching Cabot Strait currents sweep around Cape Breton and flow southwest along the Nova Scotian coast. On the north side of Cabot Strait there is a net inflow of water past Cape Ray, Newfoundland. In the Northeast Arm currents have a counter-clockwise pattern (CIS, 2001). These currents, in conjunction with surface winds, dictate the pattern of ice drift in the Gulf.

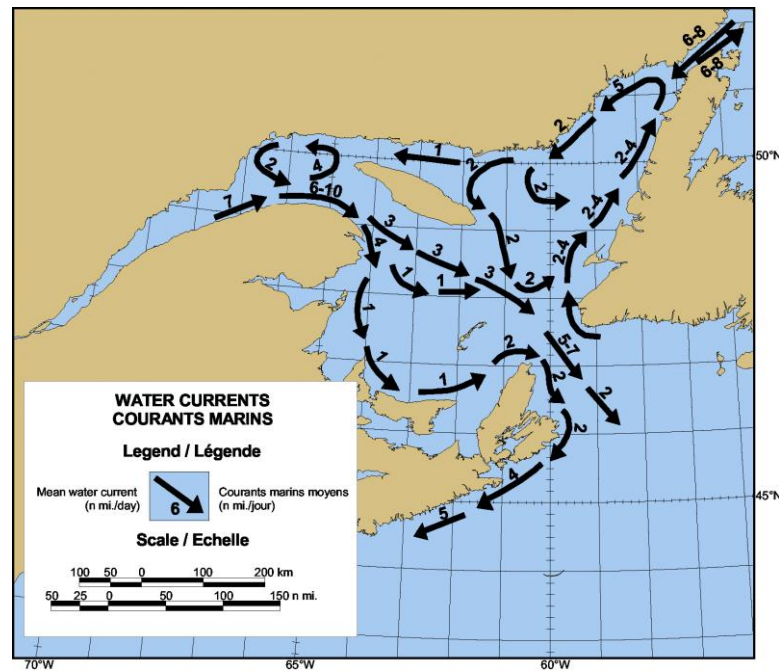


Figure 3.3: Water currents in the Gulf of St. Lawrence (adapted from CIS, 2001).

Tidal ranges in the Gulf of St. Lawrence vary considerably due to the geomorphology of the Gulf and because tidal surges enter from both Cabot Strait and the Strait of Belle Isle. Tides vary from as little as 0.7 m in the Iles de la Madeleine to 4.1 m in the southwest end of the St. Lawrence Estuary. Tides primarily impact the development of fast ice, with areas of low tidal ranges and shallow water depths typically producing wider areas of fast ice (CIS, 2001).

3.1.2 Ice in the Gulf of St. Lawrence

The Gulf of St. Lawrence is the southernmost region of Canada that experiences sea ice on an annual basis. The following sections introduce the ice regime of the Gulf of St. Lawrence and describe ice

conditions for the winter of 2008/2009. The discussion of the Gulf ice regime is derived from CIS regional ice charts from 1971-2000, as summarized in the *Sea Ice Climatic Atlas of the East Coast of Canada* (CIS, 2001). The discussion of the 2008/2009 ice season is derived from the *Seasonal Summary For Eastern Canada* (CIS, 2009).

3.1.2.1 Sea Ice Regime

There are two major climatic factors that control the ice regime of the Gulf of St. Lawrence. First, mean temperatures do not fall far below the freezing point. Thus cold or mild winters have a considerable impact on the extent and severity of ice. Second, the strength and direction of winds have a considerable impact on the areas of ice dispersal and congestion once ice has formed (CIS, 2001). The normal patterns of ice freezeup and breakup in the Gulf are illustrated in Figure 3.4. Here the term freezeup refers to the first appearance of ice (i.e. the date of freezeup for any given grid cell is the earliest date at which the 30-year median ice concentration $\geq 1/10$). The term breakup refers to the latest date at which ice is present (i.e. the date of breakup for any given grid cell is the latest date at which the 30-year median ice concentration is $\geq 1/10$).

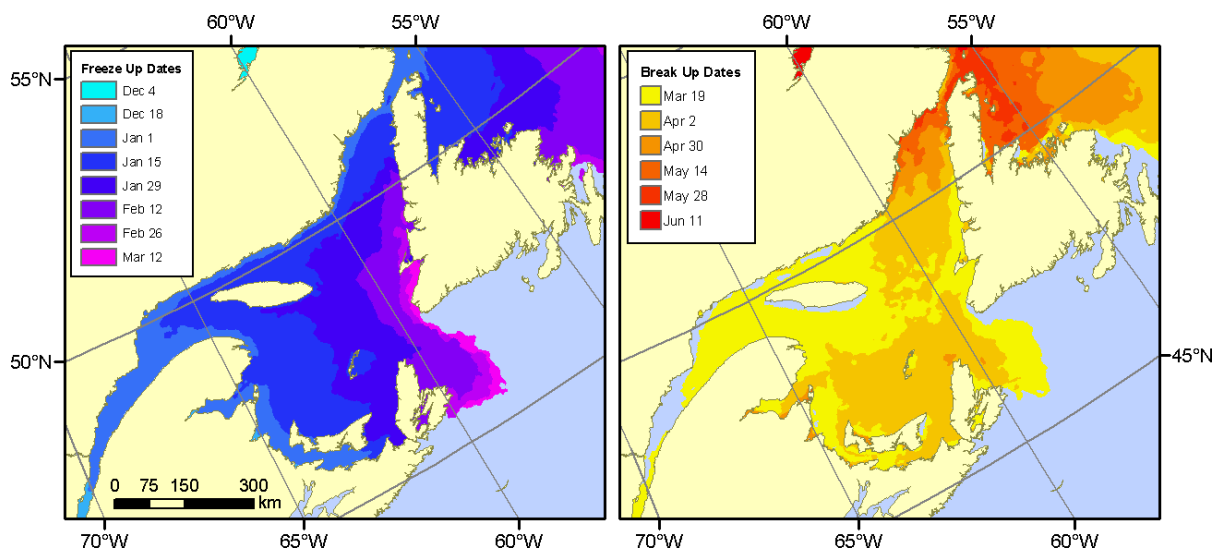


Figure 3.4: Median dates of sea ice freezeup and breakup in the Gulf of St. Lawrence, 1971-2000 (adapted from CIS, 2001).

Freezeup begins in December in the St. Lawrence Estuary where new ice forms in coastal regions and spreads seawards under the influence of currents and winds. In mid-December ice also forms in coastal shallows of the southern Gulf. By the end of December ice fills the Estuary, Northumberland Strait and Chaleur Bay, and ice is present in the Northeast Arm. At this time all ice is new or grey ice. In January ice growth proceeds eastward across the Gulf and south from the north shore. By the end of January ice reaches Cabot Strait, and much of the Gulf is ice covered. Ice is primarily new and grey, and grey-white ice begins to form. In early February the ice cover grows and thickens, filling the Gulf with predominantly grey-white and thin FY ice. In late February to mid-March ice reaches its maximum extent and continues to thicken through the FY stage of development and ice drifting through Cabot Strait is plentiful (CIS, 2001).

The dispersal of ice begins in late February, starting in the St. Lawrence Estuary where the upwelling of warm waters and inflow of warmer spring waters create openings in the ice cover. The presence of leads in the ice cover during spring are important due to the influence of the sea ice albedo feedback (leads act as centres of ice decay). In early March decreases in ice concentration are slow, but in the second half of March ice concentrations decrease at an accelerating pace. Grey-white and FY ice dominate the ice cover as thinner ice types melt faster. By early April the Estuary and the main shipping route through the Gulf (which roughly follows the Laurentian Channel) are ice free, separating ice in the southern Gulf from ice in the Northeast Arm. By mid-April the Madeleine Shallows are free of drifting ice, and coastal fast ice breaks up by mid-May. In the Northeast Arm, ice retreats slowly northwards. The entire Gulf is free of ice by the end of May. During the breakup period puddling on the ice surface is minimal, suggesting that decay is likely dominated by ablation on underside of the sea ice resulting from increasing water temperatures (CIS, 2001).

Ice floes in the Gulf are generally small compared to those in the Canadian Arctic. This is due to the dynamic nature of the ice pack. Ridging is extensive within the Gulf, although ridge sails seldom

exceed 2 m in height, except along windward shores. Given the predominant westerly winds and currents within the Gulf the mobile pack ice can exert considerable pressure on windward shores creating ridge sails up to 10 m. Large ridges are most common on the western shores of Cape Breton and the Iles de la Madeleine (CIS, 2001). While new, young and FYI are the predominant ice types observed in the Gulf it is possible for traces of MY ice and icebergs to be advected into the Gulf via the Strait of Belle Isle (CIS, 2001). While MY ice and icebergs are important from a navigational perspective, neither was present during SGULF09. As a result, they are not considered in this study.

3.1.2.2 Sea Ice Conditions in Winter 2008/2009

As is normal freezeup in the Gulf began in December. Temperatures were above normal across much of the Gulf in early December, although they were near normal in the Estuary, allowing ice growth to begin. Warm temperatures in the fourth week of December limited further ice growth, resulting in the total ice area being well below normal at the start of 2009 (Figure 3.5).

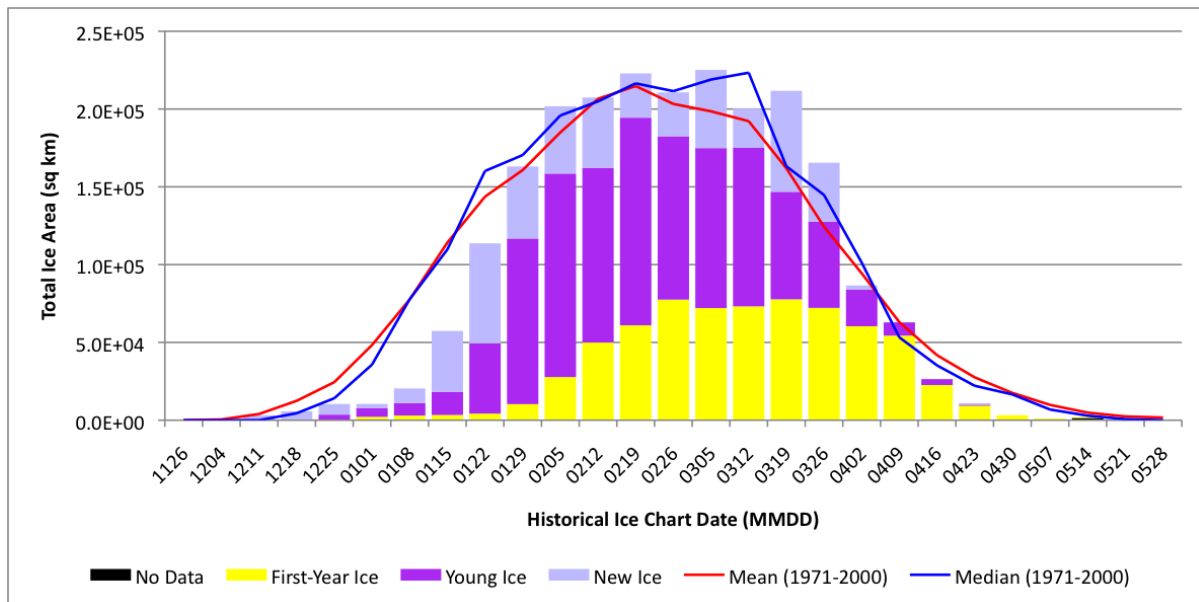


Figure 3.5: Weekly ice coverage in the Gulf of St. Lawrence, winter 2008/2009.

In the first half of January air temperatures and ice growth rates in the Gulf were near normal; however, total ice area remained below normal. In the second half of January air temperatures were

2° to 5° below normal accelerating ice growth rates. By the end of the month the total ice area and ice type distribution were near normal (CIS, 2009). By mid-February the Gulf was nearly ice covered, as is normal. In the second half of February air temperatures were 3° to 5° above normal limiting ice development. In the last week of February, which coincides with the start of SGULF09, a slight decrease in total ice area was observed. At this time the total ice area and the distribution of ice types were near normal values (Figure 3.6).

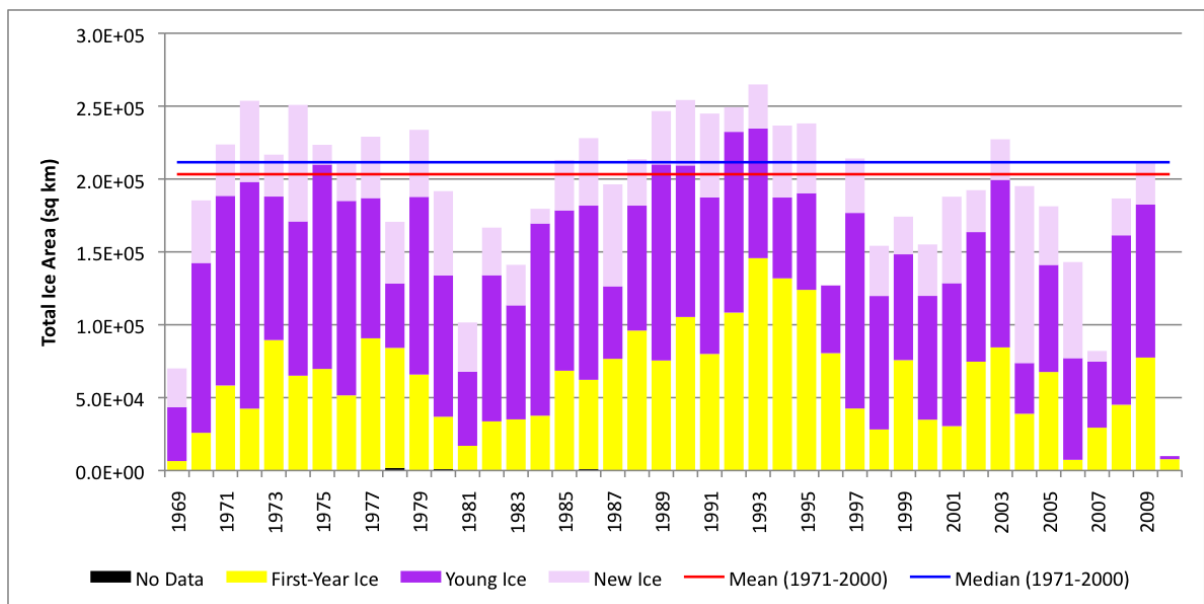


Figure 3.6: Historical ice coverage in the Gulf of St. Lawrence for the week of February 26, 1969-2010.

In the first half of March the total ice area and distribution of ice types remained near normal. Thus, the ice conditions during SGULF09 were ideal for data collection as they were representative of normal ice conditions in the Gulf at its maximum ice extent. In the second and third weeks of March strong winds from the west to northwest brought significant changes to the ice pack, flushing ice out of Cabot Strait and into the Atlantic Ocean. At this time the southern and eastern limits of the ice tongue reached near record limits and an ice hazard was issued for the Sable Offshore Energy Projects because of the encroaching ice tongue (CIS, 2009). Within the Gulf itself, the winds moved thick ice from the Estuary and Gaspé Peninsula region into the central Gulf. In early April above

normal air temperatures and southwest winds accelerated ice melt in the Madeleine Shallows. By mid-May all of the drifting and fast ice in the Gulf had melted (CIS, 2009).

3.2 SGULF09 Data Sets

During SGULF09, the CIS was responsible for acquiring and archiving satellite remote sensing data. SAR data from both RADARSAT-2 and Envisat were acquired and image analysis charts were created for each scene. The DFO was responsible for the acquisitions of field measurements, which were primarily collected using helicopter-borne remote sensing instruments.

3.2.1 Satellite Imagery

3.2.1.1 SAR Data

The primary data set for this study was dual-pol (HH/HV) RADARSAT-2 ScanSAR imagery. Additional single-pol (HH) RADARSAT-2 ScanSAR and Envisat/ASAR Wide Swath Mode (WSM) medium resolution data were also acquired. The RADARSAT-2 data include ScanSAR Narrow (SCN) A and B and ScanSAR Wide (SCW) A images. For all image acquisitions the SAR antenna was right looking. The SAR data are summarized in Table 3.1 and the SAR image footprints are shown in Figure 3.7.

Table 3.1: Summary of available SAR imagery.

Acquisition Date	Start Time (UTC)	Sensor	Beam Mode	Polarization	Orbit Direction
2009/02/26	10:30:22	RADARSAT-2	SCWA	HH	Descending
2009/02/26	21:52:00	RADARSAT-2	SCWA	HH, HV	Ascending
2009/03/01	22:04:02	RADARSAT-2	SCWA	HH, HV	Ascending
2009/03/02	10:14:07	RADARSAT-2	SCNB	HH, HV	Descending
2009/03/02	10:14:52	RADARSAT-2	SCNB	HH, HV	Descending
2009/03/04	22:16:54	RADARSAT-2	SCWA	HH	Ascending
2009/03/05	10:25:59	RADARSAT-2	SCWA	HH, HV	Descending
2009/03/05	10:27:13	RADARSAT-2	SCWA	HH, HV	Descending
2009/03/05	14:19:06	Envisat/ASAR	WSM	HH	Descending
2009/03/05	21:47:44	RADARSAT-2	SCNA	HH, HV	Ascending
2009/03/05	21:48:29	RADARSAT-2	SCNA	HH, HV	Ascending

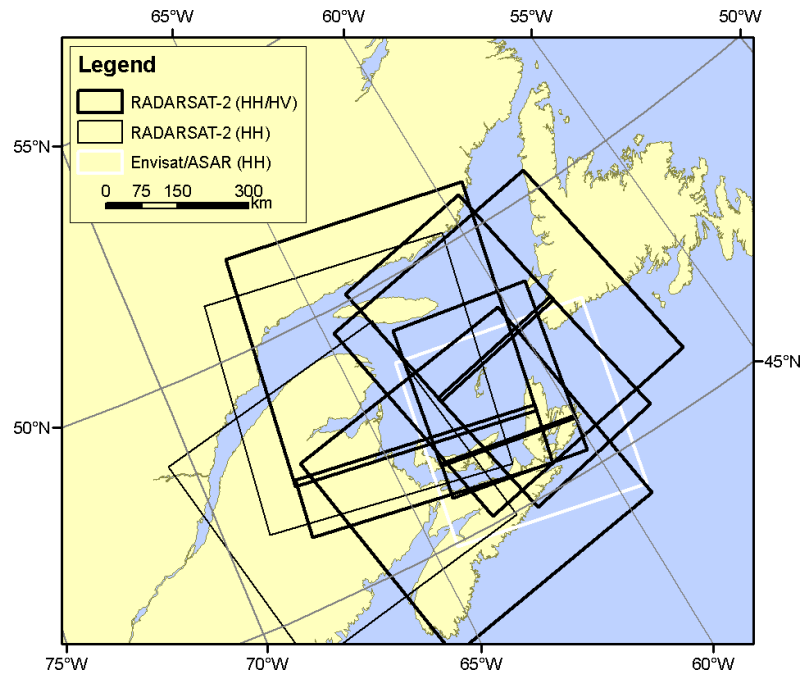


Figure 3.7: Image footprints for the SAR data acquired during SGULF09.

The SAR data were georeferenced and calibrated to sigma nought backscatter coefficients (σ°). This processing was done using PCI Geomatica v10.3.0 for the RADARSAT-2 data, and the Next ESA SAR Toolbox v3C for the Envisat/ASAR data.

Given the changes in orbit track between acquisitions and that both ascending and descending data were acquired, backscatter from specific ice features can be evaluated at various incidence angles where features can be identified in multiple images. The image characteristics for each beam mode, including incidence angle range, are summarized in Table 3.2.

Table 3.2: Summary of RADARSAT-2 and ENVISAT/ASAR beam mode characteristics (MDA, 2009; ESA, 1998).

Sensor	Beam Mode	Nominal Pixel Spacing (m)	Resolution Range x Azimuth (m)	Nominal Swath Width (km)	Incidence Angle Range (degrees)	No. of Looks Range x Azimuth
RADARSAT-2	SCNA	25	79.9-37.7 x 60	300	20-39	2 x 2
RADARSAT-2	SCNB	25	79.9-37.7 x 60	300	31-26	4 x 2
RADARSAT-2	SCWA	50	160.0-72.1 x 100	500	20-49	4 x 2
Envisat/ASAR	WSM	75	150 x 150	400	17-42	N/A [†]

[†]The number of range and azimuth looks for ASAR WSM were not available; however, ESA (1998) reports the equivalent number of looks as ~11.5.

3.2.1.2 Visible-Infrared Data

In addition to the SAR data, visible-infrared satellite remote sensing data acquired by the Moderate Resolution Imaging Spectroradiometer (MODIS), onboard the Terra and Aqua satellites, were available. Two or more MODIS images were available over the Gulf of St. Lawrence each day during SGULF09; however, cloud cover was common during the study period, limiting the number of useful MODIS images. Table 3.3 lists the MODIS images acquired on days where RADARSAT-2 data were available and where some portion of the Gulf of St. Lawrence was cloud free.

Table 3.3: Summary of MODIS images with limited cloud cover.

Acquisition Date	Ordinal Date	Acquisition Start Time (UTC)	Platform
2009/02/26	057	15:30	Terra
2009/02/26	057	17:15	Aqua
2009/03/04	063	14:50	Terra
2009/03/05	064	15:35	Terra
2009/03/05	064	17:25	Aqua

The MODIS data are Version 5 MOD02HKM and MYD02HKM products, which are Level 1B calibrated radiance data from the MODIS/Terra and MODIS/Aqua systems, respectively. The spatial resolution of these products is 500 m. The data were georeferenced and bow tie corrected using the MODIS Conversion Toolkit, available from the ITT Visual Information Solution Code Library¹.

¹ <http://www.itervis.com/UserCommunity/CodeLibrary.aspx>

In addition to the Level 1B data, Level 2 Sea Ice Extent products (MOD29/MYD29) were also available. The MOD29/MYD29 data are provided at a spatial resolution of 1 km. These products contain two sea ice extent datasets. This first dataset identifies snow covered sea ice using the normalized difference snow index (NDSI). This algorithm identifies snow covered sea ice based on its reflectance properties (Hall et al., 2001); however, new ice with no snow cover will not be identified using the NDSI criteria. As a result, a second dataset is included which identifies sea ice based on surface temperature estimates (Riggs et al., 1999). By combining these products a classified image is created where each pixel is classified as sea ice, open water, cloud, or land. The sea ice class is subdivided into sea ice identified by both algorithms, sea ice identified only by the reflectance (NDSI) criteria, and sea ice identified only by the Ice Surface Temperature (IST) criteria.

3.2.2 Field Data

During SGULF09 field data were collected primarily from helicopter-borne instruments and airborne visual observations. This section outlines the ice charts created during the campaign, the helicopter-borne remote sensing instrumentation and data, the ice drift data provided by ice buoys and by the CIS Ice Tracker, and meteorological data recorded at Environment Canada (EC) weather stations.

3.2.2.1 Ice Charts

For each SAR image acquired during SGULF09 (Table 3.1) CIS Ice Analysts created an image analysis chart. In addition to the image analysis charts, reconnaissance ice charts were created in the field during SGULF09 by ISS onboard CCG icebreakers, helicopters and DASH-8 aircraft. The observed ice charts were created on an opportunistic basis and as a result the spatial and temporal coverage of these reconnaissance charts vary. At least one icebreaker reconnaissance chart was available for each day during the field campaign; however the spatial coverage of these charts is the most limited, with the nominal width of observations along ship tracks being 8 km wide. Icebreaker

charts were produced most frequently within Northumberland Strait and in the vicinity of the Iles de la Madeleine. Helicopter reconnaissance charts were created on February 25, 26, and 27. For each date the observations covered a flight line between PEI and the Iles de la Madeleine. The nominal width of the helicopter observations was 35 km. Airborne reconnaissance charts were created on March 1, 4 and 6. The nominal width of the airborne observations was 40 km (for clear sky conditions). While the spatial coverage of the observed ice charts increases with increasing altitude of the observer platform, the level of detail that the ISS can observe is reduced (MSC, 2005).

3.2.2.2 Helicopter-borne Instrumentation and Data

The primary platform for the collection of field measurements during SGULF09 was a CCG BO-105 helicopter. Two remote sensing instrument systems were attached to the helicopter. The first was a fixed-mounted electromagnetic (EM) induction system coupled with a laser altimeter. This EM system is colloquially referred to as the IcePic and was used to collect ice thickness and surface roughness measurements. The second instrument was a nadir looking video system, used to collect geotagged video stills of ice conditions along the helicopter flight path.

The IcePic is a cigar-shaped sensor package that is fixed to the nose of a helicopter. It contains two sensors from which estimates of ice thickness and surface roughness can be derived. The first component of the IcePic is an EM induction system, which measures the distance from the IcePic to the nearest conductive surface (the ice-seawater interface). The EM induction system is comprised of transmitter and receiver coils (transmitter frequencies of 1.7, 5.0, 11.7 and 35.1 kHz) with a coil separation of 1.2 m. The transmitter coil produces a primary magnetic field that induces eddy currents in nearby conductors (in this case seawater). The induced eddy currents then generate a secondary magnetic field that is sensed by the receiver coils. A proprietary nonlinear inversion model is then used to calculate the distance to the ice-seawater interface. The footprint of the EM induction system is ~2.5 times the altitude of the sensor above the seawater (Prinsenberget al., 2002; 2008). The

nominal flying altitude during IcePic data collection was 5 m. The second component of the IcePic is a laser altimeter, which measures the distance from the IcePic to the ice (or snow) surface. The laser altimeter has a listed accuracy of 1.5 cm and the laser footprint is a few centimetres. The IcePic also contains an attitude sensor, which is used to compensate for the effects of roll and pitch on the laser altimeter measurements (Prinsenberget al., 2008). Ice (plus snow) thickness h_i is calculated according to the equation

$$h_i = h_{EM} - h_L \quad (3.1)$$

where h_{EM} is the distance from the IcePic to the ice-seawater interface, as measured by the EM induction system, and h_L is the distance from the IcePic to the ice (or snow) surface, as measured by the laser altimeter. IcePic ice thickness measurements have been shown to be accurate to 0.1 m over level ice (Prinsenberget al., 2002); however, the thickness of deformed ice measured with EM induction systems is generally underestimated. This underestimation has two causes. First, the footprint of the EM induction system is greater than the size of most ridges. Second, ridge keels can include pockets of seawater, which act as conductive surfaces (Haas et al., 1997). Ice (or snow) surface roughness, defined as the height of the ice (or snow) surface relative to the surrounding level ice (or snow) surface, are also calculated from the laser altimeter data (Peterson et al., 2008). The sampling rate of the IcePic is 10 Hz, resulting in a nominal spatial sampling interval of ~5 m for the normal helicopter survey speed of 100 mph (Prinsenberget al., 2002).

The nadir pointing digital video camera was installed in a pod attached to the helicopter skid and it was connected to the helicopter's radar altimeter and global positioning system (GPS). The video camera has a 6 mm lens with a horizontal field of view of 56.1° and a vertical field of view of 43.6°. The width of the collected video frames is 1.07 times the flying height of the video camera (Lalumiere, 2000). During SGULF09 the camera was set to collect video frames at a resolution of 640 by 480 pixels. At a nominal flying altitude of 90 m the ground width of each video frame is ~96

m and the pixel size is ~0.15 m by 0.15 m. The video camera acquired 100 frames per minute and the approximate scene centre and flying altitude for each frame were recorded from the helicopter's onboard GPS and radar altimeter, respectively. During video data collection a much greater altitude is required relative to the IcePic system. A greater altitude is required in order to produce video frames that cover a reasonable sea surface area, to ensure overlap between successive video frames, and to reduce blurring in the image data. During SGULF09 the overlap between successive frames, which is dependent on the helicopter speed and altitude, was generally on the order of 30%. Due to the varying altitude requirements of the IcePic and video systems, video data and IcePic data could not be collected simultaneously. The location of IcePic and video data profiles acquired during SGULF09 is provided in Figure 3.8.

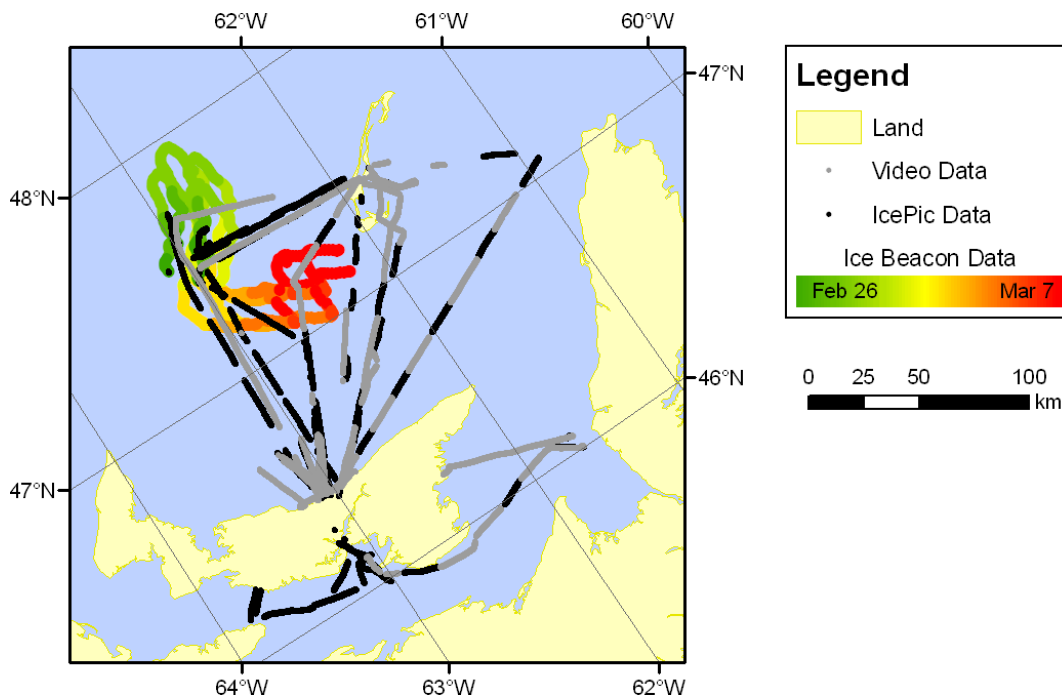


Figure 3.8: The location of IcePic and video data profiles and GPS ice beacon data acquired during SGULF09.

Given that the IcePic and video systems were operated from a helicopter these data could not be acquired in inclement weather conditions. Furthermore, both the IcePic and video systems require favourable illumination conditions. During IcePic data collection it is too dangerous to collect data

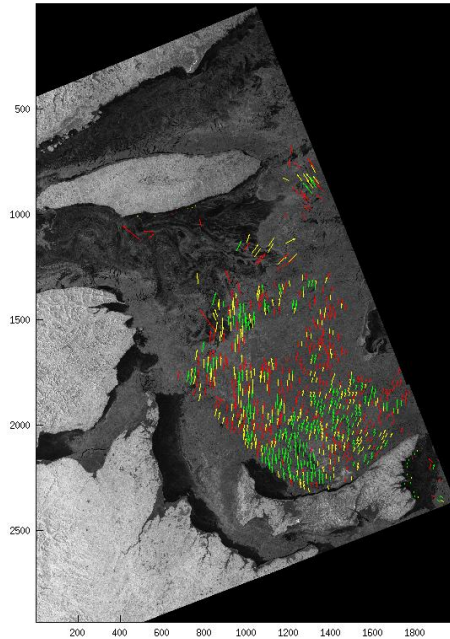
during flat-light conditions as the topography of the ice is poorly defined and the pilot cannot safely operate the helicopter at such low altitudes. During video data collection poor illumination conditions adversely affect the quality of the video data. These factors limit IcePic and video data collection to daylight hours. RADARSAT-2 data were acquired earlier (~10:30 for descending passes) or later (~22:00 for ascending passes) than the IcePic and video data. Note that all times are provided in UTC. As a result, there was usually a difference of several hours between the acquisition of the field data and the SAR data. Ice drift data was therefore required to determine the direction and speed of ice motion between the acquisition of the IcePic and video data and the RADARSAT-2 data.

3.2.2.3 Ice Drift Data

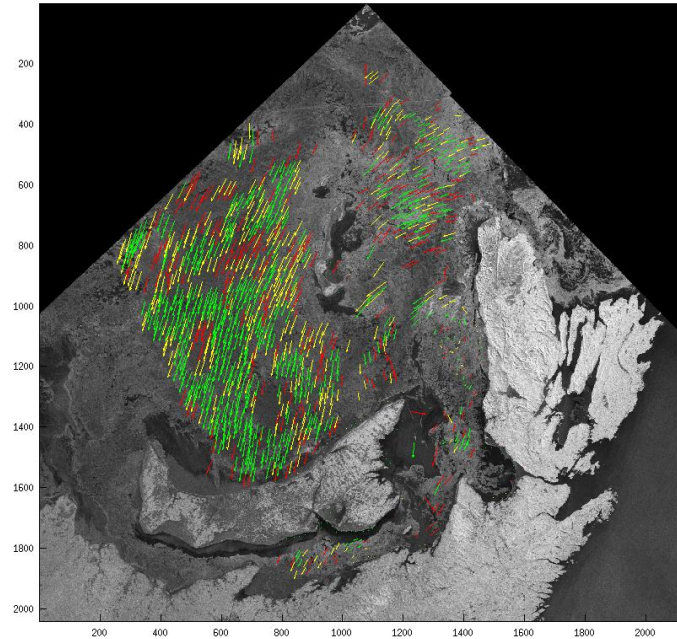
Ice drift data during the field campaign were collected using four Iridium Ice Beacons. The ice beacons, which were deployed on February 26 at 18:00, recorded hourly GPS locations throughout the field campaign. The GPS data were transmitted to a private website via the Iridium satellite system. The beacons, which were deployed for a study of the Gulf of St. Lawrence harp seal population, were placed in a square formation around the seal whelping grounds. Given that the beacons were primarily tasked for seal research, the ice beacons provided only limited spatial coverage of ice drift within the SGULF09 study domain (Figure 3.8). As a result, ice drift data were also generated using the CIS Ice Tracker algorithm developed by Alexander Komarov (unpublished). The ice tracker operates on two sequential SAR images resampled to 100 m grid cell spacing. The algorithm takes into account two components of ice movement, parallel shift and rotation, based on the properties of a two-dimensional Fourier transform (A. Komarov, personal communication, May 14, 2010). The tracker outputs displacement vectors for ice features that are resolved in both of the input images, and assigns a confidence level (low, medium or high) to each output vector. While the tracker drift data provided wider spatial coverage than the ice beacons, the tracker data are limited to areas of overlap in the input image pairs and they provide only the start and end points of ice drift

between the acquisition times of each input image. Ice drift vectors were produced for three image pairs. The tracker was run on additional image pairs but no confident ice motion could be derived due to extended time lags (2 to 3 days) between the input images. The output drift vectors for the three successful image pairs are provided in Figure 3.9.

a) Feb 26 10:30z --> Feb 26 21:52z



b) Mar 1 22:04z --> Mar 2 10:14z



c) Mar 5 10:25z --> Mar 5 21:47z

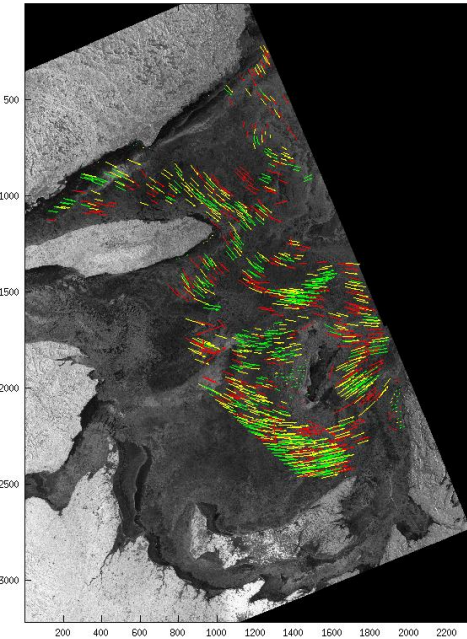


Figure 3.9: CIS Ice Tracker output. Red, yellow, and green arrows represent ice displacement vectors with low, medium and high confidence, respectively. RADARSAT-2 data and products © MacDonald, Dettwiler and Associates Ltd 2009 – all rights reserved.

3.2.2.4 Meteorological Data

Hourly air temperature, wind speed and wind direction data as well as daily total precipitation data were collected from EC weather stations located around the Gulf of St. Lawrence (Figure 3.1). Air temperatures during SGULF09 were fairly consistent spatially across the southern Gulf of St. Lawrence and the mean air temperature was -6°C ; however, three periods of positive air temperatures were recorded (Figure 3.10).

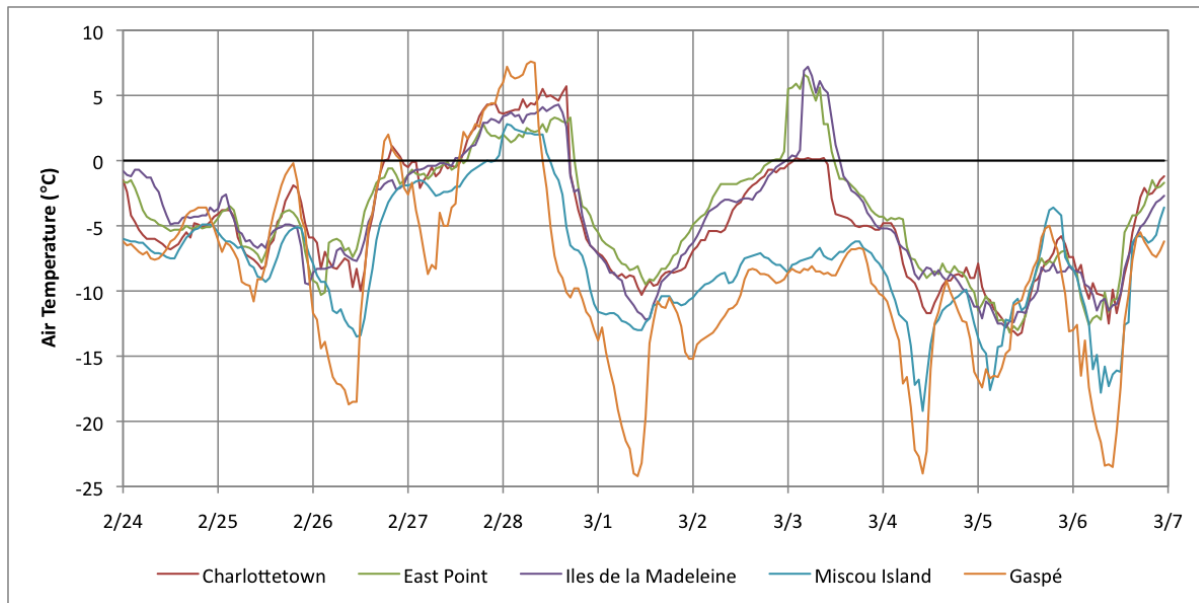


Figure 3.10: Hourly air temperature data recorded at EC weather stations around the southern Gulf of St. Lawrence, February 24 (00:00) to March 6 (23:00).

On February 26 (18:00-22:00), positive air temperatures were recorded at Gaspé and Charlottetown, although the maximum air temperature during this event was only 2.0°C . The longest period of positive air temperatures was between February 27 (12:00) and 28 (18:00). During this time positive air temperatures were recorded at all weather stations in the southern Gulf and the maximum air temperature was 7.6°C (recorded at Gaspé). The third period of positive air temperatures was recorded between March 2 (21:00) and 3 (13:00), although air temperatures in the western Gulf (Gaspé and Miscou Island) remained well below 0°C at this time. The maximum air temperature during this event was 7.2°C (recorded at the Iles de la Madeleine).

Precipitation during SGULF09 was concentrated primarily in one large storm event that occurred between February 28 and March 3. Over these four days a mix of snow, freezing rain and light rain showers were reported at EC weather stations. Rain was only reported on February 28, and snow and freezing rain were reported on March 1, 2 and 3. The precipitation was heaviest on March 2 with the greatest quantity of freezing rain falling at Charlottetown (37.6 mm). In contrast to the freezing rain observed at Charlottetown, weather observations for Gaspé reported only snowfall (19 cm) on March 2. Aside from this storm event on March 2, only trace amounts of precipitation were recorded.

Despite the fact that there were periods of positive air temperatures and there was a major storm event, the field log (DFO, 2009) does not report any significant changes to sea ice properties over the course of the campaign and melt features (puddles, melt ponds) were never reported. In the field log entry for March 4 (the first flight following the March 2 freezing rain event) the field log specifically notes that there were no significant changes to the ice conditions. Sea ice backscatter signatures were stable throughout SGULF09 and the textural and tonal variations of sea ice signatures were never masked by the presence of a wet snow pack. The observed stable backscatter signatures are in part due to the fact that positive air temperatures were recorded only at the acquisition time of one RADARSAT-2 image (February 26, 21:52), and in this case air temperatures were barely $>0^{\circ}\text{C}$. While saline snow can melt at temperatures below 0°C , the air temperatures recorded in the southern Gulf at the acquisition time of each of the remaining SAR images were $<-5^{\circ}\text{C}$. Given the low air temperatures and observed stable backscatter signatures it is likely that the snow conditions can be considered dry for the C-band SAR data. The ice conditions observed in the RADARSAT-2 data are therefore winter ice conditions.

Winds during SGULF09 were variable (temporally), both in speed and direction. Spatially winds were reasonably consistent across the southern Gulf, with the exception of winds measured at Gaspé, which were calmer (Figure 3.11).

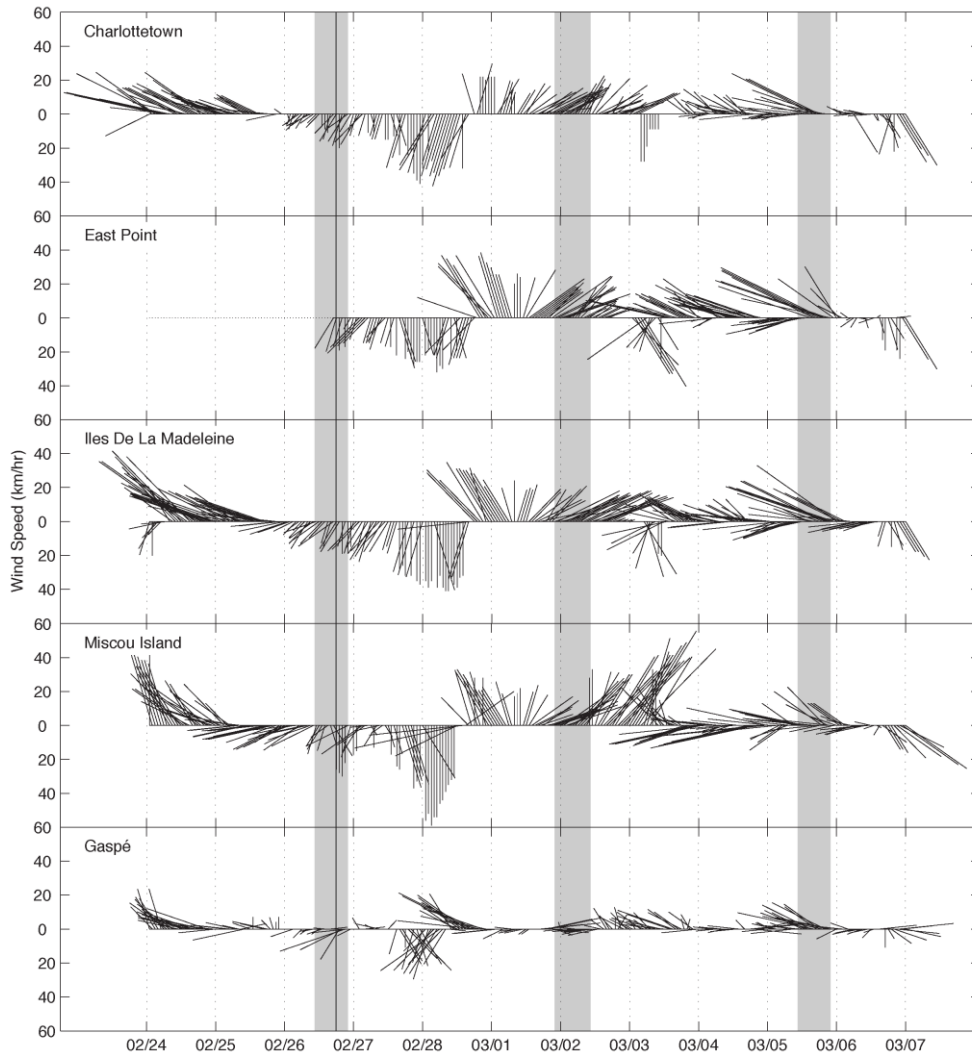


Figure 3.11: Hourly winds in the southern Gulf of St. Lawrence, February 24 (00:00) to March 6 (23:00). The wind data for each hour is plotted as a black line with the wind direction represented by the angle of the line and the wind speed represented by the length of the line. The vertical reference line (February 26, 18:00) corresponds to the onset of ice beacon GPS data collection. The shaded areas correspond to the time intervals of the Ice Tracker image pairs.

There is good agreement between the wind data, the ice beacon drift pattern and the Ice Tracker drift vectors throughout the southern Gulf of St. Lawrence. This agreement suggests that it is

appropriate to use wind data to estimate the direction of ice drift in the absence of ice beacon or ice tracker data.

3.3 Methods

In order to identify what new sea ice information is provided by the dual-pol RADARSAT-2 ScanSAR data, relative to single co-pol data, both qualitative and quantitative analysis was performed to assess the HH and HV backscatter signatures of open water and new, young and FY ice.

3.3.1 Evaluating Ice and Open Water Discrimination

To evaluate the separability of ice and open water in dual-pol RADARSAT-2 ScanSAR data, an understanding of the HV backscatter signature of open water was required. Backscatter values from open water were therefore extracted from across the full ScanSAR swath width and analysed. To achieve this images in which open water spanned the full image width for some lines were identified and backscatter profiles were extracted. To reduce the effects of speckle, ten consecutive image lines were extracted and the mean backscatter for each column was computed from the power backscatter values (effectively increasing the number of looks). The backscatter signatures for both the HH and HV channels were extracted and plotted to compare the effect of incidence angle on the co- and cross-pol backscatter signature of open water. In addition to determining the impact of incidence angle on HV backscatter from open water, the effects of the NESZ needed to be evaluated. To determine if the HV backscatter from open water was at, below, or above the NESZ, the HV imagery was visually assessed to determine if ocean surface features (e.g. wind fronts) could be identified or if system and processing artefacts dominated the backscatter signatures. Once the HV backscatter signature of open water was defined the separability of ice and open water could be assessed. This assessment was broken down into two components, an evaluation of the ability to delineate the ice edge, and an evaluation of the ability to estimate ice concentrations within the pack ice.

The ability to delineate the ice edge from HH or HV data was first assessed visually. The contrast between ice and open water was evaluated at various wind speeds and incidence angles in order to determine if image conditions existed where the visual contrast between ice and open water was greater in the HV channel than in the HH channel. Given that the ice edge was located in Cabot Strait during SGULF09, IcePic and video data were not available to validate the position of the ice edge as visually interpreted from the SAR data; therefore, the delineation of the ice edge was compared to MODIS data. The ice edge was visually identified in the MOD02HKM data and qualitatively compared to both the HH and HV RADARSAT-2 image data and derived image analysis charts.

The MOD02HKM data were viewed both as a true colour composite (MODIS bands 1, 4, 3; centre wavelengths: 670 nm, 565 nm, and 479 nm) and as a false colour composite (MODIS bands 3, 6, 7; centre wavelengths: 565 nm, 1652 nm, 2155 nm). In the true colour composite terrestrial, oceanic and atmospheric features appear their natural colours (i.e. as if seen by the naked eye). In this composite, ice is readily identifiable but can be confused with clouds. The false colour composite was used to separate ice and snow from clouds. Ice and snow are characterized by strong reflectance in the visible spectrum and strong absorption at shortwave infrared (SWIR) wavelengths, causing them to appear red using this band combination. Liquid water on the ground strongly absorbs at all of these bands, causing it to appear black, while liquid water in clouds scatters light equally at visible and SWIR wavelengths causing clouds to appear white (NASA, 2010). To aid in the interpretation of the MOD02HKM data, MOD29 sea ice extent data were also used. MOD29 data could not be used in place of the MOD02HKM data for two reasons. First the spatial resolution of the MOD29 data (1 km) is lower than that of the MOD02HKM data (500 m). Second, the cloud-masking algorithm was found to be extremely conservative, meaning that many areas with thin or sparse clouds were masked in the MOD29 data when the presence (or absence) of sea ice could still be determined through visual analysis of the MOD02HKM data.

To assess the ability to estimate ice concentration from dual-pol RADARSAT-2 data, areas of the mobile pack ice where the HH backscatter signatures were ambiguous were identified. For these areas the backscatter signatures of the HH and HV data were visually compared and field data (video data and observed ice charts) were used to validate the ice and open water signatures observed in the two channels. Using these data, HH and HV ice and open water backscatter signatures were characterized for various incidence angles and wind speeds to identify conditions at which the addition of the cross-pol channel is likely to improve ice concentration estimates. While the initial evaluation of the dual-pol data was performed using separate greyscale images for each polarization, the dual-pol data were also visualized as a false colour composite (R-HH, G-HH, B-HV) to determine whether or not the open water and sea ice information from each channel could effectively be synthesized in a colour composite. This band combination was selected as it is the most prevalent colour composite used in the existing literature for visualizing dual-pol SAR data (e.g. Scheuchl et al., 2004c; Arkett et al., 2006; Peterson et al., 2006; Flett et al., 2008).

3.3.2 Evaluating Ice Typing

In order to evaluate the ice type information provided by dual-pol RADARSAT-2 data, ice type distributions reported in image analysis chart egg codes were compared to transects of IcePic ice thickness data acquired within the corresponding ice polygons. IcePic data have previously been used to validate ice type signatures for single co-pol C-band SAR data (e.g. Prinsenberget al., 1996; Prinsenberget al., 2002; Peterson et al., 2008). For each image analysis chart created during SGULF09, IcePic data collected on the same day were identified and ice polygons within which IcePic data had been collected were identified. Ice drift data were then taken into consideration to determine if any profiles of IcePic data were acquired that fell completely within a single ice polygon. Once coincident IcePic and egg code data were identified the ice type distribution listed in the egg code could be compared to the IcePic ice thickness measurements. To facilitate this comparison, ice

type histograms were created from the egg code and IcePic data. The IcePic ice type histogram was created by binning the ice thickness measurements into classes that correspond to the thickness ranges defined by the WMO for each ice type. These thickness ranges are provided in Table 2.1. Assuming perfectly level ice conditions the egg code histogram and IcePic histogram should match if the egg code correctly defines the ice types (and their partial concentrations); however, consideration needs to be given to deformed ice, which could bias the IcePic histogram towards thicker ice types. Additionally, the IcePic data are collected only along transects within the ice polygons and may not be representative of the ice conditions across the entire polygon.

In order to more accurately interpret the IcePic data, a second histogram, which bins the IcePic data in 10 cm intervals, was created. This equal interval histogram provides a more detailed view of the ice thickness distribution measured by the IcePic. After the results of Prinsenberget al. (1996) and Peterson et al. (2008) this histogram can be interpreted as follows. The modal value of this histogram is expected to represent the modal level ice thickness, assuming that level ice is more common than deformed ice along the IcePic profile. Where ice is heavily deformed the ice thickness distribution is likely to be broad and bimodal, with the thinner mode representing the modal level ice thickness and the thicker mode representing the modal deformed ice thickness.

Once the IcePic and egg code data had been compared the backscatter signatures for specific ice types could be identified with certainty in the SAR data. Once the ice types were identified, the ice type information provided by each of the HH and HV channels was visually compared to identify whether or not the cross-pol channel contained any information not provided by the co-pol channel that may be of benefit for ice type mapping. Once again the HH and HV channels were combined into a false colour composite and the resulting imagery was visually assessed relative to the individual greyscale images to determine if the synthesis of the channels provides any further ice type information.

3.3.3 Evaluating Level and Deformed Ice Discrimination

The separability of level and deformed ice in the dual-pol RADARSAT-2 ScanSAR data was assessed in two ways. First, given that deformed ice is expected to generate strong HH and HV backscatter, bright (high backscatter) features were identified in the RADARSAT-2 imagery and field data (IcePic and video data) collected over these features were used to determine whether or not the ice that caused the bright radar returns is deformed ice. Video data were used to identify areas of level ice, rafted ice and ridged ice, while IcePic data were used to quantify the ice thickness and surface roughness of the bright ice features. Once the ice properties that caused the high backscatter had been identified, regions of interest (ROIs) were digitized over these bright features and over level ice, and backscatter statistics (mean and standard deviation) for each ROI were derived. In order to reduce the impact of speckle on the retrieved statistics each ROI was at least 1000 pixels in size. The backscatter signatures for each bright ice ROI and level ice ROI were then compared to quantitatively determine the separability between these ice features.

Given that the first method of identifying deformed ice features is dependent on the dual-pol backscatter it was critical to use alternative datasets to identify regions of deformed ice independent of the SAR data in case level and deformed ice are not separable in the dual-pol data. On observed ice charts the egg code reports the concentration of ridged ice for each digitized ice polygon allowing areas of ridged ice to be identified without considering the SAR data. Observed ice charts created within a few hours of RADARSAT-2 data acquisitions were identified. The ice polygons from these observed ice charts were then used as ROIs to extract backscatter statistics from the RADARSAT-2 data. The backscatter signatures were then compared to the concentration of ridged ice reported on the observed ice charts to determine whether or not the concentration of ridged ice within an ice polygon is correlated to the HH or HV backscatter amplitude.

Chapter 4

Results and Discussion

4.1 Introduction

In this chapter the image quality and sea ice information content of dual-pol RADARSAT-2 ScanSAR images acquired during SGULF09 are evaluated. The accuracy of the image analysis charts (produced primarily from visual interpretation of the RADARSAT-2 data) is also qualitatively evaluated. The accuracy of daily ice analysis charts and regional ice charts is not assessed as additional remote sensing data sources (e.g. MODIS, NOAA/AVHRR) are incorporated in the production of these charts. For the image analysis charts the accuracy of three ice parameters is evaluated. Each of these parameters is a primary requirement for operational ice monitoring. They are the ice edge location, ice concentration, and stage of development. Following the evaluation of these primary requirements, the dual-pol RADARSAT-2 data are analysed to determine whether or not reliable ice deformation information (a secondary tactical requirement) can be derived.

4.2 Ice and Open Water Discrimination

As discussed previously the discrimination of ice and open water can be difficult using single co-pol SAR data. This can reduce the accuracy of both manual and automated ice-open water classifications, and can therefore impact the accuracy of the ice edge location and ice concentration estimates in image analysis charts. During SGULF09 this limitation of co-pol data was best exemplified by the Envisat/ASAR image acquired March 5 at 14:19 (Figure 4.1). Note that all data acquisition times are given in UTC.

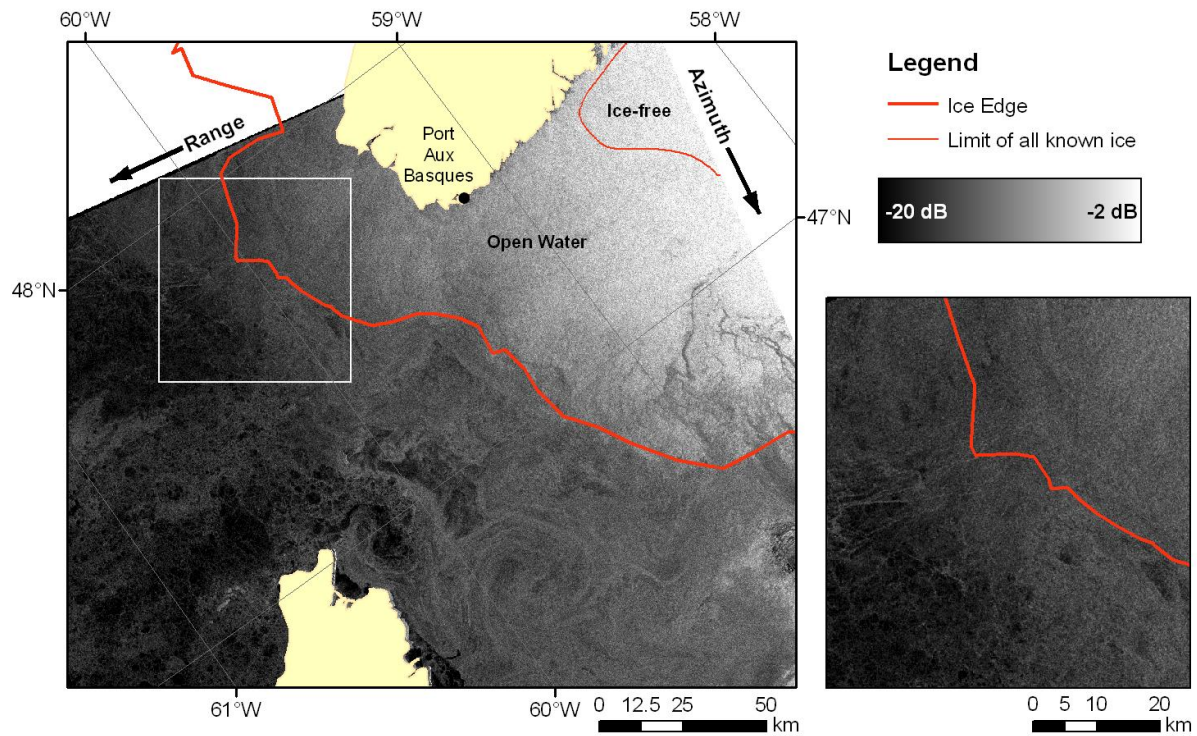


Figure 4.1: Poor discrimination between ice and open water in the near range of an Envisat/ASAR WSM HH image (March 5, 2009, 14:19). The ice edge and limit of all known ice are derived from the corresponding CIS image analysis chart. The image subset on the right is 60 km tall and 57 km wide. Envisat data © ESA 2009.

There is considerable confusion between open water and ice in the near range of this image. The area of poor discrimination covered incidence angles from 19° to 28° . The poor separation of ice and open water was particularly evident in the northern portion of Cabot Strait. Wind speeds measured at Port Aux Basques at 14:00 were 46 km/hr (13 m/s) from the west-northwest. Compared to the modelled backscatter values of Nghiem and Bertoina (2001; Figure 2.3) open water backscatter observed in this scene was low (it agrees well with the modelled backscatter for winds of 2 m/s). Additionally, the backscatter from sea ice, which was identified as primarily thin FY ice in the image analysis chart, was considerably higher than the FY ice backscatter values of Nghiem and Bertoina (2001). These observed signatures result in a crossover at much steeper incidence angles than predicted by the models used by Nghiem and Bertoina (2001). These observations are in agreement with operational experience at the CIS where it has been found that ice-open water confusion is most

frequently observed in the near range (Arkett et al., 2006). These results suggest that the wind model implemented by Nghiem and Bertoia (2001) may require further research, while the input parameters for the sea ice backscatter model likely were not representative of the ice conditions observed in this image.

The poor contrast between ice and open water in the ASAR image was reflected in the corresponding image analysis chart. The delineation of the diffuse ice edge, beyond which water is open ($<1/10$ ice concentration), was extremely generalized. The location of the limit of all known ice, beyond which water is ice-free, appears to have been drawn rather conservatively, perhaps a result of the low confidence in ice-open water discrimination in this area. The poor image quality and associated low confidence in the position of the ice edge was noted in an annotation on the image analysis chart for this ASAR image. Unfortunately, given that this ASAR image was acquired using the WSM beam mode, only the HH channel was available; therefore, an evaluation of the ice-open water discrimination at cross-polarizations was not possible. As discussed in Section 2.5.2.1 the addition of a cross-pol channel in dual-pol RADARSAT-2 ScanSAR acquisitions is expected to improve the separation of ice and open water as the cross-pol backscatter from open water is expected to be stable across range.

4.2.1 Dual-polarization Backscatter From Open Water

For each of the dual-pol RADARSAT-2 ScanSAR images acquired during SGULF09 the backscatter from open water was found to be range dependent in the HH channel and stable across range in the HV channel (e.g. Figure 4.2).

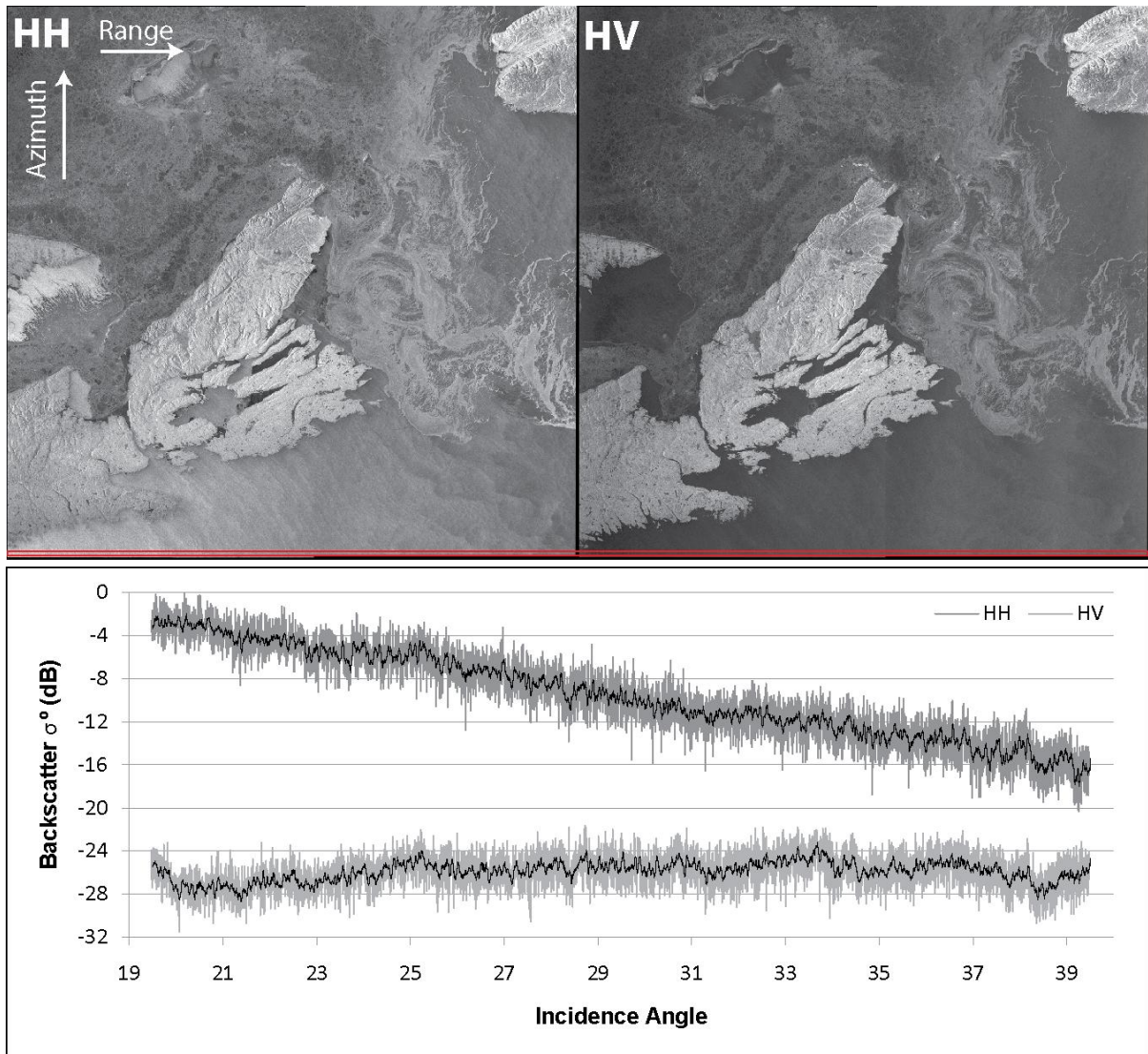


Figure 4.2: HH and HV ocean backscatter in a RADARSAT-2 SCNA image (March 5, 21:47). Plotted grey lines are mean backscatter for ten image lines (L12201-L12210) of open water across the bottom of the image. The red box indicates the location of the averaged image lines. The plotted black lines are moving averages with a period of 25 samples. RADARSAT-2 data and products © MacDonald, Dettwiler and Associates Ltd 2009 – all rights reserved.

In this SCN image the HV backscatter from open water was typically between -24 to -28 dB across the full swath, while HH backscatter decayed across range from about -3 dB in the near range to -17 dB in the far range. Similar results were observed across the larger incidence angle range of SCW (Figure 4.3).

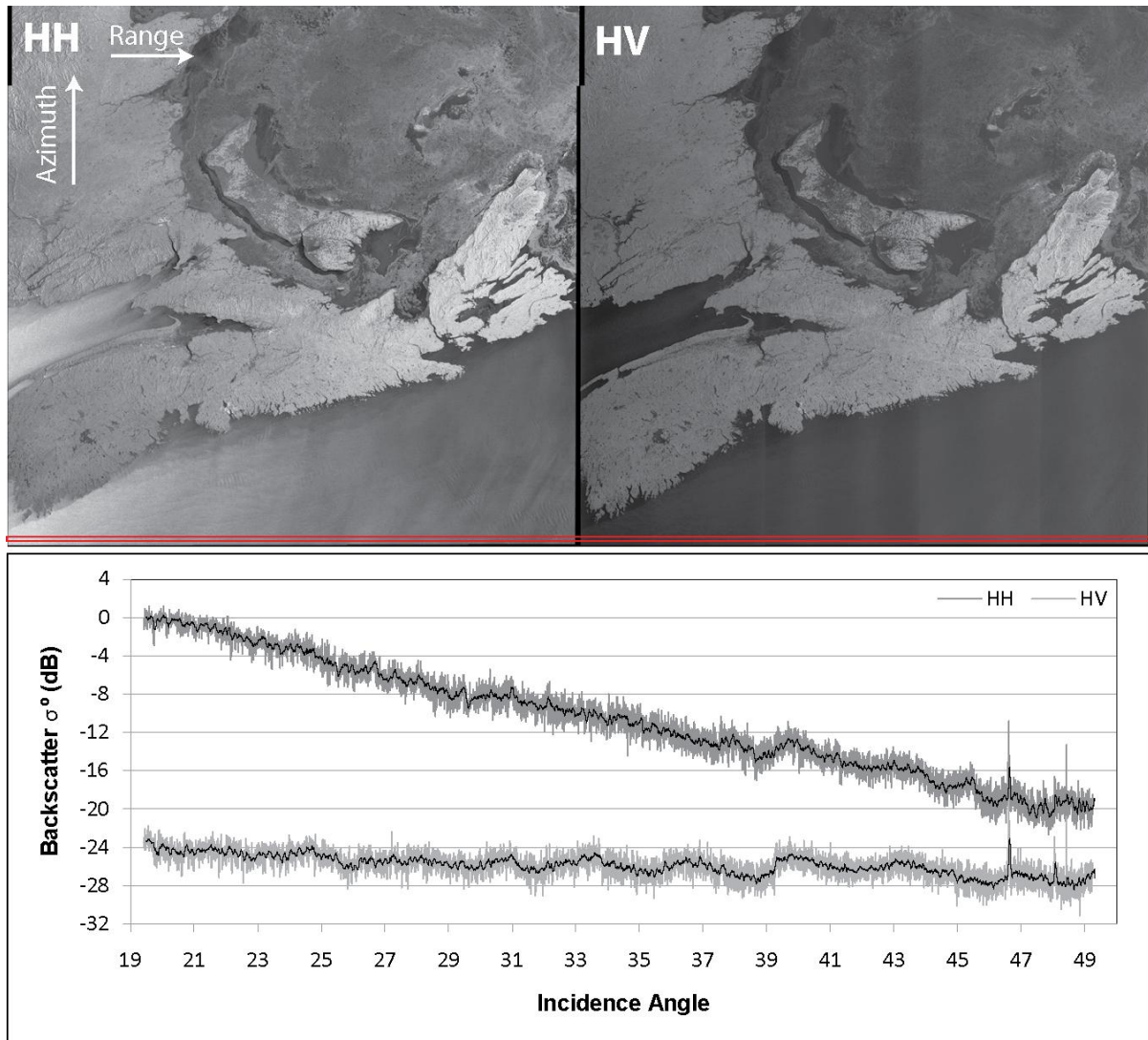


Figure 4.3: HH and HV ocean backscatter in a RADARSAT-2 SCWA image (March 1, 22:04). Plotted grey lines are mean backscatter for ten image lines (L10081-L10090) of open water along the bottom of the image. The red box indicates the location of the averaged image lines. The plotted black lines are moving averages with a period of 25 samples. RADARSAT-2 data and products © MacDonald, Dettwiler and Associates Ltd 2009 – all rights reserved.

Even across the larger incidence angle range of the SCWA swath the HV backscatter from open water effectively remained within the range of -24 to -28 dB; however, at shallow incidence angles (>45°) the signal may be noise limited as it is almost as low as (and within the uncertainty of) the NESZ (-28.5 ± 2 dB). The HH backscatter varied from approximately 0 dB in the near range to -20 dB in the far range. Three sharp increases in HV backscatter were observed in the far range, two of which

were observed in the HH data. These features, which are near Sable Island, were located in the image and appeared to be ships or possibly offshore developments. The sharp increase in backscatter associated with these point targets is expected since they would act as corner reflectors (which create strong co- and cross-pol returns). While these two images (March 1, 22:04; March 5, 21:47) were the only acquisitions in which open water spanned the entire swath for some image lines, results from isolated areas of open water in the remaining images also indicated that HV backscatter from open water is stable across range with typical values of -24 to -28 dB.

In both of the HV images presented, some distinct vertical features were visible. These features are system and processing artefacts. Some of these features were distinct vertical lines, which were identified as beam seams, an artefact of the ScanSAR imaging process. The most noticeable beam seam is located in the SCWA image at 39° where a sharp increase in backscatter is observed (Figure 4.3). This is the seam between the Wide 2 and Wide 3 beams incorporated into the SCWA swath. In addition to the beam seams, 'rolls' were observed at certain incidence angles in the HV images. It is believed that these rolls are related to antenna elevation pattern corrections. These rolls were most noticeable between 31° and 39° , where two rolls were observed in both the SCNA and SCWA images (Figure 4.2; Figure 4.3). For these two ScanSAR modes, this incidence angle range is imaged using the Wide 2 beam. Similar roll artefacts, which were attributed to antenna elevation pattern corrections, were noted previously in Envisat/ASAR HV data over open water (Scheuchl et al., 2005). Beam seams and rolls were observed over open water in the HV channel in each of the RADARSAT-2 swaths acquired during SGULF09. The appearance of these artefacts indicates that the SNR for open water is low in the RADARSAT-2 HV ScanSAR data; however, some ocean surface features (e.g. wind fronts), which were visible in the HH channel, could be identified in the HV channel. This result suggests that the backscatter from open water is, at least for portions of the ScanSAR swaths, not completely limited by the NESZ. This finding is in agreement with those of Olsen et al. (2010)

who have observed wind fronts, convection cells and other ocean features across large portions of RADARSAT-2 ScanSAR swaths in cross-pol images of the Norwegian, Greenland, and Barents Seas. Using fine beam quad-pol data, which has a lower NESZ (-36.5 ± 3 dB) than ScanSAR data (-28.5 ± 2 dB), Vachon and Wolfe (2010) have shown that cross-pol backscatter from open water is essentially independent of incidence angle and wind direction, and that it is related to wind speed by a simple power law.

The HV backscatter from open water was greater than the noise floor of the RADARSAT-2 ScanSAR data, although it was low but stable across range. This suggests that a range dependent crossover with backscatter from ice should not occur; however, if the backscatter from any given ice type is as low as that from open water, discrimination would be reduced across the entire swath in the HV channel.

4.2.2 Identification of the Ice Edge

In each of the dual-pol RADARSAT-2 ScanSAR images acquired during SGULF09 the discrimination between ice and open water in the HH channel was acceptable (i.e. none of the images contained large regions within which the separation of ice and open water was unclear). Several factors contributed to this observation. First, the majority of the Gulf was ice covered throughout the study period; therefore, few areas of open water were present, and most were small, isolated areas in the lees of Anticosti Island, the Iles de la Madeleine, and PEI. Second, when open water was observed it was usually in the very near (or far) range where ocean clutter was usually much higher (or lower) than the HH backscatter from ice. The only large area of open water imaged during SGULF09 was along the eastern edge of the mobile ice pack in Cabot Strait. This ice edge was imaged in three dual-pol RADARSAT-2 images (February 26, 21:52; March 2, 10:14; and March 5, 21:47). In the

February 26 (21:52) and March 5 (21:47) images the ice edge was in the far range. In the March 2 (10:14) image the ice edge was in the near range.

For the February 26 (21:52) image the HH backscatter from open water was very low (<-20 dB) at the shallow incidence angles of the far range (35° - 49°), allowing for the ice edge to be easily delineated using HH data alone. The position of the ice edge from the associated image analysis chart was qualitatively compared to MYD02HKM and MYD29 data (Figure 4.4).

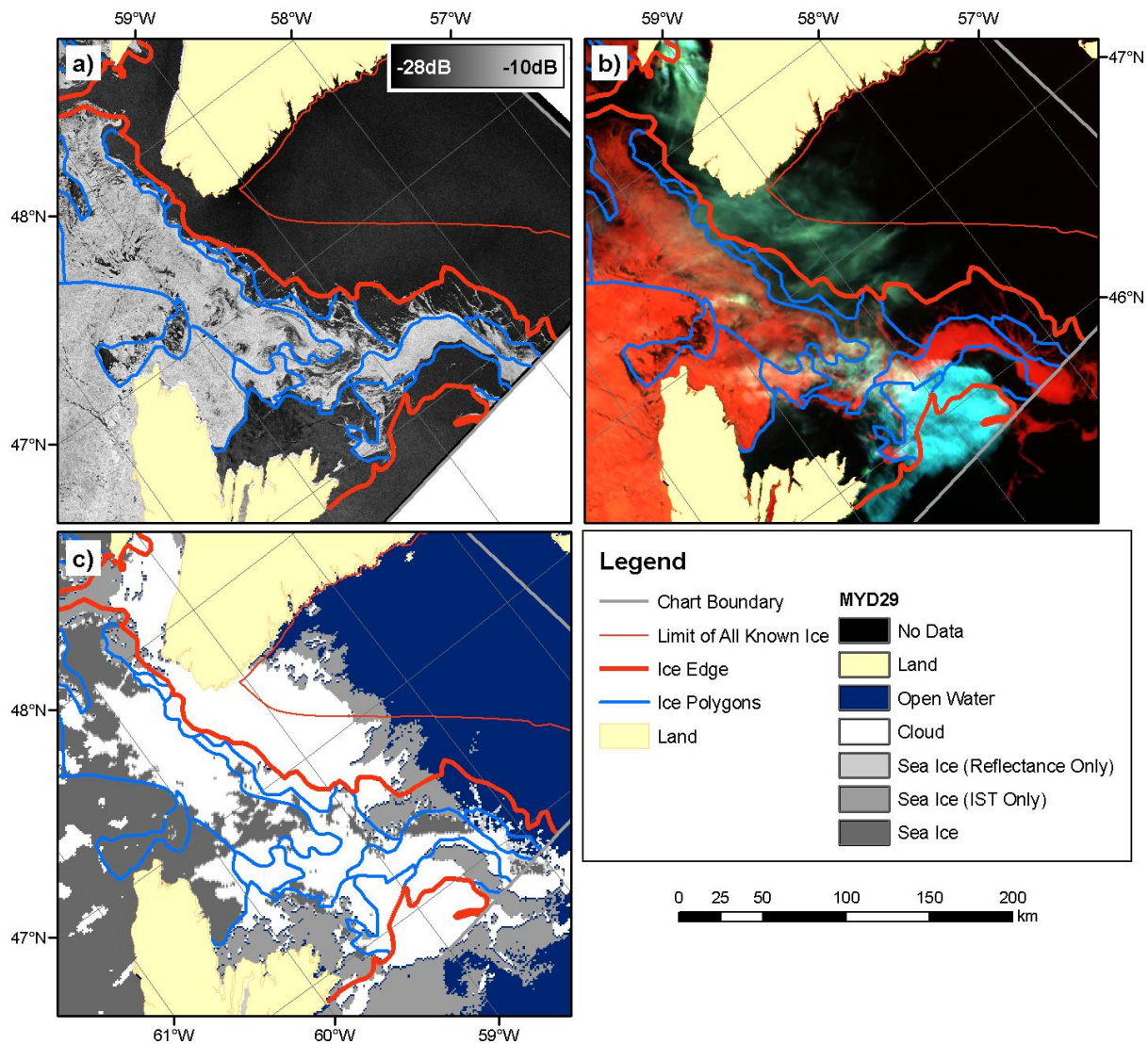


Figure 4.4: The ice edge in Cabot Strait on February 26 as observed in a) RADARSAT-2 SCWA HH data (21:52), b) MODIS/Aqua 367 false colour composite (17:15), and c) MYD29 sea ice extent data (17:15). Vector data are from the CIS image analysis chart created from the HH+HV SCWA data. RADARSAT-2 data and products © MacDonald, Dettwiler and Associates Ltd 2009 – all rights reserved.

Considering the time lapse between the RADARSAT-2 and MODIS data acquisitions, there was excellent visual agreement between the image analysis chart ice edge and ice polygon boundaries and the ice visible in the MYD02HKM false colour composite. There was also excellent agreement with the reflectance based MYD29 sea ice extent data. No pixels beyond the image analysis chart's ice edge were identified as sea ice according to the MYD29 reflectance criteria; however, there is

considerable disagreement between the SAR data (and image analysis chart) and the IST based MYD29 sea ice extent. According to the MYD29 IST criteria, sea ice was present in high concentrations well beyond the image analysis chart's ice edge, and even beyond the chart's limit of all known ice. Any MYD29 pixels identified as ice according to the IST criteria only are expected to be new ice because new ice has a much lower albedo than thicker (and usually snow-covered) ice types and therefore will not meet the reflectance criteria (Hall et al., 2001).

There are two possible explanations for the disagreement between the SAR interpreted ice edge and the MYD29 IST data. The first is that the MYD29 IST product overestimates the extent of new ice. There are two factors that could contribute to such an overestimation. First, the accuracy of IST retrievals is estimated to be 0.3 to 2.1 K (Key et al., 1997); therefore, open water near the freezing point could be misclassified as ice. Second, even under clear-sky conditions the presence of water vapour can further impact the accuracy of the IST retrievals (Hall et al., 2001). The second explanation for the disagreement between the image analysis chart and the IST data is that new ice and open water could not be discriminated in the SAR image for the observed conditions (wind speed, imaging geometry); however, new ice can clearly be identified in the HH image immediately north of Sydney, Cape Breton. This new ice is reported in the image analysis chart, with the total concentration for this ice polygon being 5/10. Given that new ice near the ice edge was separated from open water in this area, it is probable that the IST data overestimate the extent of new ice in this case. Unfortunately no field data were available to further assess the disagreement between these datasets. IcePic and video data were unavailable as this area was beyond the range of the helicopter based in Charlottetown, and no observed ice charts were produced in this area until March 6. Assuming that the IST data overestimate the presence of new ice, the HH SAR data provided excellent visual separation between ice and open water. The separation between FY ice and open

water was also excellent in the HV data as the ocean clutter was very low (<-24 dB); however, the new ice observed just north of Sydney could not be identified in the HV data (Figure 4.5).

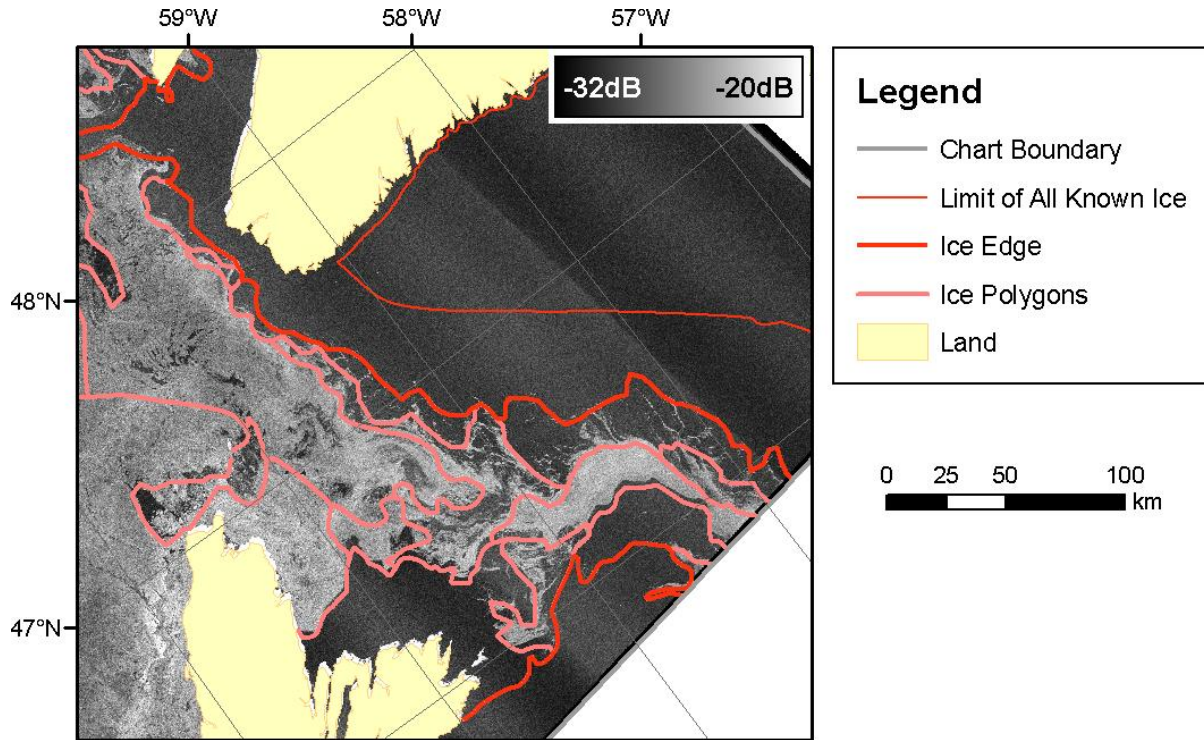


Figure 4.5: The ice edge in Cabot Strait on February 26 as observed in RADARSAT-2 SCWA HV data (21:52). Vector data are from the CIS image analysis chart created from the HH and HV SCWA data. RADARSAT-2 data and products © MacDonald, Dettwiler and Associates Ltd 2009 – all rights reserved.

In this case both open water and new ice were at or below the noise floor in the HV data; therefore, the HV channel provides reduced ice-open water discriminating power relative to the HH channel, although both provide excellent visual separation between FY ice and open water.

In the March 5 (21:47) image similar results were observed. Both the HH and HV channels provided good separation between FY ice and open water, and new ice could only be identified in the HH channel. In contrast to the February 26 (21:52) image, the ocean clutter was much higher on March 5. As a result there was reduced visual contrast between ice and open water in the HH channel (Figure 4.6).

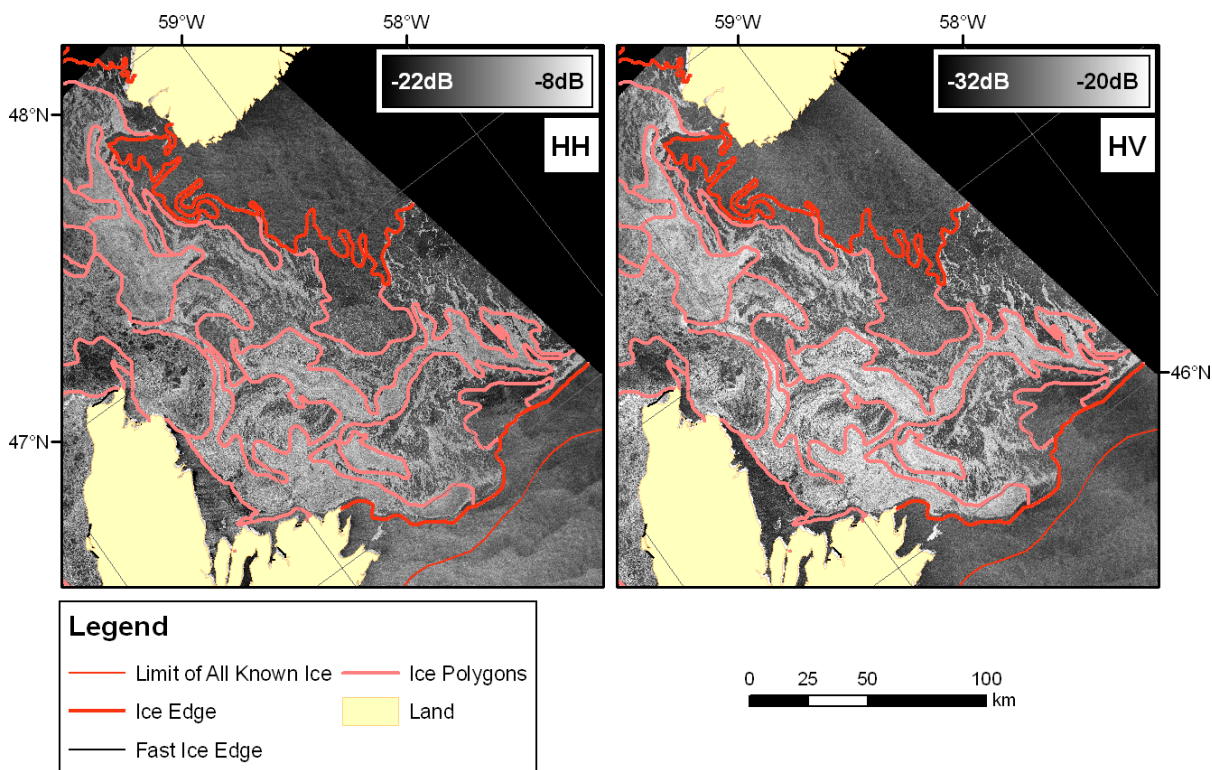


Figure 4.6: The ice edge in Cabot Strait, March 5, as observed in dual-pol RADARSAT-2 SCNA imagery (21:47). Vector data are from the CIS image analysis chart created from the SCNA data. RADARSAT-2 data and products © MacDonald, Dettwiler and Associates Ltd 2009 – all rights reserved.

The increase in HH ocean clutter in this scene is a combination of imaging geometry and wind speed. This image is a SCNA acquisition, so even though the ice edge was in the far range it was imaged at steeper incidence angles (33°-39°) than in the SCWA February 26 image. Second, wind speeds were higher. Wind speeds measured at Sydney were 17 km/hr on March 5 (22:00), compared to 11 km/hr on February 26 (23:00). While these factors contributed to a reduced visual contrast between ice and open water in the HH data relative to the February 26 image, the ice edge could still be identified with confidence from the HH data alone. Once again, new ice could not be accurately identified in the HV data; however, the visual contrast between FY ice and open water was greater in the HV channel than in the HH channel. The image analysis chart ice edge could not be compared to MODIS data due to the presence of clouds. An observed ice chart created during a DASH-8 flight the

following day was available and the ice edge from this observed chart was in good agreement with that of the image analysis chart.

In the March 2 (10:14) SCNB image the ice edge was located in the near range (31°-35°). In this image the ice edge was compact with the exception of some strips of ice in the northern portion of the image. Compared to the February 26 and March 5 images, the ocean clutter was high in the HH image. This is attributed to the steeper incidence angles at which the ice edge was observed. Wind speeds (15 km/hr measured at Port-Aux-Basques at 10:00) were comparable to the previous images. While the ice edge could be clearly delineated in either the HH or HV imagery, the HV channel once again provided improved visual contrast between FY ice and open water, particularly for the strips of FY ice in the northern portion of the image (Figure 4.7).

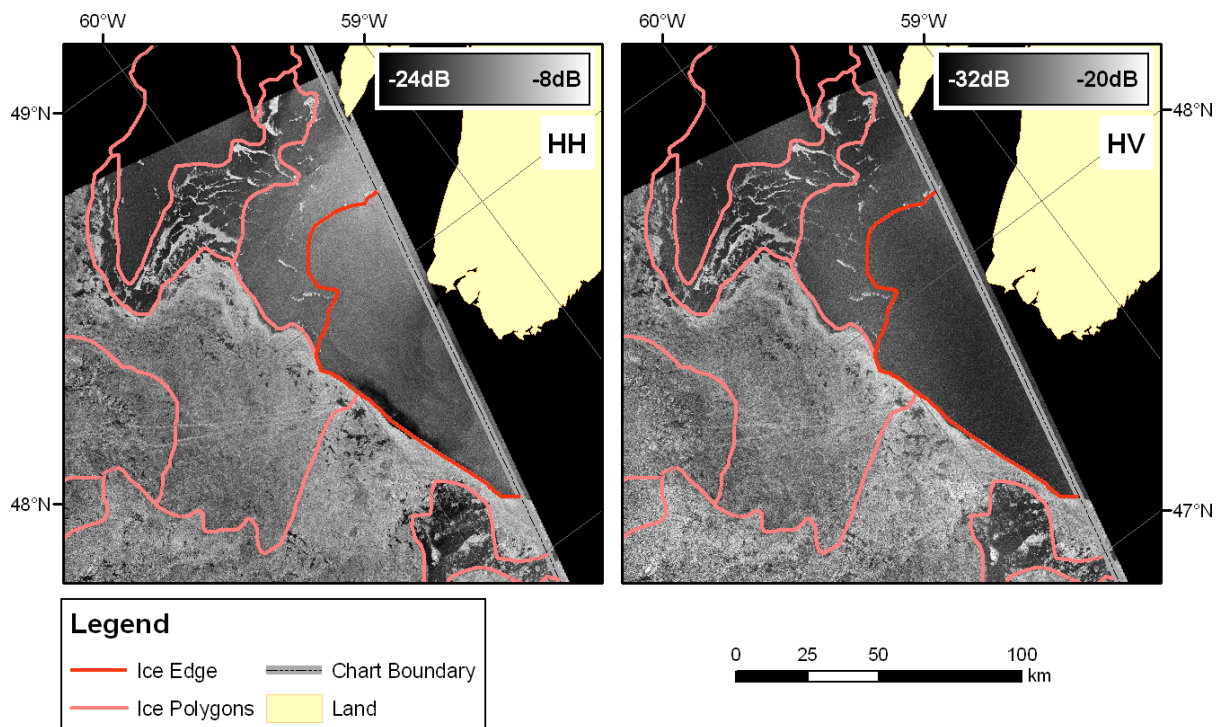


Figure 4.7: The ice edge in Cabot Strait as observed in dual-pol RADARSAT-2 SCNB imagery (March 2, 10:14). Vector data are from the CIS image analysis chart created from the SCNB data. RADARSAT-2 data and products © MacDonald, Dettwiler and Associates Ltd 2009 – all rights reserved.

While the delineation of the ice edge from the SAR data appears accurate, validation data sets were again lacking (MODIS data were cloudy and no observed ice charts were available in this region).

Results from these three images indicate that for wind speeds ≤ 17 km/hr and incidence angles $\geq 31^\circ$ the HH channel alone should provide sufficient visual contrast between ice and open water for the ice edge to be delineated with confidence. While the HH channel was sufficient for ice and open water discrimination for these image conditions, the HV channel provided improved visual contrast between FY ice and open water when incidence angles were steep and wind speeds were high. As a result, use of the HV channel may reduce the time required to delineate the ice edge in ScanSAR imagery. However, new ice could not be identified in the HV channel. If the ice edge were mapped from HV data alone, revisions would need to be made using the HH channel to refine the ice edge to include new ice. It is therefore recommended that both polarizations be used in tandem for ice edge mapping. For steeper incidence angles ($< 31^\circ$) and higher wind speeds (> 17 km/hr) it is expected that the ice-open water contrast in the HH channel would be further reduced, as observed in the March 5 ASAR image (Figure 4.1). Under these conditions it is anticipated that the improved visual contrast between FY ice and open water in the HV channel would be of greater benefit for ice edge mapping.

These results are in agreement with previous analyses of SIR-C data (Scheuchl et al., 2001) and Envisat/ASAR AP data (Scheuchl et al., 2004b; Arkett et al., 2007), which found that improvements in the separation of ice and open water provided by dual-pol data were greatest at steep incidence angles. This agreement indicates that for RADARSAT-2 ScanSAR data the reduced number of looks (relative to SIR-C data) and the reduced spatial resolution (relative to the Envisat/ASAR AP data) do not limit the improved visual contrast between ice and open water, although these factors likely reduce the precision of the ice edge delineation.

4.2.3 Separation of Ice and Open Water Within Mobile Pack Ice

While the delineation of the ice edge from HH data alone was acceptable for each dual-pol RADARSAT-2 image acquired during SGULF09, there were localized incidences within the mobile pack ice where the contrast between ice and open water was not ideal. Three examples are shown here to illustrate situations where the availability of the HV channel improved the visual separation of ice and open water.

In the March 5 (21:47) SCNA image the separation between ice and open water within the ice pack in the vicinity of the Iles de la Madeleine was not ideal in the HH channel, particularly within the FY ice to the south of the islands. The ice and snow cover are assumed to be frozen as air temperatures recorded at the Iles de la Madeleine in the 24 hours prior to image acquisition were $<-8^{\circ}\text{C}$. Winds throughout the day were from the west to northwest with an average speed of 23 km/hr. At 22:00 the air temperature was -8.5°C and winds were 39 km/hr from the northwest. The winds created a small area of open water to the east of the Iles de la Madeleine. This area of open water was bounded to the east by streaks of grease ice. Beyond the grease ice, FY pack ice was found. This progression of ice types was noted during helicopter overpasses and can be observed in video data (frames 38000 to 38500). To the south of the Iles de la Madeleine the ice pack was made up of predominantly thin FY ice. In the HH channel the contrast between the open water and the FY ice was not great, although with local image enhancements the ice edge could be identified. This same boundary was far more evident in the HV channel (Figure 4.8).

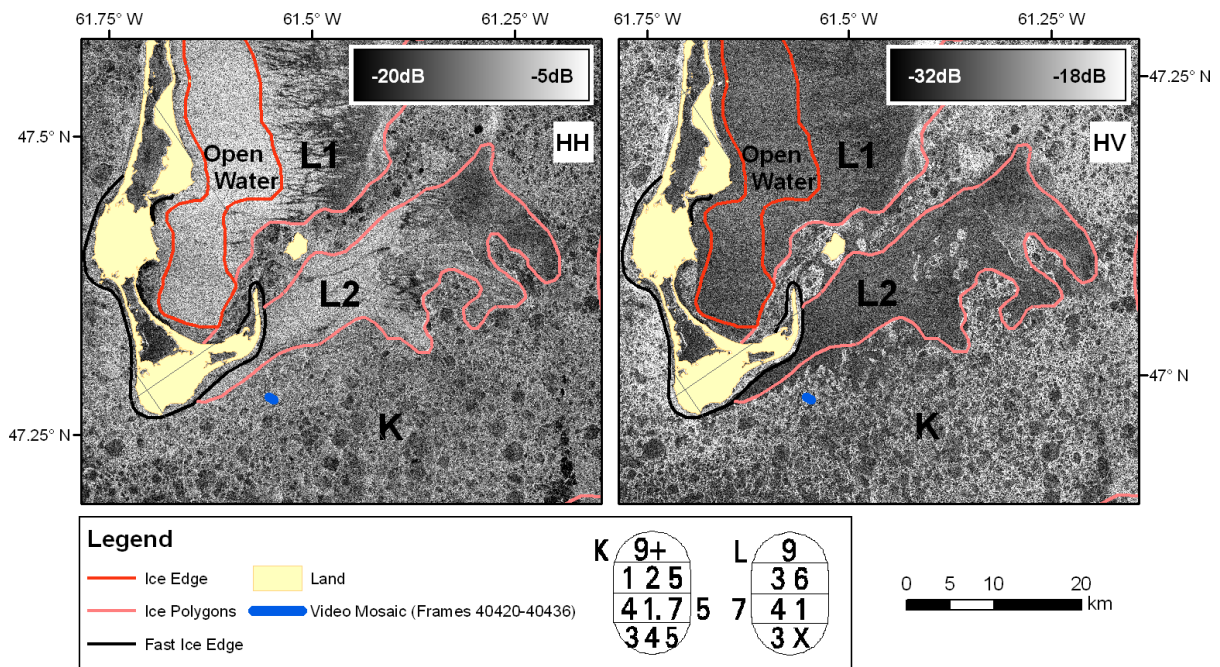


Figure 4.8: RADARSAT-2 SCNA imagery (March 5, 21:47) and image analysis chart vectors in the vicinity of the Iles de la Madeleine. Ice polygons L1 and L2 share the same egg code (L), the numerical suffixes were added to allow the polygons to be differentiated in the text. RADARSAT-2 data and products © MacDonald, Dettwiler and Associates Ltd 2009 – all rights reserved.

It is clear that the ice polygon boundaries in this area, which covers incidence angles of 23-28°, are more evident in the HV image, with the exception of the boundary between the new ice (polygon L1) and the open water to the east of the Iles de la Madeleine, where the grease ice is difficult to identify in the HV data. It is interesting to note that in this case the grease ice is not completely lost in the ocean clutter (HV backscatter in polygon L1 is lower than in the open water polygon); however, the HH channel is clearly still preferable for mapping the extent and concentration of new ice. In the HH image, the FY ice to the south of the Iles de la Madeleine (polygon K) appears to be of high concentration (and is mapped as 9+/10). In the HV image the concentration of the FY ice is difficult to determine because the backscatter from open water and smooth FY floes is similar. In contrast to the HH observations, analysis of video data collected at 20:17 (frames 40350 to 40700) revealed that there were considerable areas of open water between floes in this region. Visual analysis of MOD02HKM data (15:35) also suggested the presence of open water within the FY pack ice,

although confidence in these data are low due to the presence of thin clouds. A mosaic of video frames representative of the ice in this region clearly illustrates that open water is present within the mobile ice pack (Figure 4.9). The location of this video mosaic is shown on Figure 4.8.

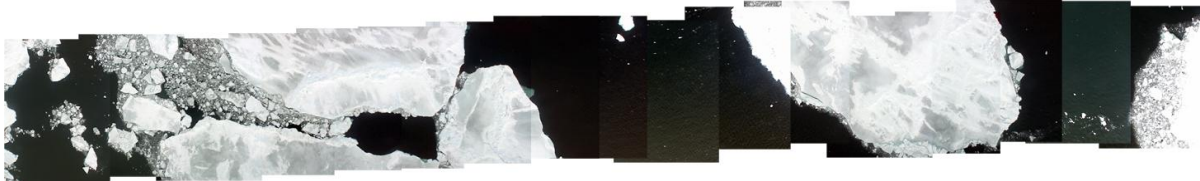


Figure 4.9: Mosaic of video frames 40420-40436 over FY ice and open water south of the Iles de la Madeleine, March 5 (20:17). The mosaic has a length of ~914 m and width of ~107 m.

Analyzed independently neither polarization provides ideal information for polygon K, as ice concentration is either overestimated (HH) or cannot be estimated with confidence (HV). However, when the polarizations are combined into a colour composite the interpretation of boundaries between ice polygons and the estimation of ice concentration within each polygon is significantly improved (Figure 4.10).

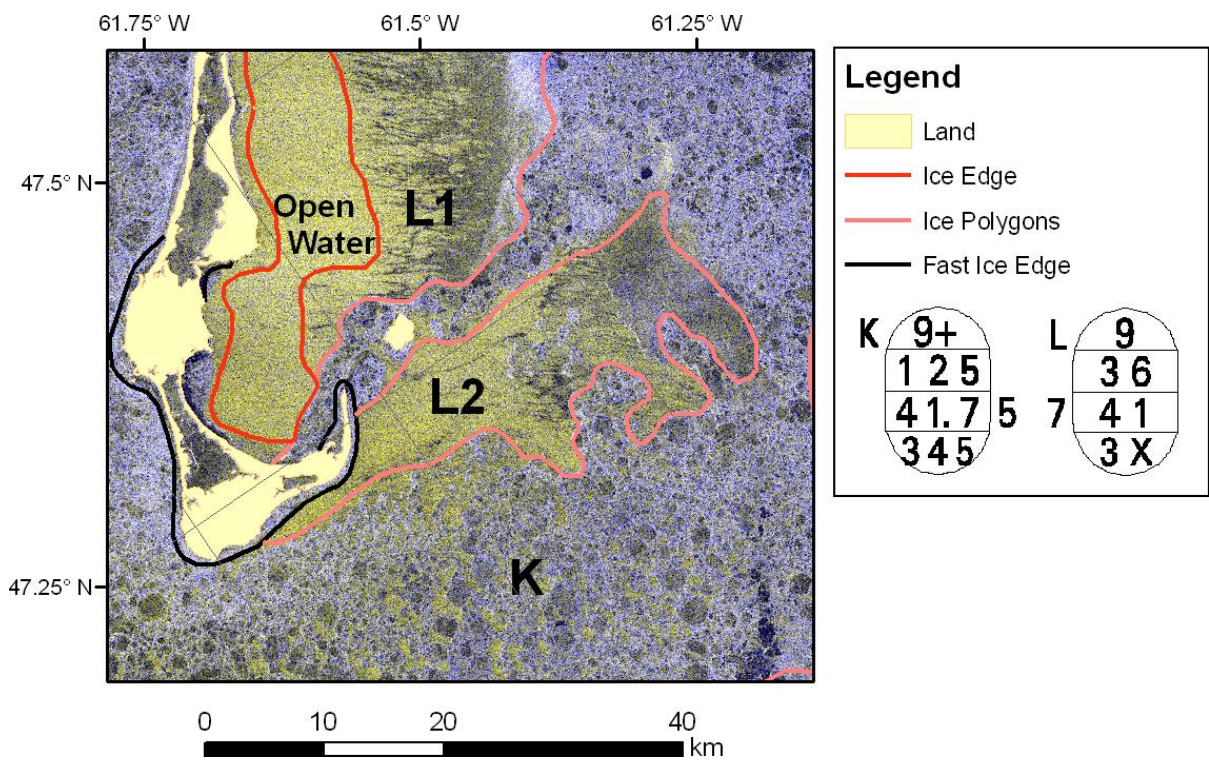


Figure 4.10: Dual-pol RADARSAT-2 SCNA imagery (March 5, 21:47) illustrating the improved visual separation of ice and open water within the FY ice pack when using a colour composite (R-HH; G-HH; B-HV). Vector data are from the CIS image analysis chart created from the SCNA data. RADARSAT-2 data and products © MacDonald, Dettwiler and Associates Ltd 2009 – all rights reserved.

Using a simple false colour composite (R-HH; G-HH; B-HV) open water appears yellow because open water backscatter is high in the HH channel (red and green) and low in the HV channel (blue). Ice appears primarily blue in colour, with new ice and smooth FY floes being dark. In agreement with the video and MODIS data, interpretation of the colour composite indicates that open water was present within the ice pack in polygon K, and that the 9+/10 concentration reported on the image analysis chart was overestimated. It is also worth noting that some small FY ice floes are visible within the new ice matrix in polygon L2. These floes are very difficult to identify in the HH image alone (due to the similar backscatter from FY ice and open water at this incidence angle and wind speed), but can be identified in the HV image and in the colour composite. This trace of FY ice was reported in the egg code.

In the March 1 (22:04) SCWA HH image there is confusion between ice and open water along the New Brunswick coast at the western end of Northumberland Strait. The ice and snow cover are assumed to be frozen as air temperatures recorded at Miscou Island were $< -10^{\circ}\text{C}$ for the entire day. Winds were near 20 km/hr throughout the day from northwest through northeast. At 22:00 the air temperature was -11.0°C and winds were 24 km/hr from the northeast. These weather conditions suggest that new ice formation was possible and that the ice pack likely drifted south and west on this day. Airborne ice observations indicate that a small strip of open water was present along the New Brunswick (NB) shore, and that the ice cover between NB and PEI increased in thickness from new ice in the west to FY ice in the east (Figure 4.11).

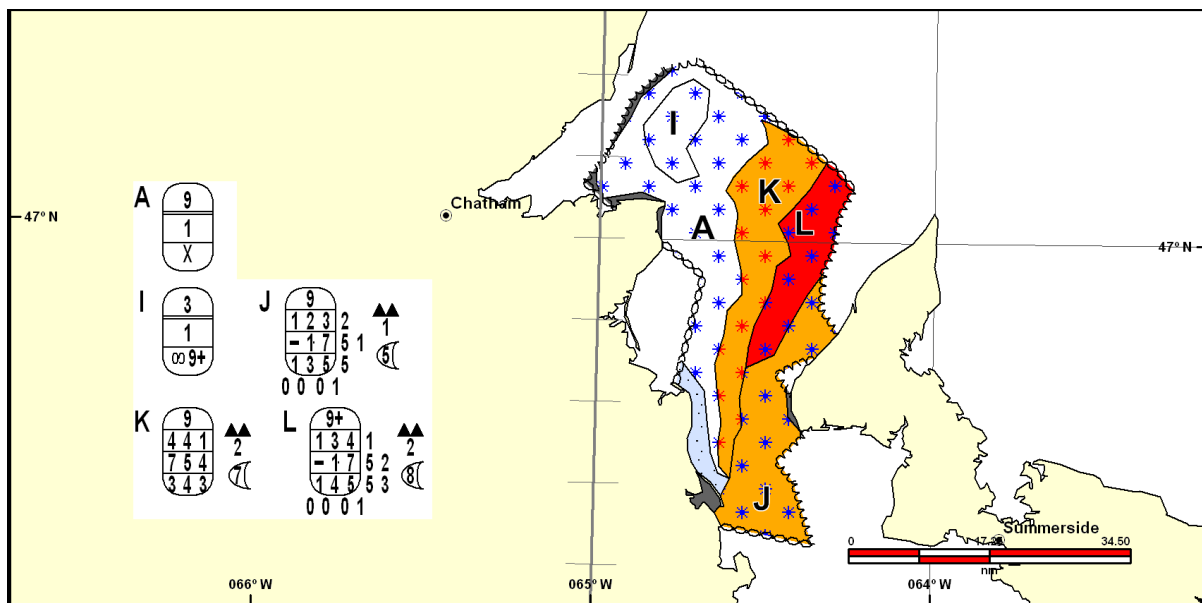


Figure 4.11: Subset of the March 1 observed ice chart (Chaleurs Bay, DASH-8 recon #00024, 13:25-21:50) illustrating the increase in ice thickness from west to east between NB and PEI.

In contrast with the observed ice chart, the image analysis chart did not report the presence of open water along the NB shore. Instead high concentrations (9+/10) of new ice and grey ice were reported (Figure 4.12).

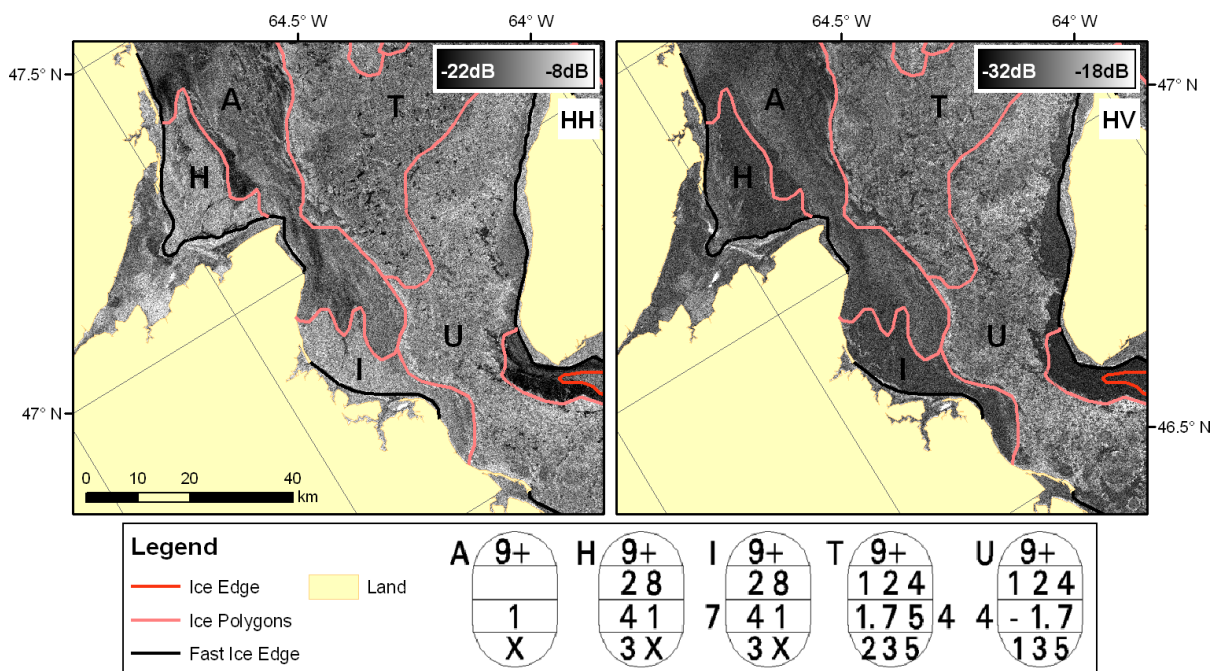


Figure 4.12: RADARSAT-2 SCWA imagery (March 1, 22:04) and image analysis chart vectors in western Northumberland Strait. RADARSAT-2 data and products © MacDonald, Dettwiler and Associates Ltd 2009 – all rights reserved.

The area reported as open water in the observed ice chart overlaps directly with the southern half of polygon I in the image analysis chart. The 9+/10 total ice concentration reported for polygon I of the image analysis chart could be explained by new ice growth or southwesterly ice drift between the time of the airborne observation and SAR acquisition, or due to misclassification of open water as new ice. The valid time for the observed chart is 13:25-21:50 so the time difference between the observation and SAR acquisition is unknown and could be almost 9 hours or as little as 15 minutes; however, the position of the boundary between new ice and the FY ice in the observed chart is in good agreement with the interpreted position in the image analysis chart. It is therefore assumed that there is a minimal time difference (or at least minimal ice drift) between the observation and SAR data acquisition. Thus, the presence of open water is likely along the NB shore.

In the image analysis chart polygons H and I suggest that there is near complete ice coverage (9+/10 concentration). Based on the HH image it is difficult to determine whether ice or open water is

present, due to the low contrast between ice and open water at this incidence angle (29-31°). The HV image is also of little use as new ice and open water cannot be reliably separated; however, when viewing the imagery as a colour composite, polygons H and I both have portions that appear yellow, suggesting the presence of open water in these regions (Figure 4.13).

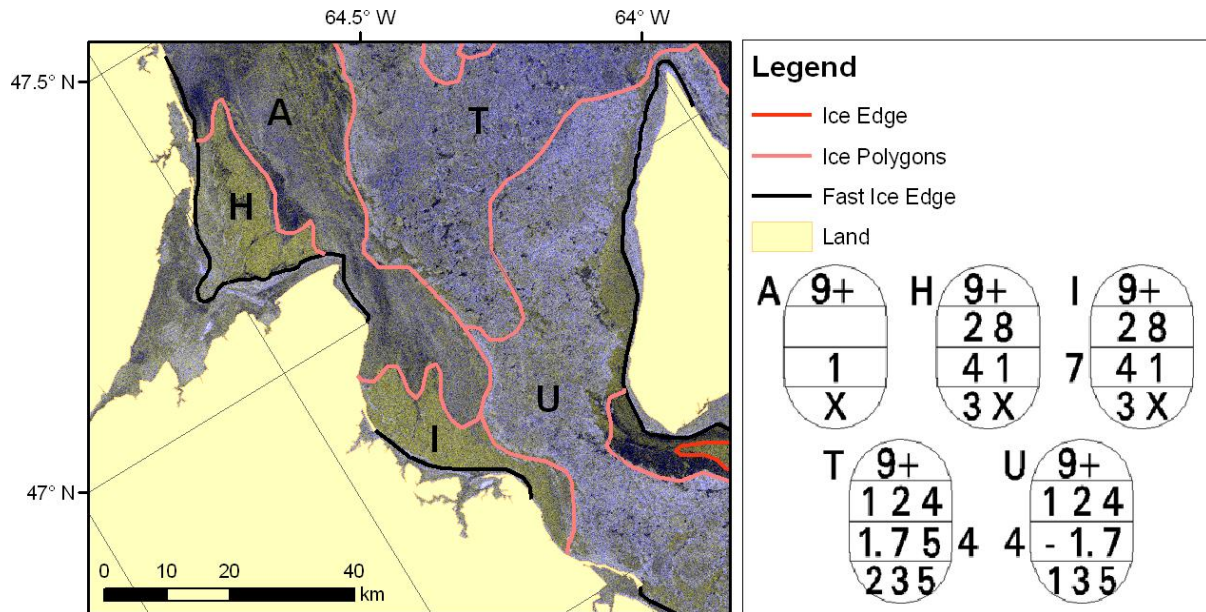


Figure 4.13: Dual-pol RADARSAT-2 SCWA (March 1, 22:04) imagery illustrating the improved separation of ice and open water when using a colour composite (R-HH; G-HH; B-HV). RADARSAT-2 data and products © MacDonald, Dettwiler and Associates Ltd 2009 – all rights reserved.

Polygon I is primarily yellow in colour suggesting that it is mostly open water, while the western half of polygon H appears to be covered with young ice. Had new ice been present in these polygons a much darker colour (such as that observed in polygon A) would be expected, as backscatter from new ice is generally very low in both HH and HV. Additionally, the HV backscatter signature of polygon A (also reported as new ice) is higher than that of polygons H and I, suggesting that the ocean cover of these regions are not the same. These results suggest that the image analysis chart is erroneous and that the presence of open water, as interpreted from the colour composite, in agreement with the airborne observations, is correct. Unfortunately no further validation datasets were available (no IcePic or video data were acquired in this area and MODIS data were obscured by clouds).

In the February 26 (21:52) SCWA image ice conditions along the Gaspé Peninsula in the vicinity of the Baie de Gaspé were difficult to interpret from the HH channel alone. The mean air temperature recorded at Gaspé on this day was -9.2°C ; however, air temperatures were $>0^{\circ}\text{C}$ between 18:00 and 22:00, reaching a maximum of 2.0°C at 19:00. Winds were weak (<10 km/hr) from the southwest for most of the day, except between 18:00 and 21:00 when winds averaged 19 km/hr. At 22:00 the air temperature was 0.1°C and winds were 6 km/hr from the southwest. No precipitation was recorded. Based on these weather conditions the ice and snow cover may have been melting at the time of the SAR acquisition, and the ice cover is expected to have drifted northeast away from the coast throughout the day. ISS shipboard observations acquired at 13:00 from the CCG icebreaker *Des Groseilliers* (call sign CGDX) reported that the Baie de Gaspé was full of new ice and nilas while young ice and thin FY ice were observed at the mouth of the bay (Figure 4.14).

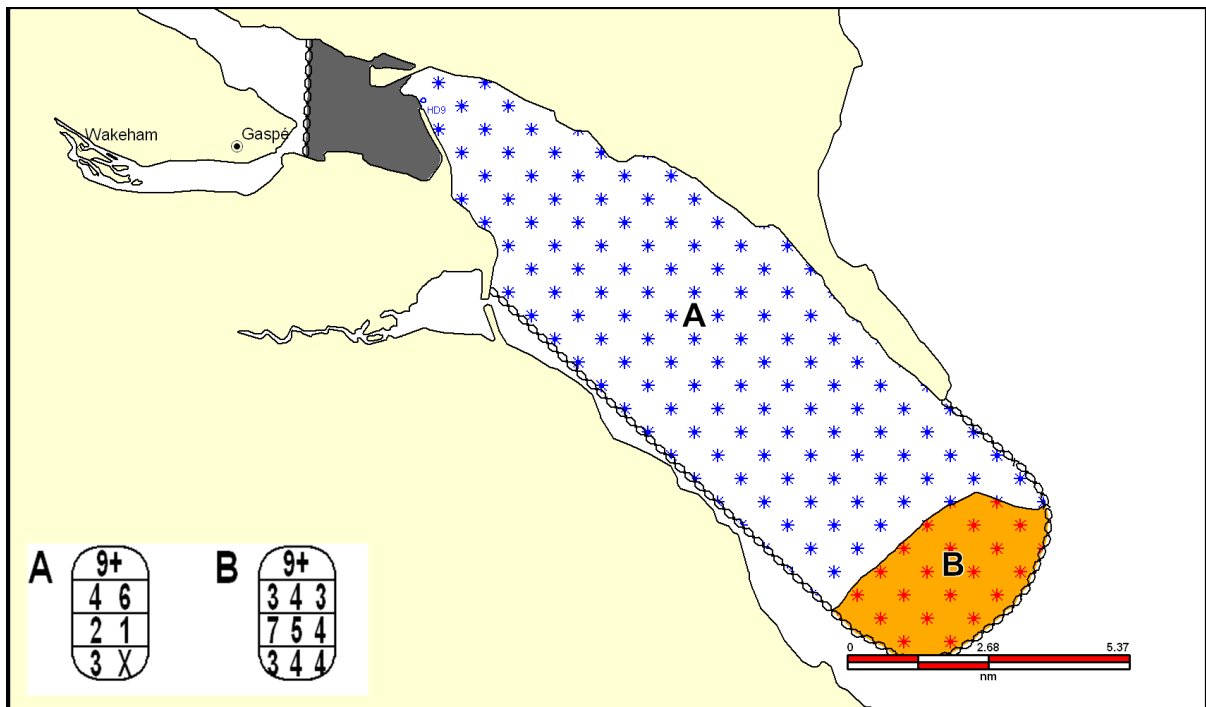


Figure 4.14: Subset of the February 26 observed ice chart (Baie de Gaspé, CGDX recon #00073, 12:30-13:35) illustrating the presence of new and young ice in Baie de Gaspé.

At the time of the shipboard observations temperatures were $<0^{\circ}\text{C}$ and winds were 4 km/hr from the southwest. In the nine hours between the shipboard observation and SAR data acquisition air temperatures rose and wind speeds increased. As a result, ice growth should not have occurred between these observations, and some of the new ice cover could have melted or could have drifted towards the north shore of Baie de Gaspé. Interpretation of the HH imagery suggests that new ice was present at high concentrations in the northern half of the bay (where backscatter is very low), while the concentration of new ice was reduced in the southern half of the bay as evidenced by small areas of high backscatter (open water). In the HV channel the new ice and open water within the Baie de Gaspé could not be separated (Figure 4.15).

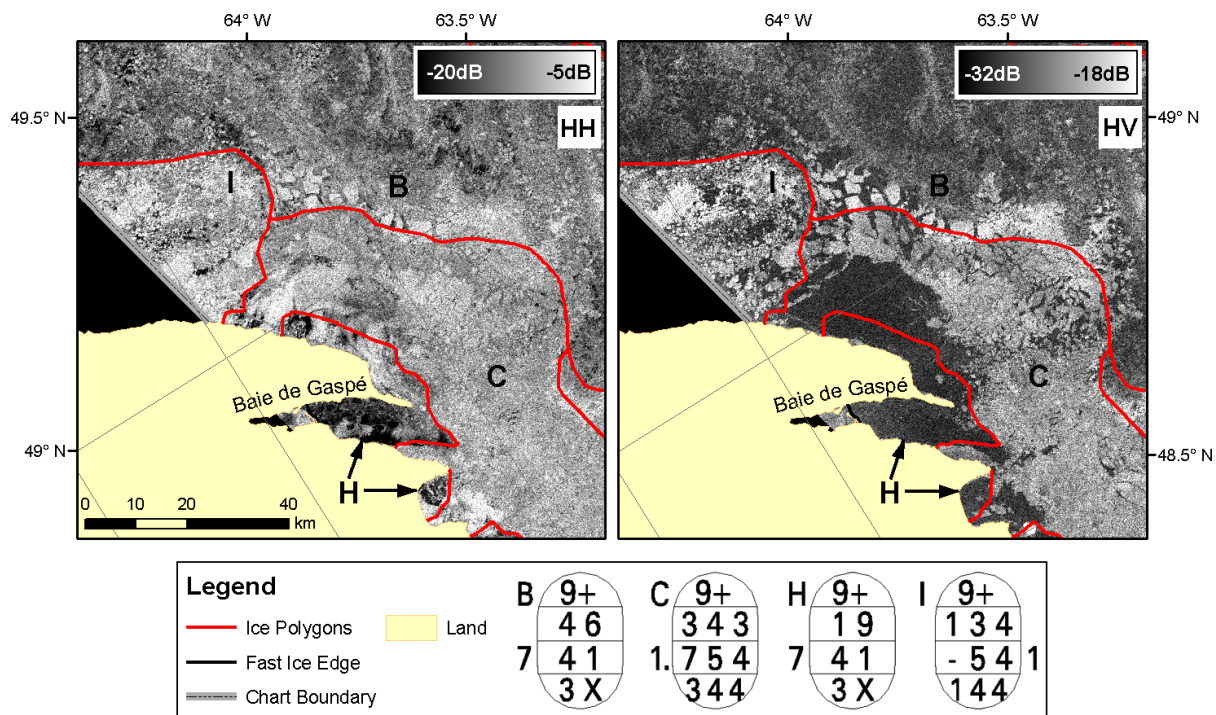


Figure 4.15: RADARSAT-2 SCWA data (February 26, 21:52) and image analysis chart vectors near Baie de Gaspé. RADARSAT-2 data and products © MacDonald, Dettwiler and Associates Ltd 2009 – all rights reserved.

The interpretation of the SAR data within Baie de Gaspé is in agreement with the shipboard observations and meteorological data; however, the ice conditions north of the Baie de Gaspé are far more difficult to interpret. The image analysis chart indicates that there is near complete ice cover

(9+/10 concentration) throughout this area, and visual analysis of the HH channel suggests that this may be the case; however, the portion of the SCWA image shown in Figure 4.15 covers incidence angles between 19° and 23°, so open water backscatter is expected to be high and may be similar to the backscatter from young and FY ice. Analysis of the HV channel indicates that there may be considerable areas of open water (or new ice), particularly in ice polygons C and H. By combining the two channels into a false colour composite the separation of open water from new ice and from young and FY ice is easily achieved (Figure 4.16).

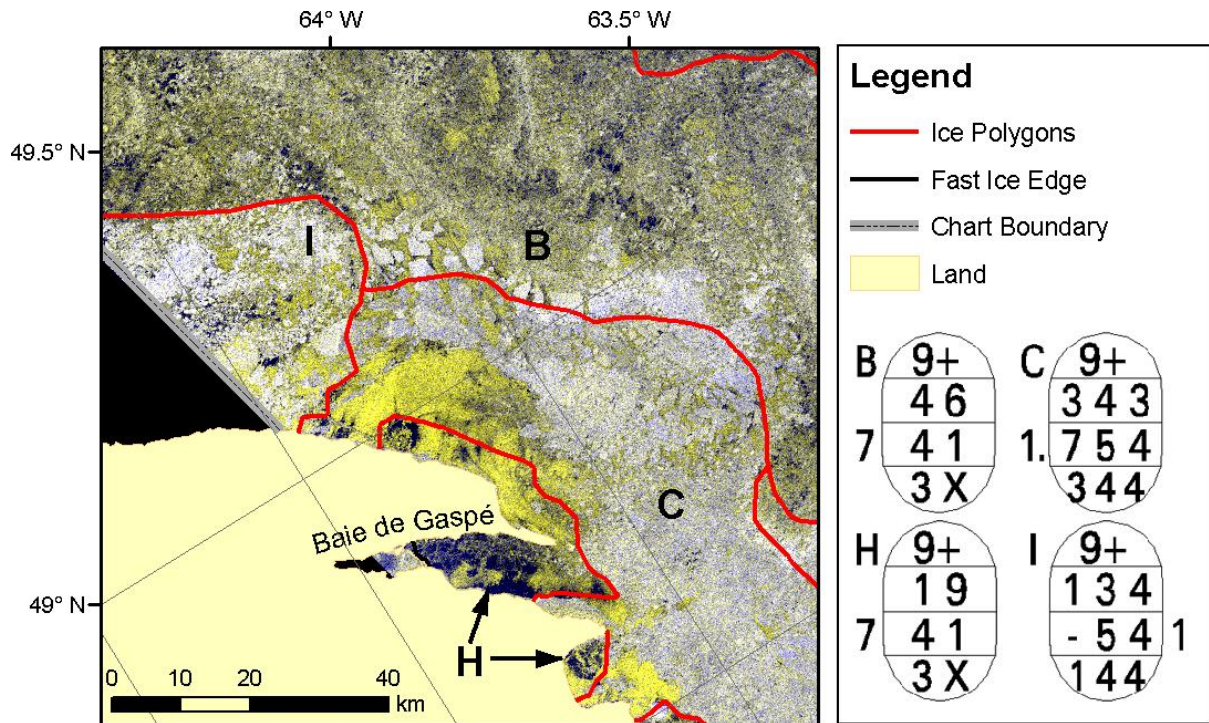


Figure 4.16: Dual-pol RADARSAT-2 SCWA imagery (February 26, 21:52) illustrating the improved separation of ice and open water when using a colour composite (R-HH; G-HH; B-HV). RADARSAT-2 data and products © MacDonald, Dettwiler and Associates Ltd 2009 – all rights reserved.

As observed in the previous examples, open water appears yellow, new ice appears dark blue and thicker ice types appear brighter shades of blue or white. For this image the dual-pol data suggest that the total concentration of polygons C and H are overestimated. Within the Baie de Gaspé the egg code for polygon H is appropriate; however, in the portion of polygon H to the north of Baie de

Gaspé and in the western portion of polygon C the ice concentration is less than what is reported in the egg codes. For these areas a separate ice polygon of moderate ice concentration would have been more appropriate.

These examples demonstrate that the discrimination of ice and open water can be improved through the use of dual-pol RADARSAT-2 data. For the scenes collected during SGULF09 the improved separation between ice and open water was most noticeable at incidence angles $<30^\circ$. This was observed at various wind speeds (6 to 39 km/hr). At these steep incidence angles the separability of young and FY ice from open water was poor in the HH channel, as backscatter was high from each of these surfaces. It is suggested that ice concentration can be overestimated if the HH channel alone is used to map ice conditions at these incidence angles. In the HV channel there was excellent separability of young and FY ice from open water at all incidence angles; however, new ice and open water could not reliably be distinguished. The HV backscatter (and hence SNR) from new ice and open water was low (<-24 dB) across the full ScanSAR swath. In a few cases there was a slight contrast between new ice and open water, with the HV backscatter from new ice being less than that of open water. This indicates a slight improvement over Envisat/ASAR, as previous analyses of AP data (e.g. Scheuchl et al., 2004b; Arkett et al. 2007) indicated that new ice and open water were never separable at the higher NESZ of Envisat/ASAR. Based on modelled and observed airborne SAR backscatter signatures reported by Nghiem and Bertoia (2001; Figure 2.4), a system with a lower NESZ than RADARSAT-2 may further increase the contrast between new ice and open water. Regardless, the HH channel in RADARSAT-2 ScanSAR data provides excellent contrast between new ice and open water. By analyzing the two polarizations in tandem as a false colour composite the limitations of each polarization can be overcome, allowing open water to be reliably separated from new ice, young ice and FY ice across the full width of the RADARSAT-2 ScanSAR swath.

From an operational perspective the improved ice-open water separation in the dual-pol data, relative to single co-pol data, is expected to improve the accuracy of ice edge and ice concentration estimates, although this will be limited to cases where a crossover between ice and open water signatures is observed in the HH data. Additionally, the improved separation between ice and open water should reduce the time required for an ice analyst to digitize the ice edge and to estimate ice concentrations of digitized ice polygons. Furthermore, these results suggest that the development of automated ice-open water segmentation algorithms that utilize dual-pol data may be possible. Results from Yu (2009) indicate that the use of a hierarchical segmentation algorithm shows considerable potential for separating ice and open water in dual-pol RADARSAT-2 ScanSAR data, although the process required some user input to define the segmentation hierarchy. With further research, it is plausible that fully automated ice-open water segmentation algorithms that utilize dual-pol RADARSAT-2 ScanSAR data could be developed. If successful, such algorithms could be implemented in an operational context, potentially increasing the speed with which image analysis charts are created.

From a climatology perspective the benefits of the improved ice-open water separation in the dual-pol data are likely to be reduced relative to the operation benefits. This is because the accuracy of image analysis charts derived from dual-pol data will only be improved, relative to single co-pol data, where there is a crossover of the signatures of ice and open water. During SGULF09 this was only observed over limited areas. Furthermore, ice climate data records are derived from regional ice charts, which incorporate numerous datasets in addition to image analysis charts, and the content of image analysis charts is generalized at the smaller map scale of regional ice charts (MSC, 2005); therefore, any improvements to ice edge and ice concentration estimates in image analysis charts are likely to have a lesser impact on the accuracy of regional ice charts and derived sea ice climate data records.

4.3 Ice Typing

Once ice and open water have been separated the next step during ice chart generation is to determine what stages of development (i.e. ice types) are present. As discussed previously, single co-pol C-band SAR data is generally considered acceptable for ice typing requirements under winter conditions. In contrast, the limited results from cross-pol data suggest that the backscatter signatures of new, young and smooth FY ice are less separable, relative to co-pol data (e.g. Arkett et al., 2006; Scheuchl et al., 2004a). Given that the image analysis charts created during SGULF09 were derived from the dual-pol RADARSAT-2 data, a comparison of the accuracy of ice type mapping from HH data alone versus HV data alone was not possible. Thus, the analysis presented here assesses the accuracy of ice typing from the dual-pol data, with the goal of determining whether or not the use of dual-pol (HH+HV) data introduced any bias into the resulting ice type classifications. In order to accomplish this evaluation ice thickness distributions from IcePic data were compared to ice type distributions from image analysis chart egg codes. Additionally, a qualitative visual comparison of the ice type information in each of the HH and HV channels was performed. This qualitative comparison was used to identify information in the HV channel that may be beneficial for ice type mapping.

Overall, ice thickness distributions derived from IcePic data were in good agreement with ice type distributions from coincident egg codes. Typically, the modal ice type (from the egg code) and the modal ice thickness (from the IcePic data) were in agreement; however, the tail of the IcePic ice thickness distributions were often skewed towards slightly thicker ice than the egg codes. Here two examples are provided to illustrate these findings, and explanations for these observations are given. The first example is taken from the image analysis chart for the February 26 (21:52) image, where a large ice polygon of primarily thin FY ice covered most of the Madeleine Shallows, including the area between the Iles de la Madeleine and PEI. In the afternoon a helicopter flight acquiring IcePic data was flown from the Iles de la Madeleine west to the seal herd, then south to Charlottetown. The

IcePic data were acquired between 16:14 and 18:02. These data represent the largest sample of IcePic data acquired over a single image analysis chart ice polygon during SGULF09. The location of the IcePic data are shown in Figure 4.17.

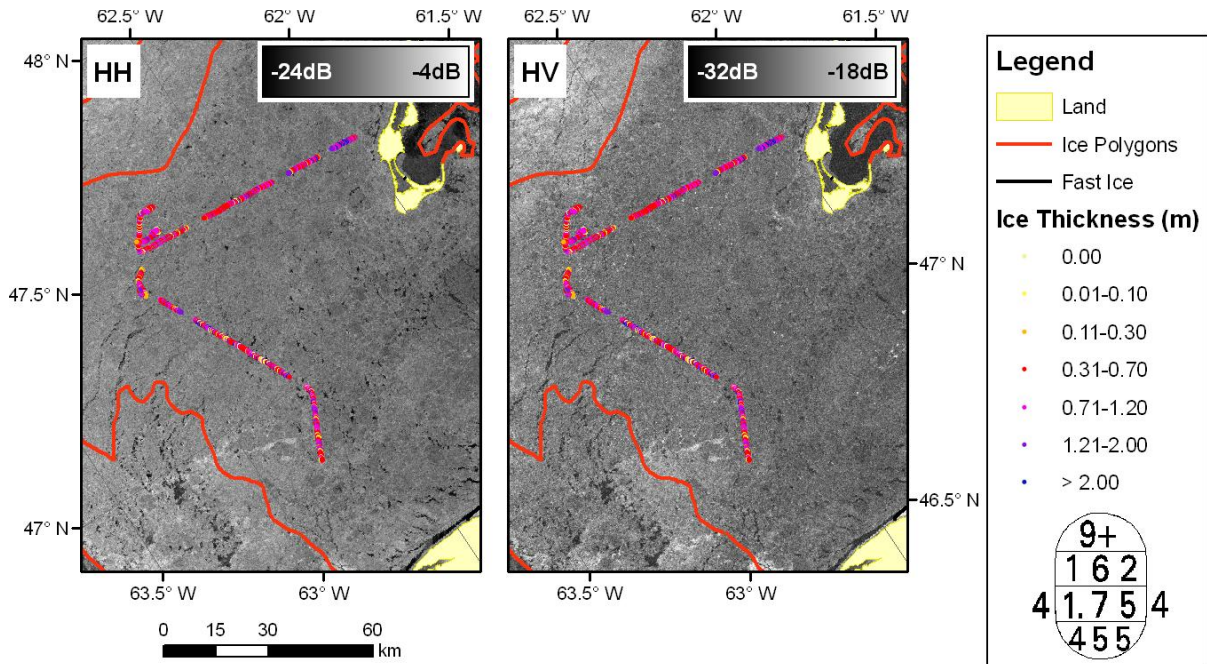


Figure 4.17: RADARSAT-2 SCWA data (21:52) and IcePic ice thickness data (16:14-18:02) acquired on February 26. RADARSAT-2 data and products © MacDonald, Dettwiler and Associates Ltd 2009 – all rights reserved.

Qualitatively the HH and HV images look similar; however, the definition of floe structure (which can be useful to help guide ice typing) appears somewhat reduced in the HV data. This observation contrasts with the expectations of Arkett et al. (2006) who suggested that, because floe edges are generally rough, the HV channel should provide improved floe structure information. The poor floe structure observed in the HV data in this scene may be a limitation of the spatial resolution of the ScanSAR data, which is likely too coarse to resolve floe edges. In addition to the reduced floe structure information, speckle appears slightly more prominent in the HV data. This can be attributed to the lower SNR of ice in the HV data, and by the fact that the dynamic range of the HV data is less than that of the HH data. The shorter dynamic range means that local image enhancements not only

affect the contrast of the ice features in the image but also detrimentally enhance the appearance of speckle (Figure 4.18).

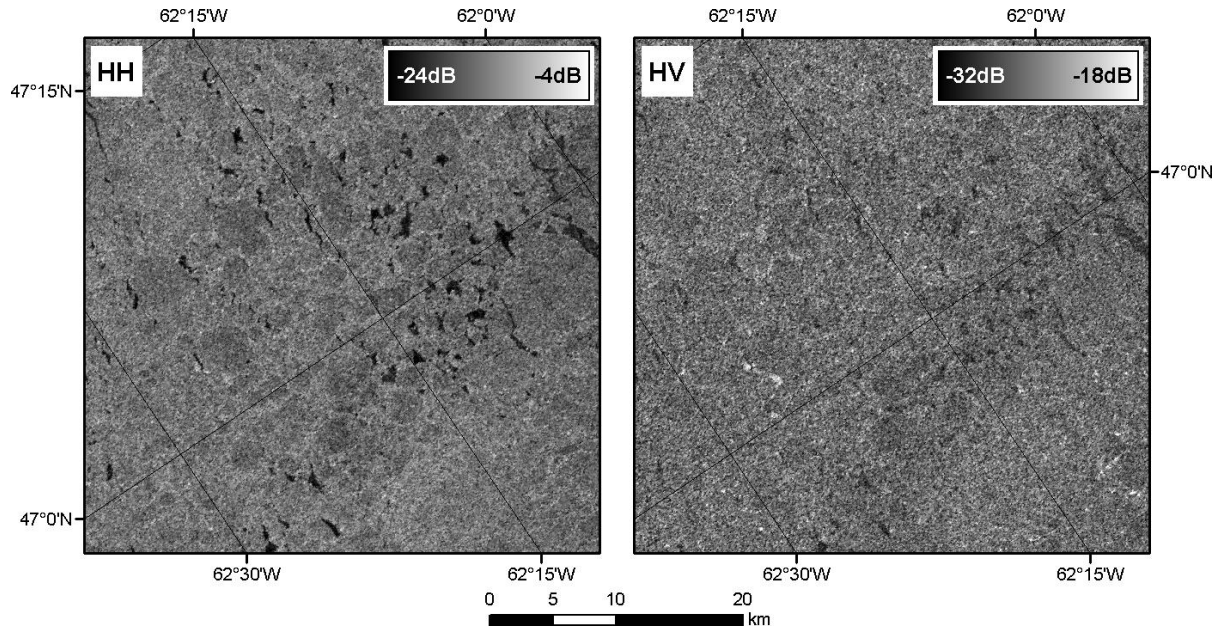


Figure 4.18: RADARSAT-2 SCWA data (February 26, 21:52) illustrating the reduced floe structure information and enhanced speckle in the HV channel. RADARSAT-2 data and products © MacDonald, Dettwiler and Associates Ltd 2009 – all rights reserved.

In this case the HV data on its own does not appear to provide any enhanced ice type information, relative to the HH data. Nevertheless, when the HH and HV data are combined as a colour composite the floe definition from the HH data remains prominent and the addition of the HV data does not appear to negatively impact the separation between individual ice floes or the separation between ice types (Figure 4.19).

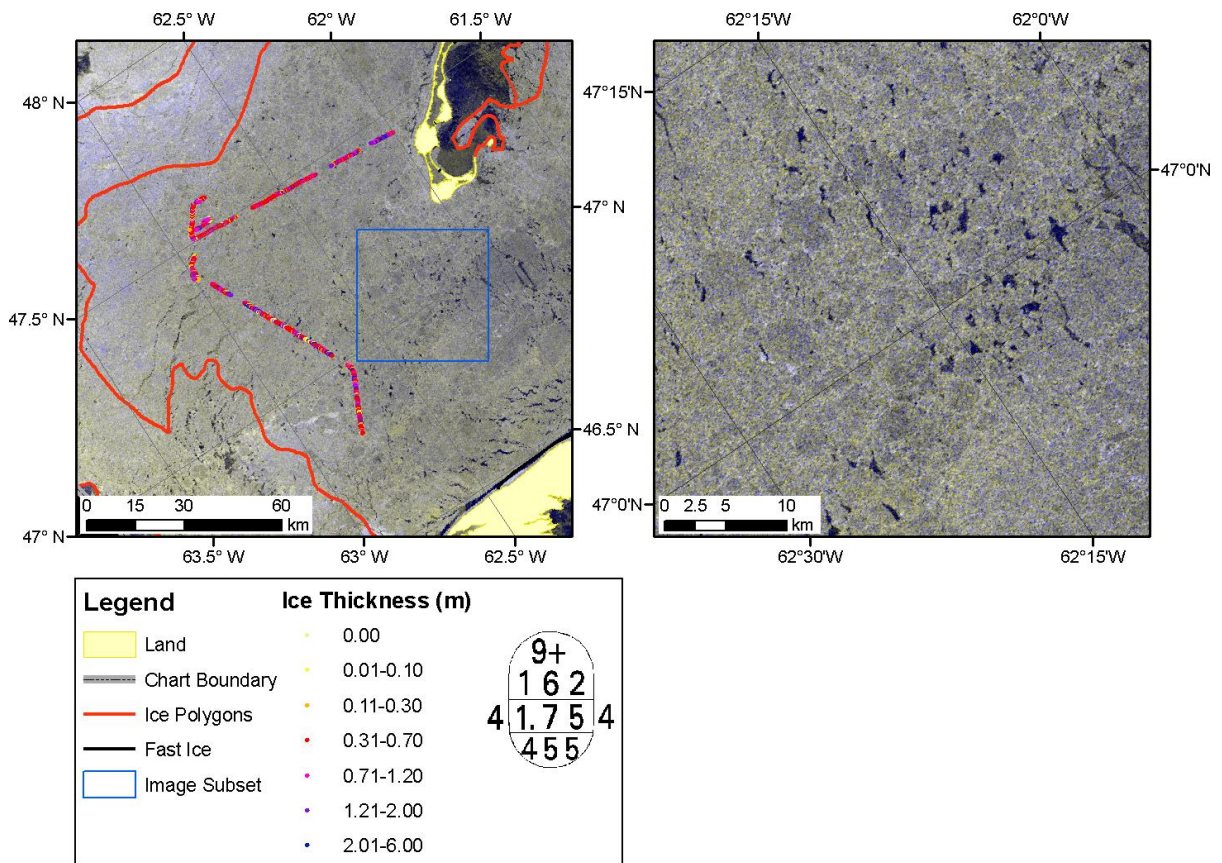


Figure 4.19: Dual-pol RADARSAT-2 SCWA imagery (February 26, 21:52) of ice in the Madeleine Shallows visualized using a colour composite (R-HH; G-HH; B-HV). RADARSAT-2 data and products © MacDonald, Dettwiler and Associates Ltd 2009 – all rights reserved.

In order to facilitate the comparison between the IcePic ice thickness data and the egg code ice type data, the IcePic data were binned according to the thickness ranges of the WMO ice types (Figure 4.20a). In order to illustrate a more detailed breakdown of the IcePic ice thickness data an equal interval histogram, with an interval of 10 cm, was also created (Figure 4.20b).

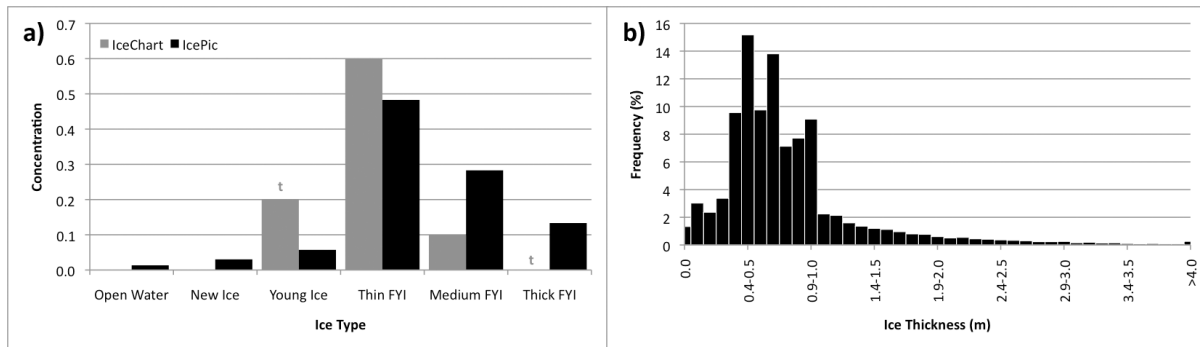


Figure 4.20: Ice type and thickness data for February 26 over the Madeleine Shallows. a) Ice type histograms derived from the image analysis chart egg code and transects of IcePic ice thickness data. The annotation 't' indicates that a trace of ice was reported in the egg code. b) Ice thickness histogram derived from IcePic data.

The ice type distribution defined in the egg code was in good agreement with the IcePic data. In particular the modal ice type for both datasets was thin FY ice. Assuming that the egg code ice types are correct, this agreement is expected, as the modal IcePic ice thickness should represent the modal level ice thickness (because level ice is more common than deformed ice in the mobile pack ice) (Peterson et al., 2008). While the datasets agreed on the modal ice type the IcePic data suggested that considerably more medium and thick FY ice was present than what was listed in the egg code. This discrepancy can be explained by the presence of deformed ice. Where deformed ice is present the IcePic is likely to measure a thickness that falls within a later stage of development (i.e. thicker ice type) than the ice is. For example, a ridge of thin FY ice that is 2 m thick would be binned into the thick FY ice category. The long tail of the IcePic histogram above 1.0 m ice thickness suggests that ridged ice is present along the flight path. If more than a trace of level thick FY ice were present a mode would be expected within this tail. Therefore, it is probable that the greater concentration of medium and thick FY ice reported in the IcePic data is due to the presence of deformed ice. Finally, there is some disagreement between the egg code and IcePic data on the concentration of young ice. This disagreement may result from the fact that IcePic data were collected over a small portion of the ice polygon (i.e. the ice measured by the IcePic along the flight path is not necessarily representative of all of the ice throughout the ice polygon). While the backscatter in the region of the flight path is

representative of the vast majority of this ice polygon, some areas of lower backscatter are observed within the ice polygon but are not observed along the flight path. A large area of this lower backscatter ice is located near 47°N, 62°W (Figure 4.19). This ice is likely young ice as less backscatter is expected from young ice due to its higher salinity (and higher dielectric loss factor), relative to FY ice. Given that the IcePic data provide only a profile within a much larger ice polygon, results must be used with caution. Nevertheless, it appears that the ice type distribution interpreted from the dual-pol RADARSAT-2 ScanSAR data are accurate.

The second example is taken from the image analysis chart for the March 5 (10:27) RADARSAT-2 image, over a region of new, young and FY ice to the east of PEI. In the morning a helicopter flight was flown through eastern Northumberland Strait and a profile of IcePic data was acquired in this region. The IcePic data were collected between 14:42 and 14:47 and the location of these data is shown in Figure 4.21.

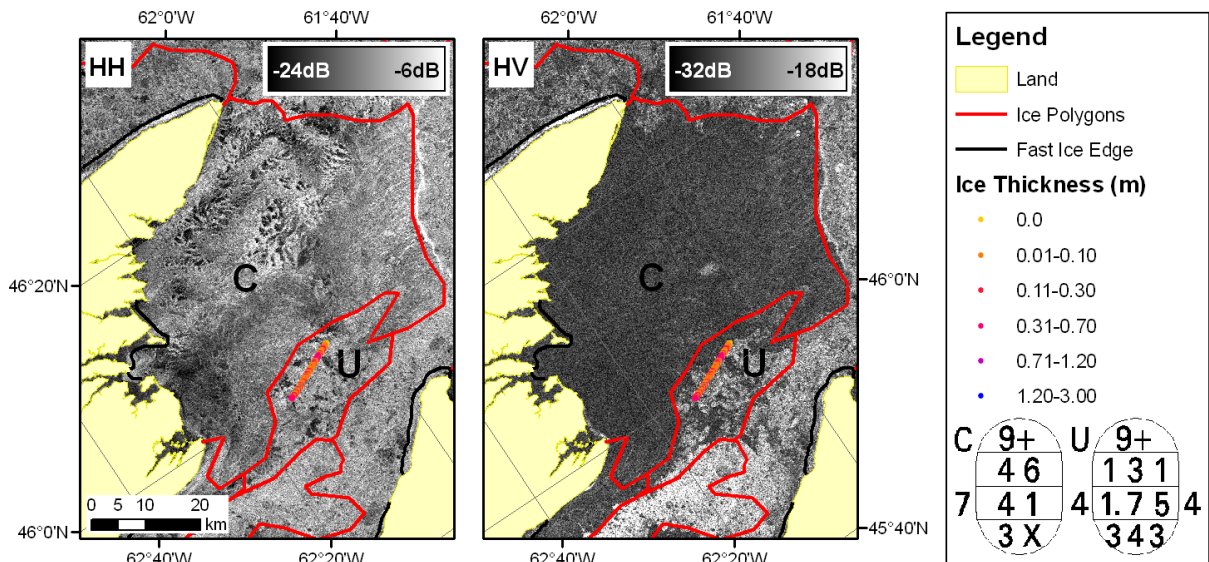


Figure 4.21: RADARSAT-2 SCWA imagery (10:27) and IcePic ice thickness data (14:42-14:47) acquired on March 5. RADARSAT-2 data and products © MacDonald, Dettwiler and Associates Ltd 2009 – all rights reserved.

In this case the HH and HV images are drastically different due to the presence of new ice. It is clear that in the HV image the new and grey ice in polygon C are not separable from open water.

Thus, the HV data alone are not suitable for ice typing when new ice is present. On the other hand, the shape of FY ice floes within polygon U are better defined in the HV data, due to the increased contrast between the FY ice and surrounding grey ice and open water. As a result, when the data are combined into a colour composite, open water and new ice are separable and the FY ice is also more separable (Figure 4.22).

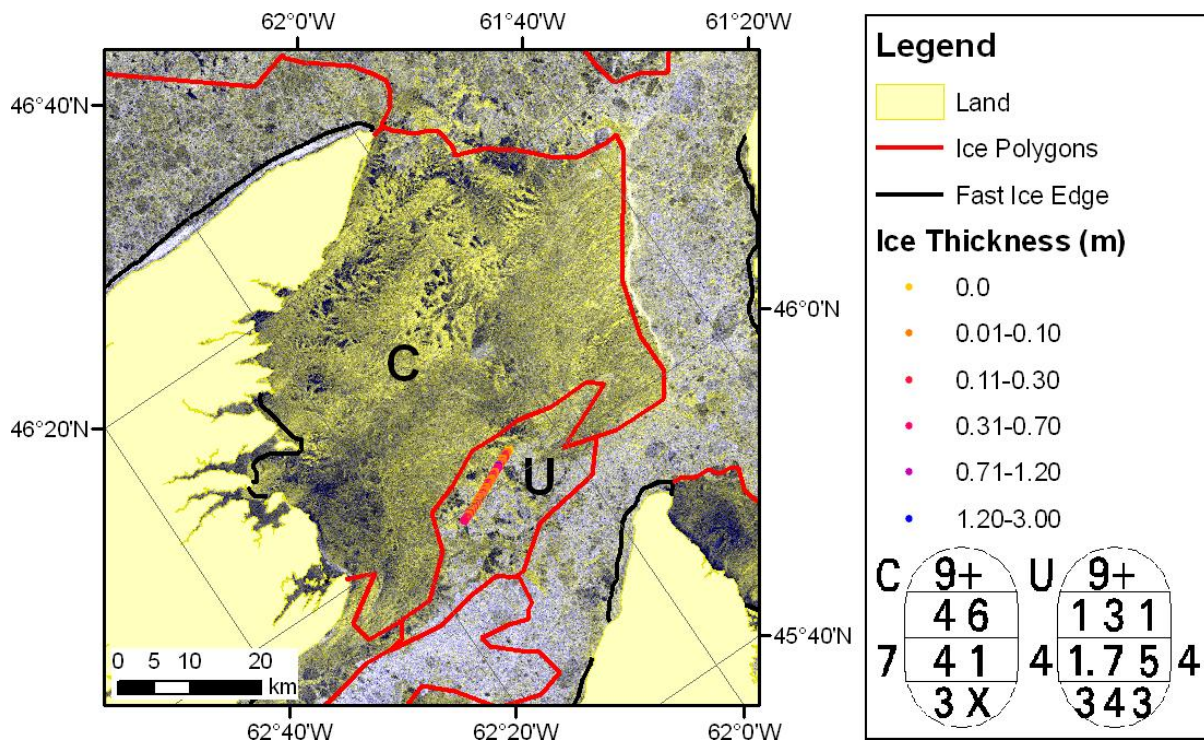


Figure 4.22: False colour composite (R-HH; G-HH; B-HV) of dual-pol RADARSAT-2 SCWA data (March 5, 10:27). RADARSAT-2 data and products © MacDonald, Dettwiler and Associates Ltd 2009 – all rights reserved.

Given the time difference between the SAR and IcePic acquisitions and the proximity of the IcePic profile to the boundary of ice polygon U, ice drift needed to be considered. Winds recorded at East Point, between 10:00 and 15:00 on March 5, were strong (mean of 29 km/hr) from the west. In the Madeleine Shallows the ice drift over this time period, as measured by the ice beacons, was 5 km to the east. Given the thinner ice conditions in Northumberland Strait it is plausible that the distance of ice drift over this time period would be greater than that measured at the beacons. This would mean

that the IcePic data might have been acquired over ice polygon C. This is supported by the IcePic data, of which over 85% of the ice thickness measurements are less than 20 cm. Additionally, in the evening RADARSAT-2 data (21:47) the boundary between the new and FY ice is ~10 km east of the IcePic profile. Thus, the IcePic data are compared to the egg code for ice polygon C instead of polygon U. In this case there was excellent agreement between the IcePic ice thickness data and the egg code ice type distribution (Figure 4.23).

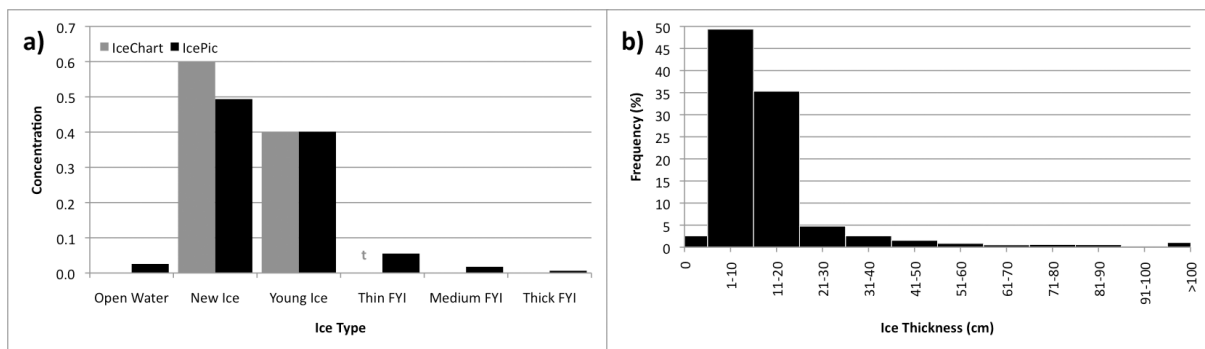


Figure 4.23: Ice type and thickness data for March 5, east of PEI. a) Ice type histograms derived from the image analysis chart egg code and a transect of IcePic ice thickness data. The annotation 't' indicates that a trace of ice was reported in the egg code. b) Ice thickness histogram derived from IcePic data.

For both the egg code and the IcePic data the modal ice type was new ice. There was also excellent agreement on the concentration of young ice. Furthermore, the IcePic data suggested that the young ice was primarily 11-20 cm thick, in agreement with the egg code, which indicates only the presence of grey ice (10-15 cm), not grey-white ice (15-30 cm). The IcePic data also indicate that a trace of thin FY ice was present and a few ridges were likely present as a very small concentration of ice thicknesses >70 cm were recorded by the IcePic.

Overall, these results suggest that the ice types reported in the egg codes derived from the dual-pol RADARSAT-2 ScanSAR data are acceptably accurate as discrepancies between partial concentrations reported in the image analysis chart egg codes and the IcePic data were usually <1/10 (the CIS strategic requirement for the accuracy of partial concentration estimates); therefore, the

addition of the HV channel does not appear to bias ice type results. Good agreement was found between the modal ice type for egg code and IcePic data; however, the IcePic data suggest the presence of more thick ice than the egg codes. This bias in the IcePic data can be attributed to the presence of deformed ice.

From visual analysis, the HV data alone does not provide enough information for accurate ice typing (due to the inability to identify new ice). Furthermore, in contrast with expectations of Arkett et al. (2006) the HV data did not provide improved information on ice floe shape and structure. This is likely due to the coarse resolution of the ScanSAR data. The observed reduction of ice type information of the HV channel, relative to the HH channel, is in agreement with previous analyses of multi-polarization C-band SAR datasets that have reported a reduced contrast between new, young and FY ice types in the HV channel. This has been observed for various SAR system parameters, including higher spatial resolutions (e.g. Envisat/ASAR) and lower NESZs (e.g. EMISAR) than RADARSAT-2 (Dierking et al., 2004; Scheuchl et al., 2004a; Arkett et al., 2007). While the HV data on their own are not suitable for ice typing, when combined with the HH data as a colour composite the ice type information content of the HH data is preserved. In cases where open water is present (and an ice-open water backscatter signature crossover exists) the addition of the HV channel can improve the definition of FY ice floes.

From an operational perspective these result suggest that the accuracy of ice typing in image analysis charts created from dual-pol RADARSAT-2 ScanSAR data will likely be comparable to the accuracy achieved previously from single co-pol data (for ice regimes limited to new, young and FY ice types). Therefore, no significant improvements to the accuracy of ice types reported in image analysis charts and derived climate data records are expected.

4.4 Level and Deformed Ice Separation

As discussed previously, the presence of deformed ice, which is of importance for tactical and climatological considerations, cannot be reliably derived from single co-pol C-band ScanSAR data; therefore, ice roughness information is currently not included in image analysis charts produced at the CIS (Arkett et al., 2007). However, MANICE (MSC, 2005) defines a relative roughness symbol for use on image analysis charts. This symbol is annotated to denote light, medium, or heavy roughness based on the concentration of deformed ice within the given ice polygon (Figure 4.24).

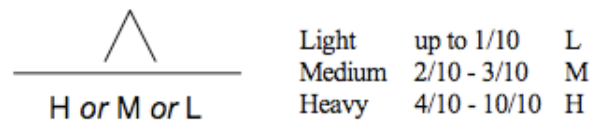


Figure 4.24: The relative roughness symbol provided in MANICE for use on image analysis charts (adapted from MSC, 2005).

This roughness statistic is only intended to be used when coincident visual reports are available to support the backscatter signature analysis (MSC, 2005). In addition to the relative roughness symbol, the use of discretionary boundaries is also permitted on image analysis charts. Discretionary boundaries are defined as “lines [that] are drawn for any changes within the egg code which could impact on tactical ice operations. For example an area of heavily ridged ice may be separated from level ice” (MSC, 2005). While these procedures for reporting deformed ice on image analysis charts are defined, to date they have not been implemented at the CIS.

In this section the ability to resolve deformed ice features in dual-pol RADARSAT-2 ScanSAR data is evaluated in order to determine whether or not the dual-pol data provide sufficient information to begin implementing the relative roughness symbol and discretionary boundaries on image analysis charts. This evaluation is carried out in two ways. First, bright features, which may be deformed ice, are identified in the RADARSAT-2 imagery, and field data are used to identify the ice properties that cause the bright radar returns. Second, the backscatter from regions identified as ridged ice in

observed ice charts is evaluated to determine whether or not the concentration of ridged ice within an ice polygon corresponds to the HH or HV backscatter amplitude.

4.4.1 Bright Ice Features Observed in the RADARSAT-2 Imagery

During SGULF09 the CIS identified two very bright (high backscatter) features that they could not attribute to any specific ice conditions with confidence, although they suspected that the strong backscatter from these features might be caused by deformed ice conditions. Following the RADARSAT-2 acquisitions in which these features were observed, efforts were made to collect field measurements over these targets. The first of these targets was a large region just offshore of PEI, north of Tracadie Bay. This feature was observed in the all of the SGULF09 SAR images that covered this area (Figure 4.25).

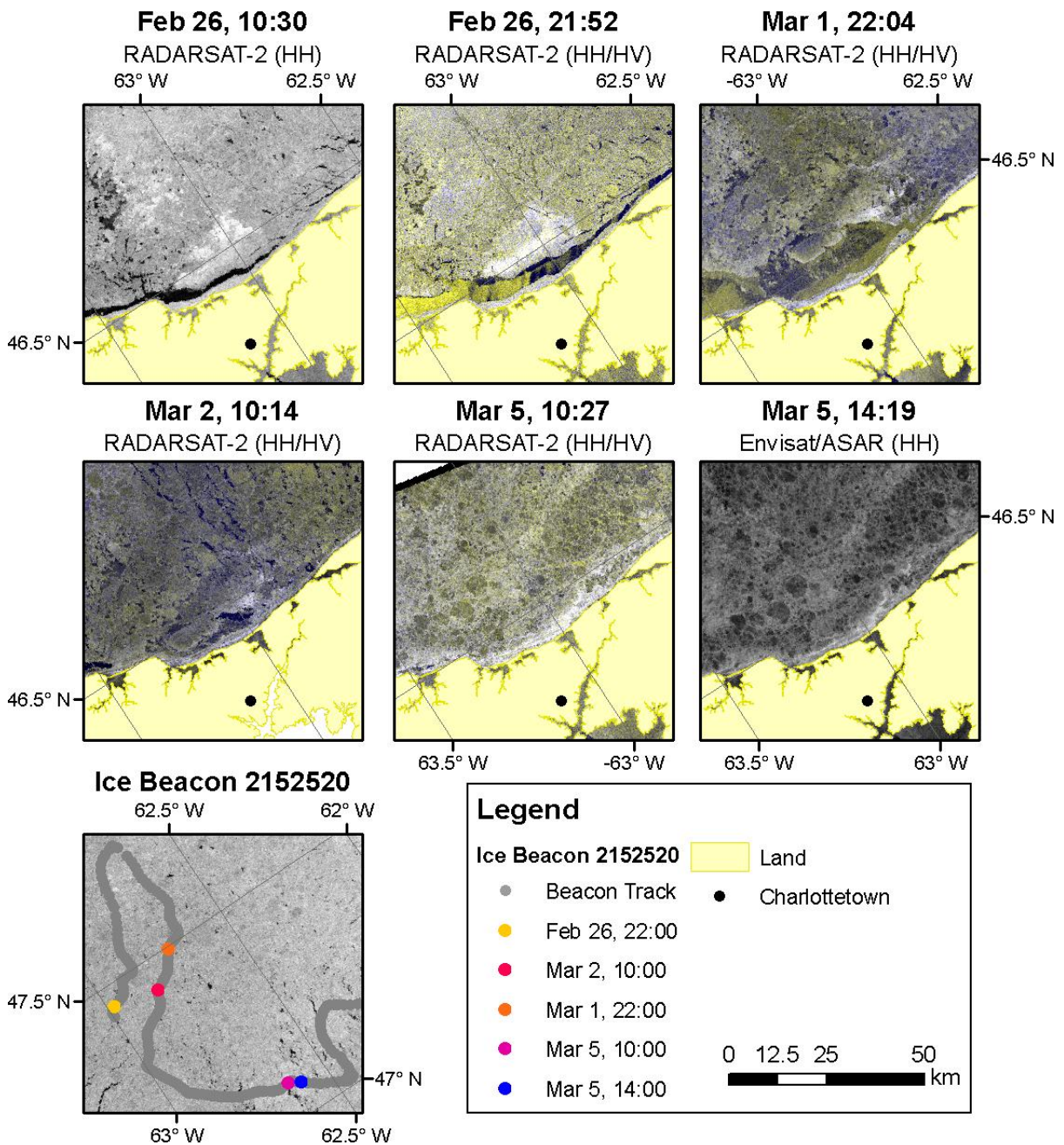


Figure 4.25: RADARSAT-2 and Envisat/ASAR imagery of a high backscatter feature north of Tracadie Bay, PEI. Data from ice beacon 2152520 are provided to illustrate ice drift between the acquisition times of each SAR image. The dual-pol RADARSAT-2 data are visualized as a colour composite (R-HH; G-HH; B-HV). RADARSAT-2 data and products © MacDonald, Dettwiler and Associates Ltd 2009 – all rights reserved. Envisat data © ESA 2009.

Throughout SGULF09 the HH and HV backscatter from this feature was high. As a result the feature appears white in both the single-pol (HH) images and in the colour composites of the dual-pol

(HH/HV) images. When this feature was first observed on February 26 it was roughly triangular in shape; however, this shape was not retained due to the pattern of ice drift in this region. Between February 26 and March 5 the mobile pack ice drifted northeast, southwest, then southeast, as evidenced by the ice beacon data (Figure 4.25). This pattern of ice drift, recorded by ice beacons located ~125 km north of Tracadie Bay, is in reasonable agreement with the ice drift near the PEI coast as visually interpreted from the SAR data; however, the coastline of PEI prevented the ice from drifting as far south as observed at the ice beacons. Instead of drifting southeast between March 3 and March 6, the pack ice in this region was forced eastwards along the fast ice edge. By March 5 the bright ice feature had been compressed and sheared into an elongated linear feature parallel to the fast ice edge.

Field data were successfully acquired over this bright feature on February 26 and March 5. On February 26 IcePic data were acquired over this region in the morning and video data were collected in the afternoon and evening (Figure 4.26).

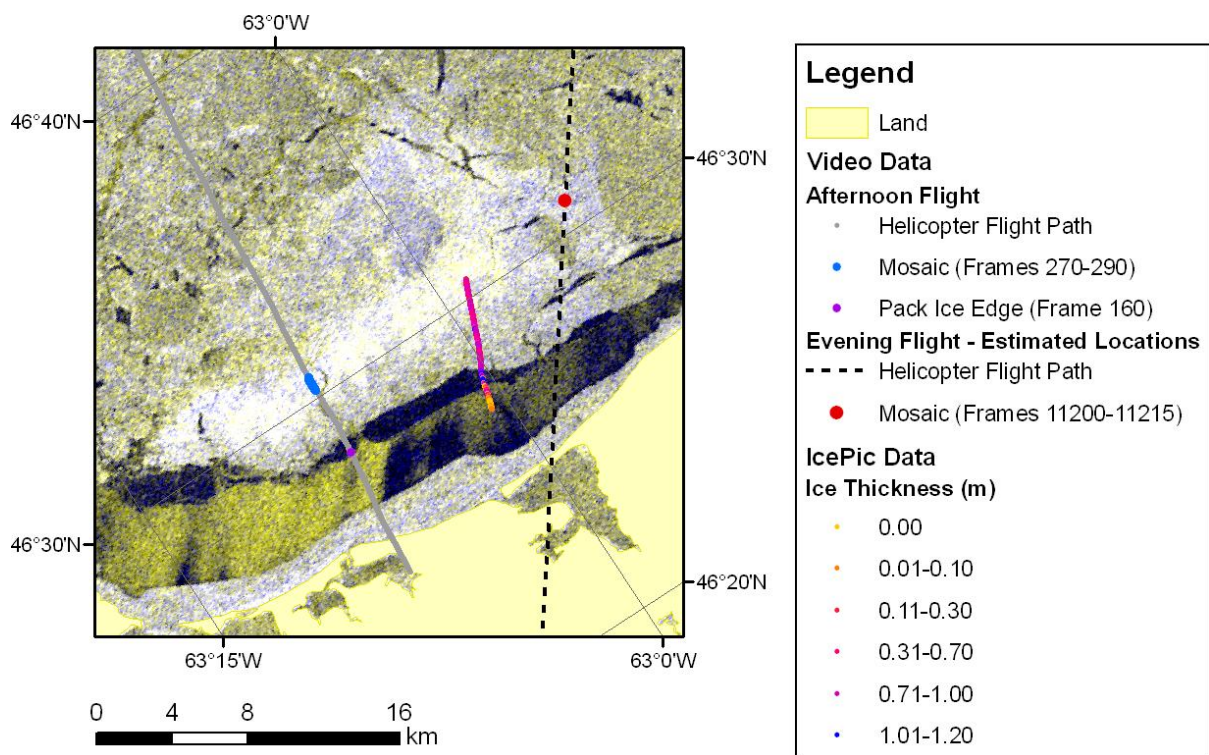


Figure 4.26: IcePic ice thickness data and video flight paths over the bright ice feature observed in the February 26 (21:52) dual-pol RADARSAT-2 data. The image is visualized as a colour composite (R-HH; G-HH; B-HV). RADARSAT-2 data and products © MacDonald, Dettwiler and Associates Ltd 2009 – all rights reserved.

During the morning IcePic flight regions of pancake-like ice, composed of ice cakes with levees, were noted in the field log (DFO, 2009). These ice cakes are thicker (>10 cm) than true pancake ice and the levees are not formed by frazil accumulation, rather the levees are blocky in structure. This pancake-like ice is thin enough (likely <30 cm) for some rafting to occur; however, the edges of the ice cakes are deformed during the rafting process creating very short ridge-like levees (Figure 4.27).



Figure 4.27: Photo of the pancake-like ice observed north of Tracadie Bay (February 26). The camera altitude was ~5 m.

In the IcePic data acquired over this region the mean ice thickness was ~70 cm; however, the ice is clearly not FY ice due to the absence of thick ridges; the ice is likely rafted young ice. Significant ridging (ice thicknesses >2 m) was only observed at the edge of the mobile ice pack (Figure 4.28).

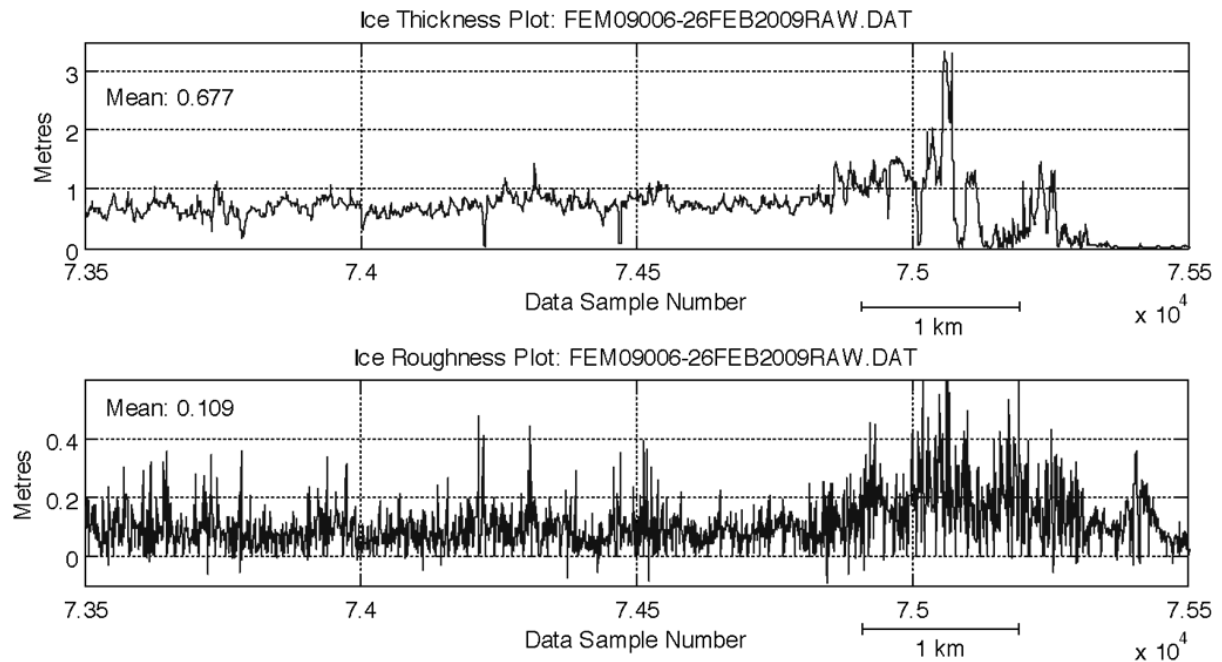


Figure 4.28: Ice thickness and roughness profiles measured over the bright ice feature north of Tracadie Bay, PEI (February 26, 18:16). Beyond sample 75000 ridged ice is present. The profile terminates over open water. The location of this IcePic profile is shown in Figure 4.26.

The strong co- and cross-pol backscatter in this region can be attributed to the surface roughness of the pancake-like ice. The mean surface roughness of this ice (~10 cm) is close to the radar wavelength (5.6 cm); therefore, diffuse surface scatter is expected to be the dominant scattering mechanism. This would explain the strong co-pol backscatter (~ -5 dB), while the strong cross-pol returns (~ -19 dB) indicate that multiple-surface scatter is also likely occurring. Although the surface roughness of these deformed young ice floes is sufficient to generate strong co- and cross-pol backscatter, these floes do not pose a significant risk to navigation.

For the outbound afternoon flight the helicopter was tasked for a reconnaissance mission and the flying altitude was increased to ~430 m. At this altitude the spatial resolution of the video data is greatly reduced (the pixel spacing is ~0.72 m by 0.72 m), while the width of the video frames is increased to ~460 m. In the video data acquired at 19:33 a region of deformed ice was identified. This deformed ice was well aligned with the bright feature in the RADARSAT-2 (21:52) image. The ice

drift between the acquisition of the video and RADARSAT-2 datasets, which was determined by comparing the position of the mobile pack ice edge in each dataset, was less than 1 km. In the video data many of the floes in this region are too small to be resolved, although rafting is observed between larger floes. This region is believed to contain pancake-like ice similar to that identified in the morning's low-altitude flights; however, at this altitude the short blocky edges of the pancake-like ice cannot be resolved (Figure 4.29).

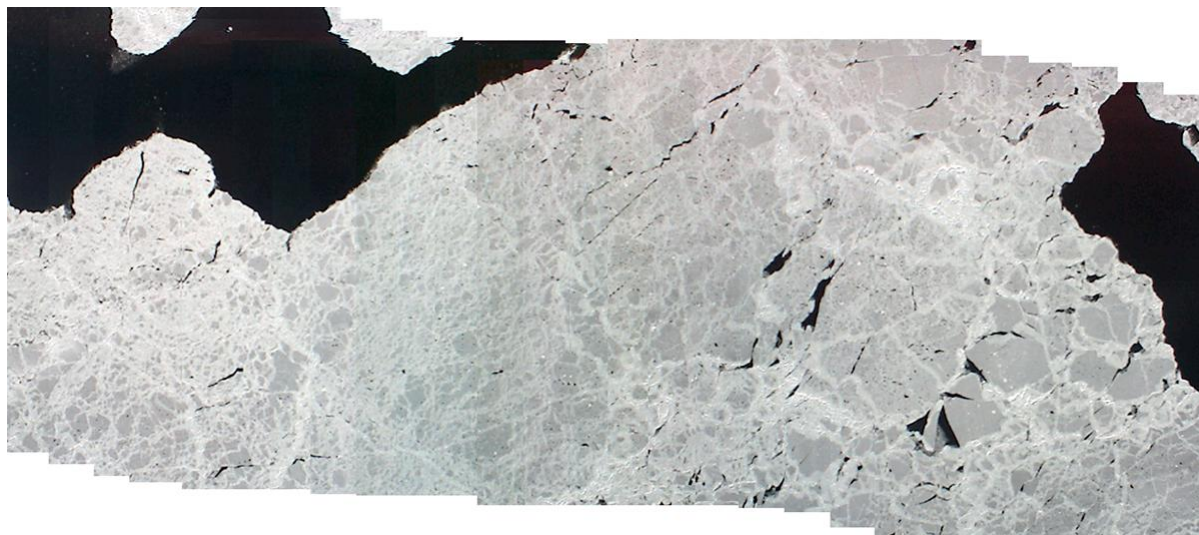


Figure 4.29: Mosaic of video frames 270-290 over deformed ice north of Tracadie Bay, PEI (February 26, 19:33). The mosaic has a length of ~1242 m and width of ~460 m.

For the inbound evening flight the helicopter was flying at the expected ~90 m altitude. At this altitude the pancake-like ice can be resolved, although the image quality was poor due to the decreasing sunlight at the time of acquisition (21:55) (Figure 4.30).

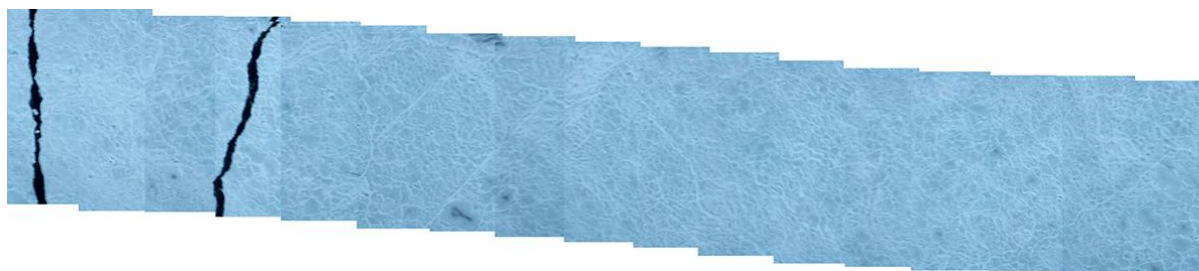


Figure 4.30: Mosaic of video frames 11200-11215 over deformed ice north of Tracadie Bay, PEI (February 26, 21:55). The mosaic has a length of ~596 m and width of ~96 m. The image brightness has been increased to compensate for the low illumination in the original data.

Unfortunately, the GPS system failed part way through the evening flight so the exact position of the video frames presented in Figure 4.30 is unknown. The field log (DFO, 2009) states that, in agreement with the available GPS data, the helicopter was returning directly to Charlottetown. The approximate position of the flight line has therefore been estimated as a direct line between Charlottetown Airport and the last reported GPS position. Given the minimal time difference (<10 min) between the acquisition of the evening RADARSAT-2 data and the evening video data over the bright region, features observed in both datasets could be used to estimate the position of the video mosaic shown in Figure 4.30. First the mobile pack ice edge was identified and working backwards (northwards) through the video frames a large lead (~200 m wide) was identified in both the video and RADARSAT-2 data. This lead was bounded on each side by pancake-like ice. Further northeast along the flight line a large, level, snow covered floe was observed in the video data. This large floe appears as a region of lower backscatter in the SAR image. Beyond this level floe the pancake-like ice reappears and eventually gives way to the homogenous pack ice, which is composed of large level FY ice floes. The pancake-like ice observed in the video data is once again well aligned with the regions of high HV backscatter in the RADARSAT-2 data (Figure 4.26). In contrast to the white colour observed further west within this deformed ice region, the pancake-like ice along this flight path appears light blue in colour, indicating a strong HV return (~ -19 dB) but a less strong HH return (~ -9 dB). It is not clear why the HH backscatter along this flight line is reduced relative to other portions of this deformed ice region. Nevertheless, the dual-pol data provides excellent visual contrast between the large level floes and the surrounding deformed pancake-like ice. Mean backscatter values derived from regions of interest (ROIs) digitized over the field validated ice targets further reinforce these findings (Figure 4.31). Each ROI contained at least 1000 pixels.

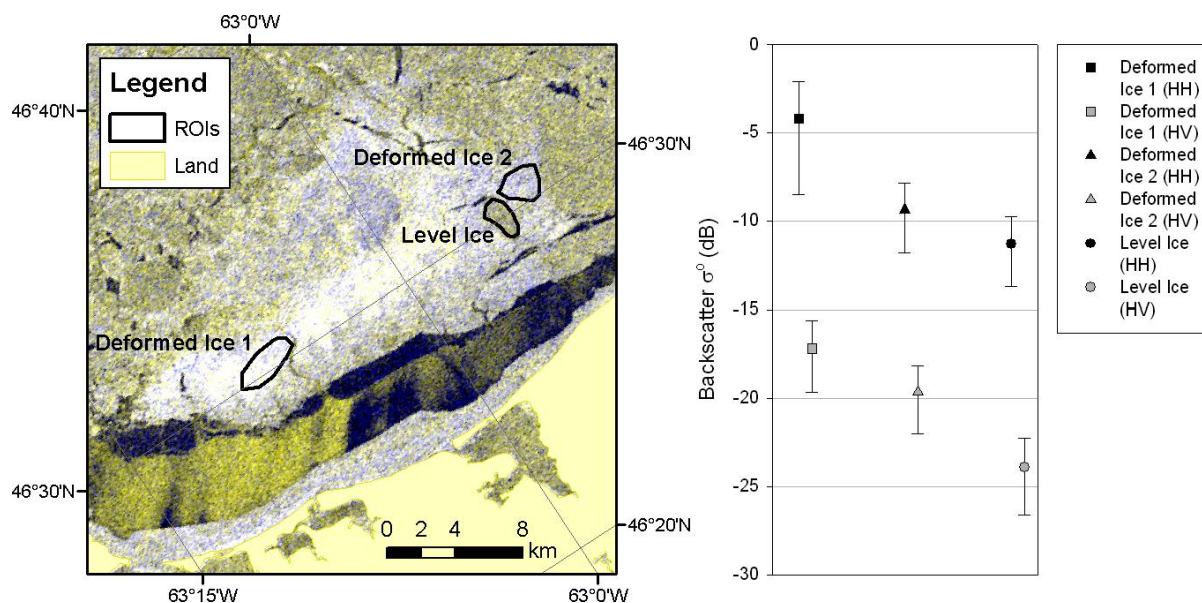


Figure 4.31: Mean backscatter ± 1 standard deviation for field validated deformed and level ice features observed in the February 26 (21:52) RADARSAT-2 data. The image is visualized as a colour composite (R-HH; G-HH; B-HV). RADARSAT-2 data and products © MacDonald, Dettwiler and Associates Ltd 2009 – all rights reserved.

Over both of the deformed ice ROIs the HV backscatter is high compared to that of the level ice ROI. In contrast, the HH backscatter from deformed ice ROI 2 and the level ice ROI are not separable. For this region of pancake-like ice the HV channel provides improved separability between the level and deformed ice.

Between February 26 and March 5 the ice in this region was subject to considerable compaction and shearing. As a result, the area of high backscatter in the March 5 SAR data took on an elongated linear shape, parallel to the fast ice edge. While no IcePic data were available over this region, video data was collected on the outbound and inbound legs of an afternoon flight to the Iles de la Madeleine. In addition to the pancake-like ice observed on February 26, areas of ridged ice and rubble were also observed in the video data. Backscatter was high from each of these deformed ice features (Figure 4.32).

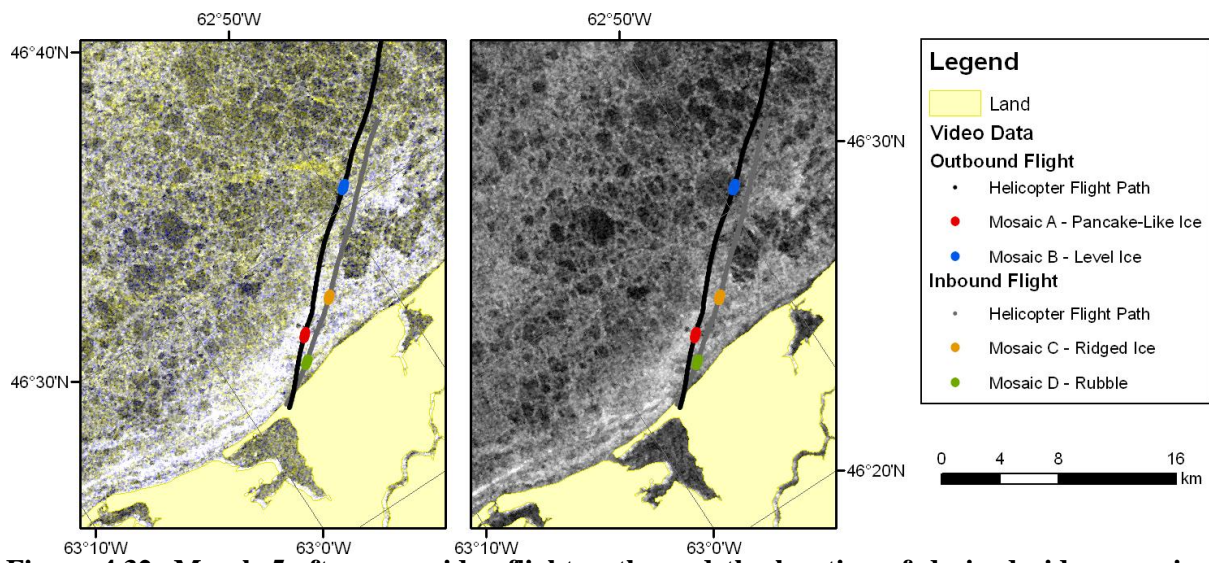


Figure 4.32: March 5 afternoon video flight paths and the location of derived video mosaics northeast of Tracadie Bay, PEI. The SAR data are (left) dual-pol RADARSAT-2 SCWA (10:27) and (right) Envisat/ASAR HH (14:19). The RADARSAT-2 image is visualized as a colour composite (R-HH; G-HH; B-HV). RADARSAT-2 data and products © MacDonald, Dettwiler and Associates Ltd 2009 – all rights reserved. Envisat data © ESA 2009.

Video mosaics of each of the three observed deformed ice features (pancake-like ice, ridged ice, and rubble), as well as a mosaic of a large level floe north of the deformed ice are presented in Figure 4.33.

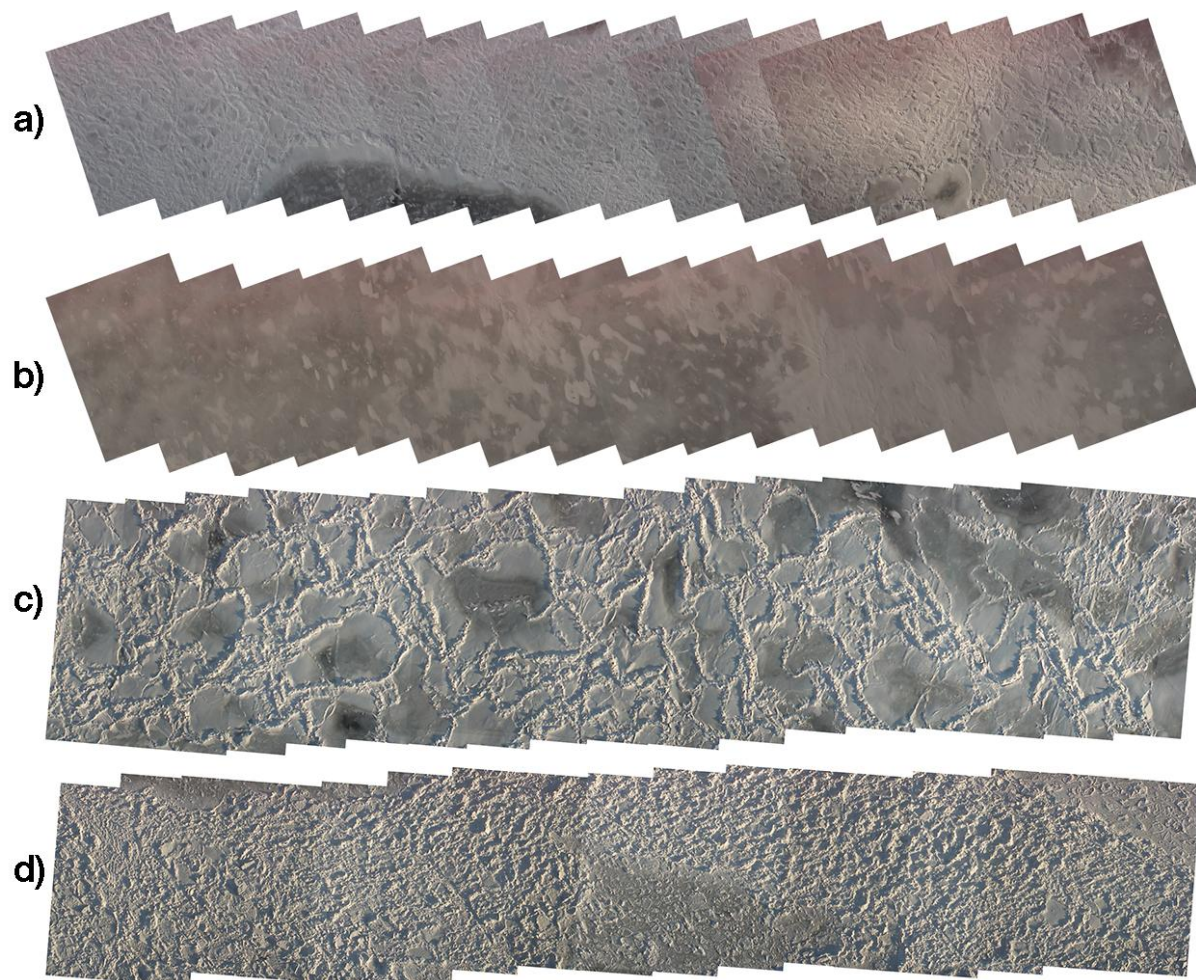


Figure 4.33: Video mosaics of March 5 ice conditions northeast of Tracadie Bay, PEI. a) pancake-like ice (18:05, frames 33785-33800, length ~553 m, width ~90 m); b) level ice (18:08, frames 34105-34200, length ~597 m, width ~100 m); c) heavily ridged ice (21:00, frames 42735-427350, length ~547 m, width ~117 m); and d) rubble ice (21:02, frames 42910-42925, length ~568 m, width ~96 m).

Once again ROIs were digitized for the field validated ice features, and backscatter statistics were derived to evaluate the separability of the level and deformed ice features. Individual ROIs were created for the level floe and for the ridged ice, while the pancake-like ice and rubble ice were combined into one ROI. The pancake-like ice and rubble ice were combined into one ROI because these features were not visually separable in the RADARSAT-2 data (both appeared bright white) and because of the proximity of these ice features. The backscatter statistics indicate that all of the deformed ice features are separable from the level ice, although the contrast between the ridged ice

and level ice is less than the contrast between the pancake-like and rubble ice and the level floe (Figure 4.34).

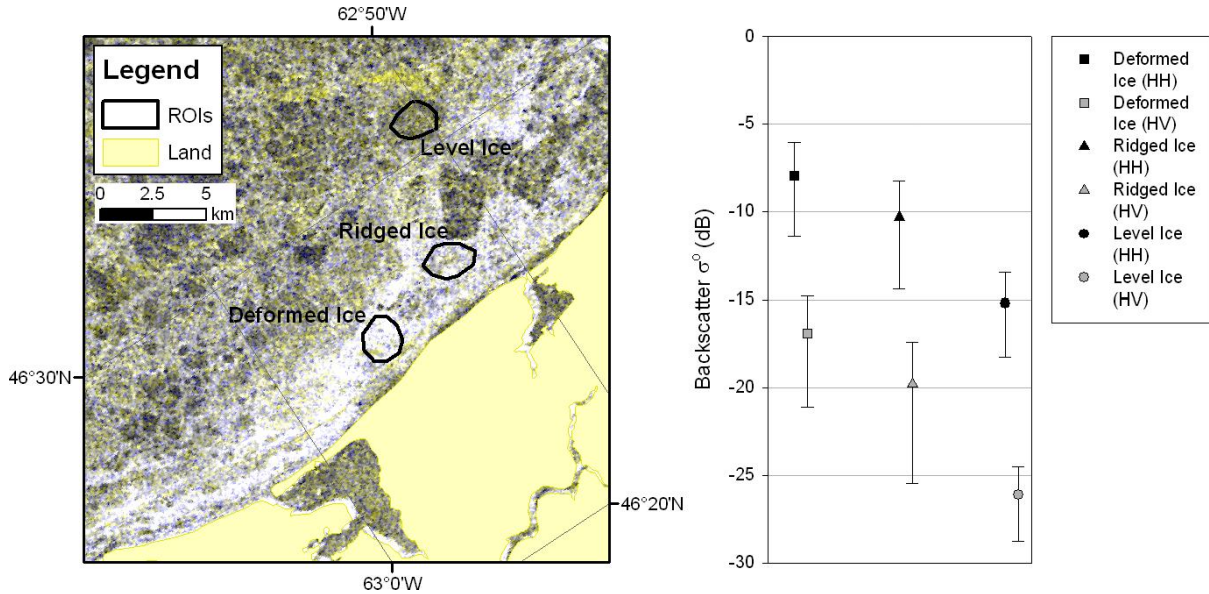


Figure 4.34: Mean backscatter ± 1 standard deviation for field validated deformed ice (pancake-like ice and rubble), heavily ridged ice, and level ice features observed in the March 5 (10:27) RADARSAT-2 data. The image is visualized as a colour composite (R-HH; G-HH; B-HV). RADARSAT-2 data and products © MacDonald, Dettwiler and Associates Ltd 2009 – all rights reserved.

Once again the contrast between the heavily deformed ice and the level ice is greater in the HV channel than in the HH channel. In contrast to the backscatter statistics for the February 26 image, the variance for each ROI is larger in the March 5 data. This is particularly true for the ridged ice ROI. The large variance of the ridged ice ROI can be explained by the fact that a considerable percentage of the surface area within this ROI is in fact level ice. As a result, there is some overlap in the backscatter signatures of the ridged ice and level ice ROIs. Nevertheless, the mean backscatter values of the ridged and level ice ROIs are well separated in the HV channel and these ice features could be visually separated in the colour composite. Given that the ice in this ROI was heavily ridged, it is expected that the contrast between areas of light or moderate ridging and level ice would be further reduced.

The second bright ice target identified by the CIS was a linear feature observed on March 5 in the eastern portion of Northumberland Strait, just offshore from the southwestern part of Cape Breton. This feature was not present in any SAR data prior to March 5 and the CIS had no explanation for the cause of the high backscatter. Deformed ice was not expected as winds were from the west throughout March 4 and 5 and any ridging would have been expected along the Cape Breton coastline against which the ice was being compacted. New ice and open water were present west of the feature, and floes of FY ice were present to the east (Figure 4.35).

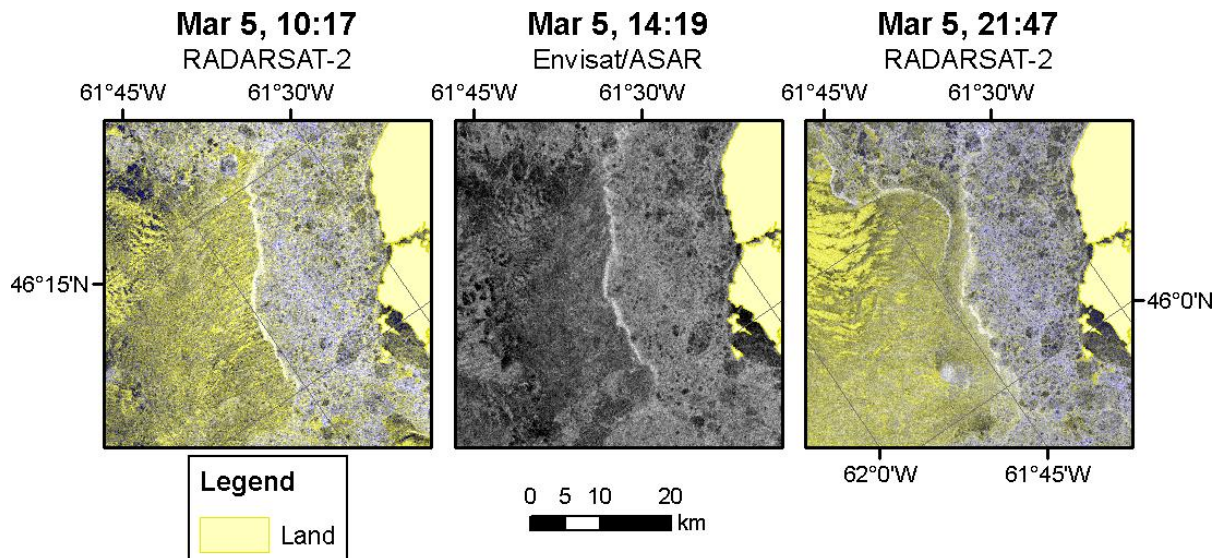


Figure 4.35: Dual-pol (HH/HV) RADARSAT-2 (SCWA 10:17; SCNA 21:47) and single-pol (HH) Envisat/ASAR (14:19) imagery of a high backscatter feature near southwestern Cape Breton, March 5. The RADARSAT-2 data are visualized as colour composites (R-HH; G-HH; B-HV). RADARSAT-2 data and products © MacDonald, Dettwiler and Associates Ltd 2009 – all rights reserved. Envisat data © ESA 2009.

Video and IcePic data were collected over this feature on the morning of March 5. Video data was collected flying eastwards over the feature, followed by IcePic collection westward along the same flight path. A second transect perpendicular to the bright feature was collected ~5 km south of the initial transect. All of the IcePic and video data were collected between 14:08 and 14:32 (within 15 minutes of the ASAR acquisition). The helicopter flight path is plotted on Figure 4.36.

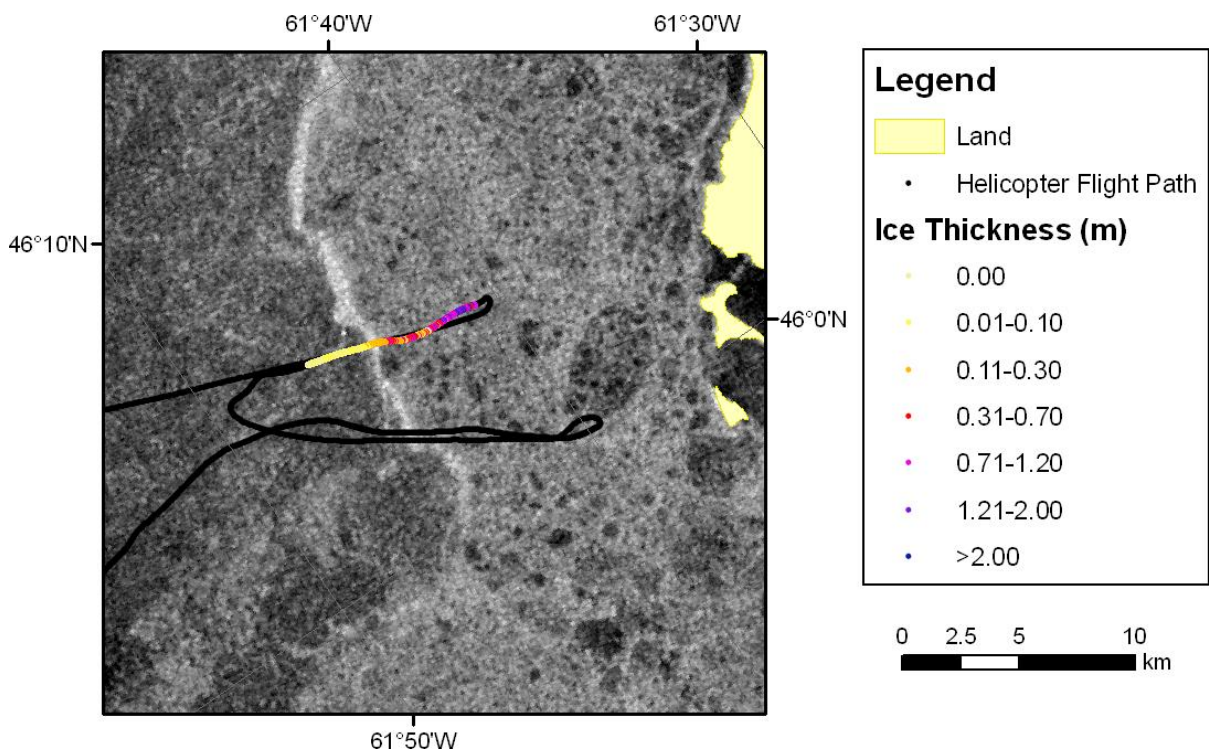


Figure 4.36: Helicopter flight path for the morning of March 5. Ice thickness data acquired at 14:15 are overlaid on the Envisat/ASAR (HH) image (14:19). Envisat data © ESA 2009.

Between PEI and the western edge of the FY pack ice, moderate to high concentrations of grease ice, nilas and pancake ice were observed. Moving eastwards pancake ice became increasingly common, although the rims on the pancakes were generally poorly developed. This pancake ice would have been formed from nilas that had been broken down and herded eastwards by the consistent westerly winds on March 4 and 5. Approaching the FY pack ice the rims on the pancakes were increasingly developed and the concentration of pancake ice increased. Along the western edge of the FY pack ice significant amounts of pancake ice with well-developed rims had accumulated, causing the bright radar returns. These cakes were of high (9+/10) concentration and were heavily rafted (Figure 4.37).



Figure 4.37: Rafted pancake ice with well-developed rims observed in eastern Northumberland Strait, March 5. The photo was taken facing west. The camera altitude was ~5 m.

To the east of this rafted pancake ice the FY ice pack consisted of small floes (typically <100 m) whose perimeters were deformed. Consolidated brash ice was common between the FY floes. The transition from new ice to rafted pancake ice to rough FY ice is evident in the IcePic Data (Figure 4.38). Note that the IcePic transect was collected flying westward so it begins over FY ice in the east and terminates over new ice in the west.

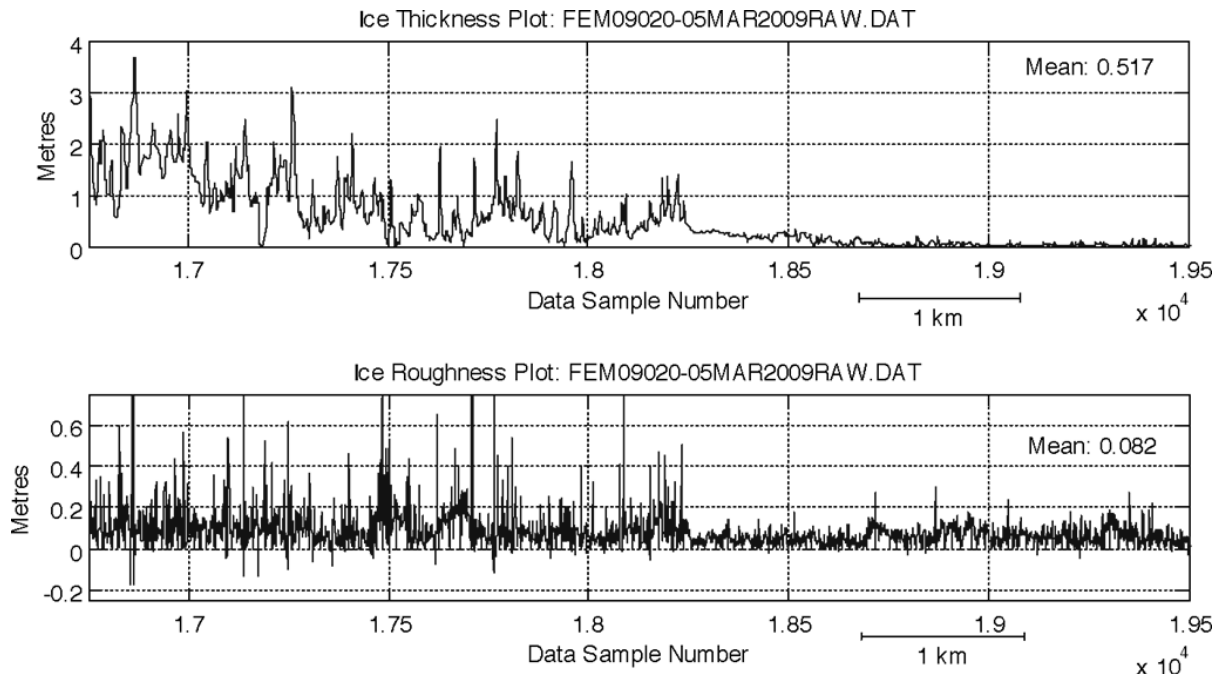


Figure 4.38: Ice thickness and surface roughness profiles in the vicinity of the bright linear feature observed in eastern Northumberland Strait, between PEI and Cape Breton (March 5, 14:13-14:17).

Given that this profile was collected within 5 minutes of the ASAR acquisition the IcePic samples could be compared directly to coincident ASAR pixels. The high backscatter feature in the SAR data and IcePic samples 18300-18600 were coincident, and the interpretation of this bright feature as being rafted pancake ice was in agreement with the IcePic data for these samples. In this region the mean ice thickness was 20 cm and the mean surface roughness was 4.4 cm (Figure 4.39).

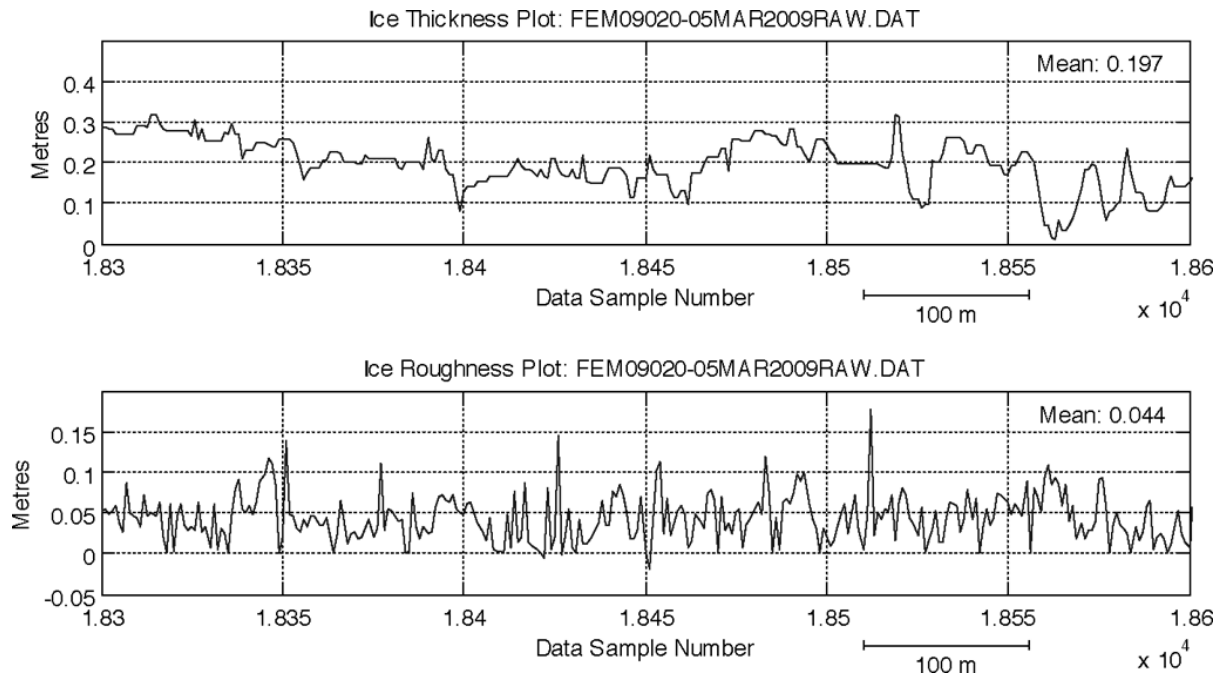


Figure 4.39: Ice thickness and surface roughness profiles over rafted pancake ice in eastern Northumberland Strait, between PEI and Cape Breton (March 5, 14:15).

Given that the surface roughness of this pancake ice was very similar to the radar wavelength, diffuse scattering would dominate. Strong diffuse scatter explains the very high HH backscatter from the pancake ice, while the high HV backscatter suggests that multiple-surface scatter also contributed to the backscatter signature of the pancake ice.

For both of the bright features identified by the CIS, deformed ice was found to be the cause of the high backscatter. The contrast between these heavily deformed ice features and level ice was greater in the HV channel than in the HH channel. These results indicate that, relative to single co-pol data, dual-pol C-band ScanSAR data should improve the discrimination between level and heavily deformed ice; however, the improved deformed ice information in the dual-pol data is not necessarily ideal for tactical considerations as the thickness of the deformed ice features identified did not appear to correspond to the amplitude of the HH or HV backscatter. Ridged and rubble ice, both of which are thick deformed ice features that pose a significant threat to navigation, either could not be separated from thinner (pancake-like) deformed ice or had reduced contrast with level ice, relative to thinner

types of deformed ice. These results are in agreement with the findings of Johnston and Flett (2001) who, using RADARSAT-1 (HH) ScanSAR data, found that individual ridges could not be identified within a matrix of thinner deformed ice. The results presented here suggest that the addition of the HV channel does not overcome this limitation of wide swath C-band SAR data. Furthermore, while these results show that areas with a heavy concentration of ridged ice are separable from level ice at the spatial resolution of the ScanSAR data, it is expected that areas of light and moderately ridged ice would be less separable from level ice (due to the increased area of level ice within each pixel).

4.4.2 Backscatter from Ridged Ice Identified in Observed Ice Charts

In this section the backscatter from areas of ridged ice, identified in observed ice charts, is evaluated to determine whether or not areas of light and medium ridging (<4/10 concentration) are separable from areas where no ridging is reported. None of the observed ice charts produced during SGULF09 indicated the presence of areas of heavy ridging ($\geq 4/10$ concentration). This analysis was favoured towards shipboard and helicopter observations as ridges can easily be identified from these platforms. While ridges can be identified from airplanes, the higher altitude of these observations may reduce the accuracy of ridge detection. Here the ridged ice information from two observed ice charts produced on February 26 is compared to the backscatter data from the evening (21:52) dual-pol RADARSAT-2 data.

ISS shipboard observations from the CCG icebreaker *Louis S. St-Laurent* (call sign CGDN) reported variable concentrations of ridged ice in the mobile pack ice to the east of the Iles de la Madeleine on February 26. While the valid time of the ice chart (11:00 to 20:30) spans most of the day, the ship track can be identified in the RADARSAT-2 data. The ship track is centred within three ice polygons on the observed ice chart, and the icebreaker itself, which appears as a bright point target, can be identified at the southern end of these ice polygons. These observations indicate that little ice drift occurred between the digitizing of these polygons and the acquisition of the

and medium FY ice is also present. The presence of brash ice (2/10 concentration) in ice polygon F may generate greater diffuse and multiple-surface scattering leading to the slightly higher HH and HV backscatter (and brighter blue colour) of this region; however, this is unlikely as brash ice is observed at a higher concentration (3/10) in polygon D. Without further information it is not possible to determine what ice properties contributed to the slight differences in backscatter signatures for these ice polygons. Nevertheless, it is clear that the moderate ridging in polygon D was not sufficient to create a backscatter signature that is separable from level ice at the low spatial resolution of the ScanSAR data.

Helicopter observations reported variable concentrations of ridged ice within the pack ice between PEI and the Iles de la Madeleine on February 26. The helicopter flight track was northbound from Charlottetown to the ice beacons, then eastbound to the Iles de la Madeleine. The helicopter observations, recorded between 19:25 and 20:40, are compared to backscatter from the evening (21:52) dual-pol RADARSAT-2 data. Between 19:00 and 22:00 each of the four ice beacons drifted <2.5 km to the northeast. For the southernmost ice polygons (A and B), which are very short in the north-south direction, the ice drift could have a considerable impact on derived backscatter statistics. Additionally, the backscatter from these regions has already been discussed thoroughly in the previous section (the pancake-like ice is located within polygon B); therefore, ice polygons A and B, along with the fast ice polygons (E), are not considered here. According to the observed ice chart ridged ice is present in each of the remaining ice polygons, with the concentration of ridged ice varying from <1/10 to 2/10 (Figure 4.41).

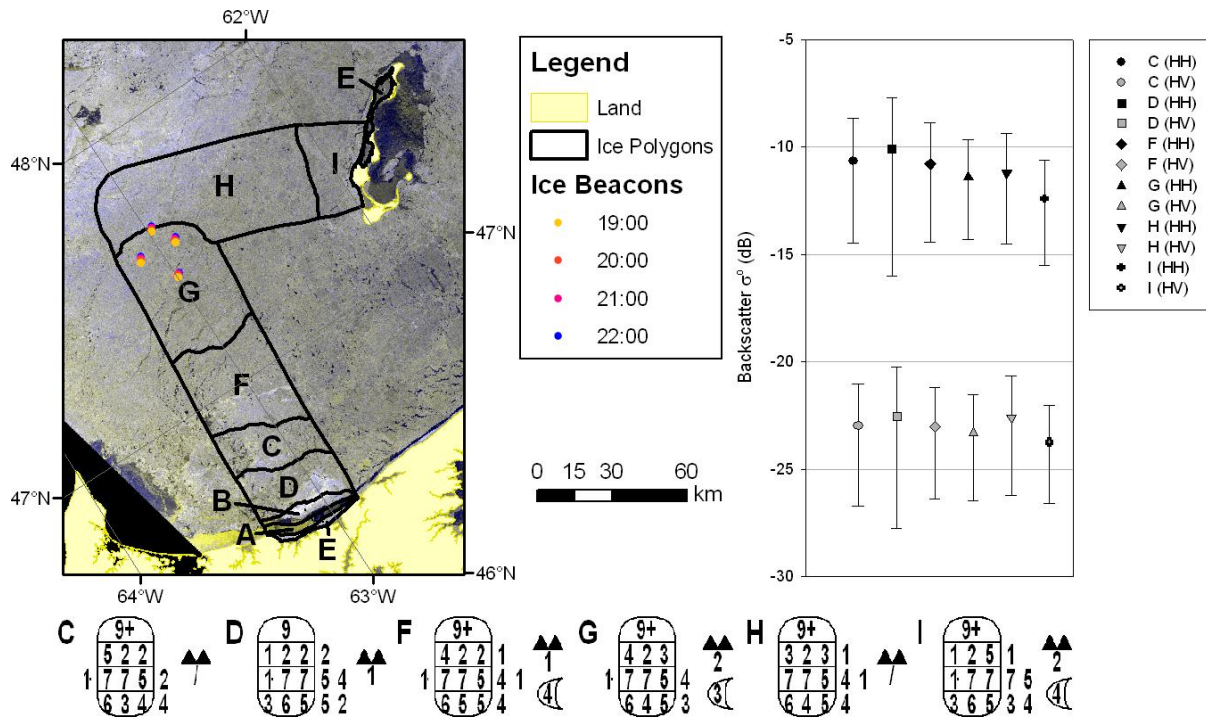


Figure 4.41: Mean backscatter ± 1 standard deviation for observed ice polygons of varying ridge concentration (CGYG recon #00019, 19:25-20:40), February 26. RADARSAT-2 data and products © MacDonald, Dettwiler and Associates Ltd 2009 – all rights reserved.

Once again, visual interpretation of the ScanSAR data did not suggest that there is any correspondence between the HH or HV backscatter from the ice polygons and the concentration of ridges within those ice polygons. The backscatter signatures for all of the ice polygons had considerable overlap and there was poor separation between their means (the range of mean values were < 2.5 dB and < 1.5 dB for the HH and HV channels, respectively). The consistent backscatter signatures were in part due to the fact that the distribution of ice types was fairly consistent between the polygons, with big and vast floes of thin FY ice being the predominant ice type, while medium FY ice and young ice were also present. While the ice types and size of floes in each polygon were similar, the variation in ridged ice concentration did not provide any separation between the backscatter signatures of the polygons. Polygon D (1/10 ridging) had the highest HH and HV backscatter, which can be attributed to the pancake-like ice present in the southern portion of this polygon. Polygons G and I, which had the highest concentration of ridged ice (2/10), had the lowest

mean backscatter values in both the HH and HV channels. Polygon H, which had only a trace ($<1/10$) of ridged ice, had the second highest mean HH and HV backscatter. Within the northwest portion of polygon H high backscatter ice was evident, but it is unclear what contributed to the stronger backscatter in this region. Video data collected along the flight path was analyzed but no significant changes in the ice conditions were observed between the brighter northwest portion and darker eastern portion of polygon H. Regardless, it is clear that the concentration of ridged ice was not a dominant control on HH or HV backscatter in the ScanSAR data where the concentration of ridged ice was light or moderate ($<4/10$).

These results suggest that, in contrast to regions of heavily deformed ice, the presence of light or moderately ridged ice ($<4/10$ concentration), is insufficient to produce a significant change in the dual-pol RADARSAT-2 ScanSAR backscatter from FY ice. For areas of heavily deformed ice ($\geq 4/10$) both the HH and HV backscatter were increased significantly allowing the heavily deformed ice to be separated from areas of level ice; however, this only applies to large areas that are much greater in size than the resolution of the ScanSAR data. Small, deformed features, such as individual ridges, cannot be resolved. The results also indicate that the contrast between heavily deformed ice and level ice is greater in the HV channel than in the HH channel. The increased contrast in the cross-pol channel is in agreement with expectations based on previous analyses of dual-polarization C-band SAR data from both airborne SARs (e.g. Rignot and Drinkwater, 1994; Flett, 1997) and spaceborne SARs (e.g. Scheuchl et al., 2004c; Arkett et al., 2007).

From an operational perspective the dual-pol RADARSAT-2 ScanSAR data provide improved level and deformed ice separation relative to single co-pol data as areas of heavily deformed ice can be reliably separated from level ice. This suggests that the relative roughness statistic and discretionary boundaries could potentially be implemented on image analysis charts if they were always annotated as areas of heavy deformation; however, the strategic and tactical value of

implementing the relative roughness statistic would be limited given that the thickness of the deformed ice did not correspond to the strength of the HH or HV backscatter. For example, pancake-like rafted young ice could not be separated from a nearby region of much thicker (and therefore more dangerous) rubble ice; therefore, an area of heavily deformed ice identified in a dual-pol RADARSAT-2 ScanSAR data does not necessarily represent a tactical hazard. Further analysis is recommended to determine if Ice Analysts could reliably use their *a priori* knowledge of ice conditions from preceding days to determine whether or not areas of heavily deformed ice are likely to present a tactical hazard. Feedback from ISS in the field would be required to validate the heavily deformed ice features identified by Ice Analysts. If the Ice Analysts can successfully use *a priori* knowledge to help them determine whether or not heavily deformed ice areas are likely to be ridged ice or rafted ice, the relative roughness symbology should be implemented; however, given the current understanding of the dual-pol RADARSAT-2 ScanSAR backscatter there is not sufficient confidence to implement the relative roughness symbology in a manner that would effectively support tactical operations. While the operational use of the deformed ice information in the RADARSAT-2 data appears limited, the use of a longer wavelength SAR (e.g. L-band) should reduce the sensitivity to small surface roughness features and increase the sensitivity to ridged ice. As a result, further research efforts targeted at separating level and deformed ice should be focused on evaluating multi-frequency (C- and L-band) ScanSAR data. This could be accomplished by comparing the backscatter from near coincident scenes of RADARSAT-2 and ALOS/PALSAR ScanSAR data.

From a climatology perspective, the improved separation of heavily deformed ice provided by the dual-pol RADARSAT-2 ScanSAR data, relative to single co-pol data, is not expected to provide any benefits to derived sea ice climate data records because the amplitude of the dual-pol backscatter was not found to correspond to the thickness of the deformed ice features. Furthermore, areas of light and moderately ridged ice (which are more common and cover much larger extents than heavily deformed

ice) cannot be identified in the dual-pol data. As a result, dual-pol RADARSAT-2 data are not expected to provide any improvements to sea ice thickness climate data records. Looking forward, research efforts should focus on forthcoming altimeter missions (e.g. ICESat-2 and CryoSat-2), as these missions have shown much greater potential for producing accurate ice thickness measurements at global scales.

Chapter 5

Conclusions and Recommendations

5.1 Conclusions

Over the past two decades operational ice centres have relied primarily on wide swath single co-pol C-band ScanSAR data to monitor sea ice conditions in support of human marine activity and sea ice climatology studies. However, single co-pol data is subject to several limitations, including weak separation between ice and open water at steep incidence angles and high wind speeds, and the inability to separate level and deformed ice. In this study, the sea ice information content of dual-pol (HH/HV) RADARSAT-2 ScanSAR data acquired over the Gulf of St. Lawrence in the winter of 2009 was evaluated to determine what new or improved ice information can be derived from wide swath dual-pol C-band SAR data, relative to single co-pol data.

In order to evaluate the ice information content of the dual-pol RADARSAT-2 ScanSAR data, optical remote sensing datasets and ice thickness and surface roughness measurements collected during the SGULF09 field campaign were compared to backscatter signatures observed in the RADARSAT-2 data. MODIS Level 1B imagery (MOD02HKM) and sea ice extent products (MOD29) were acquired to validate ice edge and ice concentration estimates derived from the dual-pol data. Field data, acquired with helicopter-borne remote sensing instruments, included ice thickness and surface roughness measurements and geotagged video stills. Additionally, visual observations acquired by ISS were available in the form of observed ice charts. These data were used to identify the ice properties related to the various backscatter signatures observed in the dual-pol data. Ice drift data, acquired from four GPS ice beacons and from the CIS Ice Tracker algorithm, were in good agreement with winds recorded at weather stations around the southern Gulf. The ice drift, ice tracker and wind data were used to help compensate for the movement of ice between the acquisitions times of the RADARSAT-2 data and the field data.

In the eight dual-pol RADARSAT-2 ScanSAR images acquired during SGULF09, several significant differences were observed between the HH and HV images. The most apparent difference was the backscatter signature of open water. The HH backscatter from open water, which is dependent on incidence angle and wind speed, varied considerably across range and from image to image. In SCWA data (20° - 49°) the HH backscatter from open water was observed to decay by as much as 20 dB across range. This decay results in a crossover of the backscatter signatures of ice and open water, which can reduce the separability of ice and open water. The incidence angle at which this crossover occurs is dependent upon wind speed and ice conditions. In this study, the separation of ice and open water in the HH data was acceptable at incidence angles $>30^{\circ}$ for wind speeds <20 km/hr. At steeper incidence angles some areas of the HH data were subject to minimal or no separation between ice and open water. In contrast to the HH channel, the HV backscatter from open water was stable across range in all images, with backscatter values ranging between -24 and -28 dB. Visual analysis of the HV data indicated that ocean surface features could be resolved in the HV data, suggesting that the HV backscatter from open water is above the NESZ of RADARSAT-2; however, system and processing artefacts (e.g. beam seams) were prominent, indicating that the SNR for open water is low in the HV channel. Given that the HV backscatter from open water is stable across range, a range dependent crossover of ice and open water signatures does not occur; however, new ice and open water could not be separated at any incidence angle in the HV ScanSAR data. When the HH and HV data are combined as a false colour composite the limitations of each channel are overcome and open water can be separated from new, young and FY ice with confidence regardless of imaging geometry or wind speed.

The backscatter signatures of new ice, young ice and FY ice also demonstrated some variation between the HH and HV channels. The greatest difference was the lack of a separable new ice signature in the HV data. For young and FY ice, the backscatter contrast between these ice types was

reduced in the HV channel, relative to the HH channel. Based on previous analyses of Envisat/ASAR AP data, it was expected that the HV data should provide improved floe structure information for FY ice (as the edge of FY floes are often ridged); however, the HV data were not found to provide any enhanced floe structure information relative to the HH data. This is likely a limitation of the low spatial resolution of the ScanSAR data. As a result, the HV data did not provide any significant new ice information that could be used to enhance the separation of ice types. Ice type distributions reported in image analysis chart egg codes derived from the dual-pol RADARSAT-2 ScanSAR were compared to ice thickness measurements collected with the IcePic. The ice types and partial concentrations reported in the egg codes were found to be in good agreement with the IcePic data. These results indicate that ice type information derived from analysis of dual-pol ScanSAR data is acceptable and the inclusion of the HV channel does not appear to bias ice type estimates.

In the dual-pol RADARSAT-2 data several bright (high backscatter) features were identified and IcePic and video data collected over these features were used to identify the ice properties that caused the strong HH and HV backscatter. Each of the bright features was an area of heavily deformed ice. Backscatter statistics were extracted from the deformed ice features and from nearby level ice and the contrast between the level and deformed ice was found to be greater in the HV channel than in the HH channel. These results indicate that the dual-pol data improve the separability between level and deformed ice; however, the deformed ice information in the dual-pol data is not necessarily ideal for tactical considerations as the thickness of the deformed ice features did not correspond to the amplitude of the HH or HV backscatter. While areas of heavily deformed ice could be identified, this was not the case for areas of light and moderately ridged ice. Backscatter statistics were extracted for ice polygons from observed ice charts and were compared to ridge concentrations reported in the egg codes. The extracted backscatter signatures were not separable regardless of whether the egg code reported no ridging or 3/10 ridged ice. This is likely a limitation of the spatial resolution of the

ScanSAR data and the mixed pixel effect. Individual ridges, which are much smaller than the spatial resolution of the ScanSAR data, cannot be resolved and the backscatter from pixels containing light or moderately ridged ice are dominated by the contribution of the level ice.

From an operational perspective the acquisition of dual-pol RADARSAT-2 data provides several benefits relative to single co-pol data. The primary benefits for operational ice monitoring are derived from the improved separation of ice and open water. The increased contrast between open water and new, young and FY ice will improve the accuracy of ice edge and total ice concentration estimates in image analysis charts where ice-open water signature crossovers are present in the HH data. Furthermore, the time required to delineate the ice edge and to estimate total ice concentrations should be reduced. During the period of maximum ice extent these benefits will be limited as most images contain only small areas of open water. During the freezeup and breakup periods these benefits are likely to be greater as there is increased potential for ice-open water signature crossovers, as more open water is present at these times. The improved ice-open water contrast also suggests that the development of fully or semi-automated image segmentation algorithms capable of separating ice from open water is plausible. If such algorithms are successfully developed, they could be implemented in an operational context to automate the delineation of the ice edge and the estimation of total ice concentrations. Given the reduced contrast between new, young and FY ice types, dual-pol data are not expected to increase the accuracy of ice type and partial concentration estimates. The accuracy of these parameters is maintained relative to single co-pol data. Finally, the improved contrast between heavily deformed ice and level ice suggests that the relative roughness symbology and discretionary boundaries could be implemented to identify heavily deformed ice on image analysis charts; however, the thickness of heavily deformed ice (and the tactical risk that it poses) cannot be determined from backscatter data alone. Further validation is required to determine if ice analysts can use their knowledge of ice conditions from previous days to reliably determine whether

heavily deformed ice is likely to be rafted ice or ridged ice. This will require feedback from ISS in the field to validate the heavily deformed ice features identified by the ice analysts. If heavily rafted and heavily ridged ice can reliably be separated then the relative roughness symbol and discretionary boundaries should be implemented on image analysis charts.

From a climatology perspective the acquisition of dual-pol RADARSAT-2 ScanSAR data is likely to provide only marginal benefits. The reduced impact of the benefits of dual-pol SAR data on climate data records, relative to image analysis charts, is due to the fact that the information derived from the SAR data is combined with ice information from numerous other datasets in the creation of regional ice charts (from which sea ice climate data records are derived). Given the smaller map scale of regional ice charts, the level of detail of ice information derived from image analysis charts must be generalized; therefore, any increased accuracy of ice extent and ice concentration data provided by dual-pol imagery are likely to have a reduced impact on regional ice charts, relative to image analysis charts. Additionally, given that the thickness of heavily deformed ice features did not correspond to HH or HV backscatter amplitude, and that areas of light and moderately ridged ice could not be separated from areas of level ice, dual-pol RADARSAT-2 ScanSAR data are not expected to provide improved estimates of ice thickness for climate data records.

5.2 Recommendations

Given the improved ice-open water and level-deformed ice separation provided by dual-pol RADARSAT-2 ScanSAR data, relative to single co-pol data, it is recommended that operational ice centres acquire dual-pol ScanSAR data whenever possible. While the additional financial cost of dual-pol data is marginal, it may not be feasible to acquire dual-pol data for all operational acquisitions. If this is the case dual-pol acquisitions should be ordered during to the freezeup and breakup periods, because the crossover of ice and open water signatures is more likely to occur at

these times when open water is more common. As observed during SGULF09, the improved separation of ice and open water during the period of maximum ice extent is generally limited to small areas, as most areas are completely ice covered at this time of year.

The results presented in this study indicate that the ice information content of the dual-pol RADARSAT-2 ScanSAR data can be exploited most effectively when the two polarization channels are combined into a false colour composite. When viewing the data as two separate greyscale images the information content of the two channels is difficult to synthesize. The switch from greyscale (single co-pol) data, to colour composite (dual-pol) data is not expected to pose a significant challenge to ice analysts as they have years of experience analyzing false colour composites of optical datasets. However, it is recommended that the ice analysts be trained on the HV backscatter signatures for open water and new, young and FY ice, so that they can accurately interpret the surface properties that are related to specific colours in the false colour composite (e.g. open water in the near range appears yellow in colour, new ice appears dark blue in colour). Furthermore, the effect of local image enhancements on the appearance of the colour composite needs to be evaluated. This evaluation should be carried out with significant input from the ice analysts.

5.3 Future Work


While the dual-pol RADARSAT-2 ScanSAR data were found to be beneficial in the context of operational sea ice monitoring, the results presented in this study are limited to ice that is no older than the FY stage of development and to winter ice conditions. Further work is recommended to assess the operational value of dual-pol RADARSAT-2 ScanSAR data over additional ice regimes. First, dual-pol data should be evaluated for ice regimes where MY ice is present. Given its low salinity and high air bubble content, MY ice produces strong volume scattering; therefore, cross-pol backscatter should be enhanced, relative to younger, smooth ice types, which generate less volume

scatter. As a result, dual-pol data may provide improved separation of FY and MY ice. Results from airborne SAR campaigns suggest that this is the case, but these expectations need to be evaluated at the spatial resolution, incidence angle range and NESZ of RADARSAT-2 ScanSAR data. Second, the backscatter signatures of dual-pol RADARSAT-2 ScanSAR data need to be evaluated during the melt period to determine whether or not any of the benefits provided by the cross-pol channel are still achieved when wet snow and melt ponds are present on the ice surface.

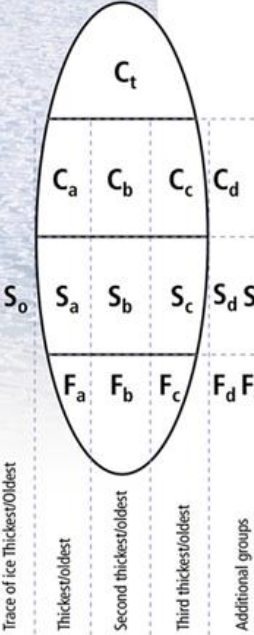
In addition to evaluating dual-pol data over additional ice regimes and seasons, future research efforts should focus on evaluating the sea ice information content of multi-parameter (multi-polarization and multi-frequency) SAR data at wide swath widths. Results from airborne SAR campaigns indicate that backscatter signatures have a stronger dependence on frequency than on polarization; therefore, multi-frequency SAR data may provide enhanced ice information relative to multi-polarization data. In particular, L-band SAR data should be less sensitive to small surface roughness features (rafted ice) and should be more sensitive to larger surface roughness features (ridged ice and rubble fields); therefore, deformed ice that presents a tactical hazard may be separable from level ice and rafted ice, but this has not been evaluated for ScanSAR data. While multi-frequency SAR data are not available from any existing spaceborne SAR system, the acquisition of near coincident data from multiple platforms (e.g. RADARSAT-2, ALOS/PALSAR) could be used to evaluate the potential of multi-parameter ScanSAR data in the context of operational sea ice monitoring.

Appendix A

Egg Code Definition


Environment Canada / Environnement Canada

KEY TO ICE SYMBOLS









Total Concentration of ice, reported in tenths.

Partial concentration in tenths of thickest (C_a), second thickest (C_b) and third thickest (C_c) ice types with C_a , C_b and C_c 1/10 or more. If only one thickness type is present C_a equals C_t and the second level is left blank.

Stage of development (age) of ice concentration reported by C_a , C_b and C_c .

Development stage (age) of remaining ice types. S_0 if reported is a trace of ice thicker/older than S_a . S_d is a thinner ice which is reported when there are four or more ice thickness types.

Predominant form of ice (floe size) corresponding to S_a , S_b and S_c respectively.

-  Open Water
-  Fast Ice
-  Ice Free
-  Bergy Water
-  Target Water
-  Ice Drift (NM/Day)

Stage of Development Sea Ice ($S_0S_aS_bS_cS_dS_e$)

Description	Thickness	Code
New	<10 cm	1
Nilas; Ice rind	<10 cm	2
Young	10-30 cm	3
Grey	10-15 cm	4
Grey-white	15-30 cm	5
First-year	≥ 30 cm	6
Thin first-year	30-70 cm	7
Medium first-year	70-120 cm	1•
Thick first-year ice	>120 cm	4•
Old		7•
Second-year		8•
Multi-year		9•
Ice of land origin		▲•
Undetermined, unknown		X

Form of Ice ($F_aF_bF_cF_dF_e$)

Description	Width	Code
Pancake ice		0
Small ice cake, brash ice	<2 m	1
Ice cake	2-20 m	2
Small floe	20-100 m	3
Medium floe	100-500 m	4
Big floe	500-2000 m	5
Vast floe	2-10 km	6
Giant floe	>10 km	7
Fast ice		8
Icebergs		9
Undetermined, unknown or no form		X
Ice in strips in which concentration is C		∞ C

Stage of Development Lake Ice ($S_0S_aS_bS_cS_dS_e$)

Description	Thickness	Code
New	<5 cm	1
Thin	5-15 cm	4
Medium	15-30 cm	5
Thick	30-70 cm	7
Very thick	>70 cm	1•
Undetermined, unknown		X



Canadian Ice Service (CIS)

Client Services
373 Sussex Drive, E-3
Ottawa, Ontario
K1A 0H3

Tel.: 1 800 767 2885 (Canada) and (613) 996-1550
Fax: (613) 947-9160
Email: cis-scg.client@ec.gc.ca
Web site: <http://ice-glaces.ec.gc.ca>



Figure A.1: Full description of the egg code and key ice chart symbols (MSC, 2005).

References

- Amante, C., and B.W. Eakins (2001). ETOPO1 Arc-Minute Global Relief Model: Procedures, Data Sources and Analysis. *NOAA Technical Memorandum NESDIS NGDC-24*, 19 pp.
- Arkett, M., D. Flett and R. De Abreu (2007). C-band multiple polarization SAR for sea ice monitoring – What can it do for the Canadian Ice Service. In *Proceedings of the Envisat Symposium 2007*, April 23-27, 2007. Montreux, Switzerland.
- Arkett, M., D. Flett, R. De Abreu and C. Gillespie (2006). Sea Ice Type and Open Water Discrimination for Operational Ice Monitoring with RADARSAT-2. *IEEE 2006 International Geoscience and Remote Sensing Symposium Proceedings*, 1631-1634.
- Carsey, F.D., R.G. Barry and W.F. Weeks (1991). Chapter 1: Introduction. In F.D. Carsey (Ed.), *Microwave Remote Sensing of Sea Ice*, AGU Geophysical Monograph 68, pp. 1-7. Washington: American Geophysical Union.
- CIS (2001). Sea Ice Climatic Atlas, East Coast of Canada, 1971-2000. Cat. No. En57-38/2000. [Electronic Resource] available from <http://ice.ec.gc.ca/IA_ECCA/Sea_Ice_Climatic_Atlas_East_Coast_of_Canada_1971_2000.pdf>
- CIS (2006). Canadian Ice Service Digital Archive – Regional Charts: History, Accuracy, and Caveats. CIS Archive Documentation Series No. 1. [Electronic Resource] available from <http://ice.ec.gc.ca/IA_DOC/cisads_no_001_e.pdf>
- CIS (2009). Seasonal Summary for Eastern Canada: Winter 2008-2009. [Electronic Resource] available from <http://ice.ec.gc.ca/IS_SS_EC/East_Coast_Seasonal_Summary_2008-09.pdf>
- Curry, J.A., J.L. Schramm and E.E. Ebert (1995). Sea Ice-Albedo Climate Feedback Mechanism. *Journal of Climate*, 8, 240-247.

- DFO (2007). Measuring Ice Properties with Helicopter-borne Instrumentation. Retrieved on May 14, 2010, from <http://www.mar.dfo-mpo.gc.ca/science/ocean/seaice/properties_e.html>
- DFO (2009). Southern Gulf of St Lawrence 2009 Ice survey. [Electronic resource] available from <<ftp://starfish.mar.dfo-mpo.gc.ca/pub/ocean/seaice/Gulf2009/>>
- Dierking, W., H. Skriver and P. Gudmandsen (2004). On the improvement of sea ice classification by means of radar polarimetry. In R. Goossens (Ed.) *Remote Sensing in Transition*, pp. 203-209. Millpress: Rotterdam.
- Drinkwater, M.R., R. Kwok, D.P. Winebrenner and E. Rignot (1991). Multifrequency Polarimetric Synthetic Aperture Radar Observations of Sea Ice. *Journal of Geophysical Research*, 96, C11, 20679-20698.
- EC (2005). Manual of Standard Procedures for Observing and Reporting Ice Conditions, revised 9th edition. [Electronic Resource] available from <<http://ice.ec.gc.ca/app/WsvPageDsp.cfm?Lang=eng&Inid=23&ScndLvl=no&ID=172>>
- ESA (1998). Envisat ASAR: Science and Applications. ESA Report SP-1225. [Electronic Resource] available from <http://earth.esa.int/pub/ESA_DOC/SP_1225.pdf>
- ESA (2009). Sentinel-1: GMES radar mission for land and ocean services. [Electronic Resource] available from <http://esamultimedia.esa.int/docs/S1-Data_Sheet.pdf>
- ESA (2010). ASAR Glossary Terms: Geometry Glossary. Retrieved on July 6, 2010 from <<http://envisat.esa.int/handbooks/asar/CNTR5-5.htm>>
- Flett, D.G. (1997). C-band Polarimetric Synthetic Aperture Radar Signatures of Winter Sea Ice Conditions. Masters Thesis, University of Waterloo, Waterloo, Ontario, Canada. 129 pp.

- Flett, D., R. De Abreu, M. Arkett and M.-F. Gauthier (2008). Initial Evaluation of RADARSAT-2 for Operational Sea Ice Monitoring. *IEEE 2008 International Geoscience and Remote Sensing Symposium Proceedings, 1*, 9-12.
- Freeman, T., and S.L. Durden (1998). A three-component scattering model for polarimetric SAR data. *IEEE Transactions on Geoscience and Remote Sensing, 36*, 3, 963-973.
- Haas, C., S. Gerland, H. Eicken, and H. Miller (1997). Comparison of sea-ice thickness measurements under summer and winter conditions in the Arctic using a small electromagnetic induction device. *Geophysics, 62*, 749 – 757.
- Hall, D.K., G.A. Riggs, and V.V. Salomonson (2001). Algorithm Theoretical Basis Document (ATBD) for the MODIS Snow-, Lake Ice- and Sea Ice-Mapping Algorithms. Greenbelt, MD: Goddard Space Flight Center. [Electronic Resource] available from <<http://modis-snow-ice.gsfc.nasa.gov/atbd.html>>
- Hallikainen, M., and D.P. Winebrenner (1992). Chapter 3: The Physical Basis for Sea Ice Remote Sensing. In F.D. Carsey (Ed.), *Microwave Remote Sensing of Sea Ice*, AGU Geophysical Monograph 68, pp. 29-45. Washington: American Geophysical Union.
- Holland, M.M., and C.M. Bitz (2003). Polar Amplification of climate change in coupled models. *Climate Dynamics, 21*, 221-232.
- Johnston, M. (2001). Validation of RADARSAT imagery using in situ measurements from first year ridged ice. *Proceedings of the 16th International Conference on Port and Ocean Engineering under Arctic Conditions (POAC '01)*, 3, 1129-1138.

- Johnston, M., and D. Flett (2001). First year ridges and RADARSAT ScanSAR imagery: influence of incidence angle and feature orientation. *Proceedings of the 4th International Symposium on Remote Sensing in Glaciology*, 4-8 June 2001, College Park, Maryland.
- Johnston, D.W., A.S. Friedlaender, L.G. Torres and D.M. Lavigne (2005). Variation in sea ice cover on the east coast of Canada from 1969-2002: climate variability and implication for harp and hooded seals. *Climate Research*, 29, 209-222.
- Key, J.R., J.B. Collins, C. Fowler, and R.S. Stone (1997). High latitude surface temperature estimates from thermal satellite data. *Remote Sensing of the Environment*, 61, 302-309.
- Kwok, R., S.V. Nghiem, S.H. Yueh, and D.D. Huynh (1995). Retrieval of Thin Ice Thickness from Multifrequency Polarimetric SAR Data. *Remote Sensing of Environment*, 51, 361-374.
- Kwok, R., G.F. Cunningham, M. Wensnahan, I. Rigor, H.J. Zwally and D. Yi (2009). Thinning and volume loss of the Arctic Ocean sea ice cover: 2003-2008. *J. Geophys. Res.*, 114, C07005, doi:10.1029/2009JC005312.
- Laidler, G.J., J.D. Ford, W.A. Gough, T. Ikummaq, A.S. Gagnon, S. Kowal, et al. (2009). Travelling and hunting in a changing Arctic: assessing Inuit vulnerability to sea ice change in Igloodik, Nunavut. *Climatic Change*, 94, 363-397.
- Lalumiere, L., S. Prinsenber and I. Peterson (2000). Observing Pack Ice Properties with a Helicopter-borne Video-Laser-GPS Sensor. *Proceedings of the 10th (2000) International Offshore and Polar Engineering Conference, Vol. 1*, 697-703.
- Lemke, P., J. Ren, R.B. Alley, I. Allison, J. Carrasco, G. Flato, et al. (2007). Observations: Changes in Snow, Ice and Frozen Ground. In S. Solomon, D. Qin, M. Manning, Z. Chen, M. Marquis, K.B. Averyt, et al. (Eds.), *Climate Change 2007: The Physical Science Basis* (pp. 337-383).

Contribution of Working Group I to the Fourth Assessment Report of the Intergovernmental Panel on Climate Change. Cambridge: Cambridge University Press.

Lillesand, T.M., R.W. Kiefer, and J.W. Chipman (2004). *Remote Sensing and Image Interpretation*. New York: John Wiley & Sons, Inc.

Livingstone, C.E. (1991). Synthetic Aperture Radar Images of Sea Ice. In S. Haykin, E.O. Lewis, R.K. Raney and J.R. Rossiter (Eds.) *Remote Sensing of Sea Ice and Icebergs*, pp. 541-610. New York: John Wiley & Sons, Inc.

Long, A.E. (1992). C-band V-Polarized Radar Sea Echo Model from ERS-1 Haltenbalken Campaign. In *Proceedings of URSI Microwave Signature Conference*. IGLS-Innsbruck, Austria.

Manabe, S., and R.J. Stouffer (1980). Sensitivity of a global climate model to an increase of CO₂ in the atmosphere. *J. Geophys. Res.*, 85, C10, 5529-5554.

Matsuoka, T., S. Uratsuka, M. Satake, T. Kobayashi, A. Nadai, T. Umehara, et al. (2001). CRL/NASDA airborne SAR (Pi-SAR) observations of sea ice in the Sea of Okhotsk. *Annals of Glaciology*, 33, 115-119.

MDA (2009). RADARSAT-2 Product Description. MDA Document RN-SP-52-1238, Issue 1/6, November 2, 2009. [Electronic Resource] available from <http://gs.mdacorporation.com/products/sensor/radarsat2/RS2_Product_Description.pdf>

Morey, R.M., A. Kovacs and G.F.N. Cox (1984). Electromagnetic properties of sea ice. CRREL Rep. 84-2, U.S. Army Corps of Engineers, Cold Regions Research and Engineering Laboratory. Hanover, N.H.

MSC (2005). MANICE: Manual of Standard Procedures for Observing and Reporting Ice Conditions, Revised Ninth Edition. Meteorological Service of Canada Catalogue No. En56-175/2005.

- [Electronic Resource] available from
<<http://ice.ec.gc.ca/app/WsvPageDsp.cfm?Lang=eng&lnid=23&ScndLvl=no&ID=172>>
- NASA (2010). "MODIS Rapid Response System FAQ: What do the different band combinations mean?" Retrieved April 28, 2010 from <<http://rapidfire.sci.gsfc.nasa.gov/faq/#faq04>>
- Nghiem, S.V., and C. Bertoia (2001). Study of Multi-Polarization C-Band Backscatter Signatures for Arctic Sea Ice Mapping with Future Satellite SAR. *Canadian Journal of Remote Sensing*, 27, 5, 387-402.
- Nghiem, S.V., R. Kwok, S.H. Yueh and M.R. Drinkwater (1995). Polarimetric signatures of sea ice 1 – Theoretical model. *Journal of Geophysical Research*, 100, C7, 13665-13679.
- Olsen, R., P. Vachon and D.J. Weydahl (2010). Cross-pol assisted wind retrieval from RADARSAT-2 ScanSAR data. Paper presented at the 2010 European Space Agency Living Planet Symposium, June 28 to July 2, 2010. Bergen, Norway. Abstract retrieved from <http://www.congex.nl/10a04/sessions/CXNL_10a04_873946.htm>
- Onstott, R.G. (1992). Chapter 5: SAR and Scatterometer Signatures of Sea Ice. In F.D. Carsey (Ed.), *Microwave Remote Sensing of Sea Ice*, AGU Geophysical Monograph 68, pp. 29-45. Washington: American Geophysical Union.
- Parkinson, C.L., and D.J. Cavalieri (2008). Arctic sea ice variability and trends, 1979-2006. *J. Geophys. Res.*, 113, C07003, doi:10.1029/2007JC04558.
- Perovich, D.K., and J.A. Richter-Menge (1994). Surface characteristics of lead ice. *Journal of Geophysical Research*, 99, C8, 16341-16350.

- Peterson, I.K., S.J. Prinsenber and J.S. Holladay (2006). Comparison of Helicopter-borne Measurement of Sea-Ice Properties with ENVISAT ASAR APP Data for Amundsen Gulf. *IEEE 2006 International Geoscience and Remote Sensing Symposium Proceedings*, 3651-3654.
- Peterson, I.K., S.J. Prinsenber, and J.S. Holladay (2008). Observations of sea ice thickness, surface roughness, and ice motion in Amundsen Gulf. *Journal of Geophysical Research*, 113, C06016, doi:10.1029/2007JC004456.
- Prinsenber, S.J., I.K. Peterson, and J.S. Holladay (1996). Comparison of Airborne Electromagnetic Ice Thickness Data with NOAA/AVHRR and ERS-1/SAR Images. *Atmosphere-Ocean*, 34, 1, 185-205.
- Prinsenber, S.J., J.S. Holladay and J. Lee (2002). Measuring ice thickness with EISFlow™, a fixed-mounted helicopter electromagnetic-laser system. *Proceedings of the 12th (2002) International Offshore and Polar Engineering Conference*, 1, 737-740.
- Prinsenber, S.J., I.K. Peterson, and J.S. Holladay (2008). Measuring the thicknesses of the freshwater-layer plume and sea ice in the land-fast region of the Mackenzie Delta using helicopter-borne sensors. *Journal of Marine Systems*, 74, 783-793.
- Ramsay, B., T. Hirose, M. Manore, J. Falkingham, R. Gale, D. Barber et al. (1993). Potential of RADARSAT for Sea Ice Applications. *Canadian Journal of Remote Sensing*, 19, 4, 352-362.
- Ramsay, B., D. Flett, H.S. Andersen, R. Gill, S. Nghiem and C. Bertoia (2004). Preparation for the operational use of RADARSAT-2 for ice monitoring. *Canadian Journal of Remote Sensing*, 30, 3, 415-423.

- Raney, R.K., and J.C. Falkingham (1994). RADARSAT and operational ice information. In S. Hayking, E.O. Lewis, R.K. Raney and J.R. Rossiter (Eds.) *Remote Sensing of Sea Ice and Icebergs*, pp. 611-658. New York: John Wiley & Sons, Inc.
- Riggs, G. A., D.K. Hall and S. A. Ackerman (1999). Sea Ice Extent and Classification Mapping with the Moderate Resolution Imaging Spectroradiometer Airborne Simulator. *Remote Sensing of the Environment*, 68, 2, 152-163.
- Rignot, E.R., and M.R. Drinkwater (1994). Winter sea-ice mapping from multi-parameter synthetic-aperture radar data. *Journal of Glaciology*, 40, 134, 31-45.
- Rignot, E., R. Chellappa and P. Dubois (1992). Unsupervised Segmentation of Polarimetric SAR Data Using the Covariance Matrix. *IEEE Transactions on Geoscience and Remote Sensing*, 30, 4, 697-705.
- Scheuchl, B., and I. Cumming (2005). Analysis of the Influence of NESZ Variations on Cross-Polarized Signatures of Sea Ice. *IEEE 2005 International Geoscience and Remote Sensing Symposium Proceedings*, 7, 5157-5160.
- Scheuchl, B., R. Caves, I. Cummings and G. Staples (2001). Automated Sea Ice Classification Using Spaceborne Polarimetric SAR Data. *IEEE 2001 International Geoscience and Remote Sensing Symposium Proceedings*, 7, 3117-3119.
- Scheuchl, B., D. Flett, R. Caves and I. Cumming (2004a). Potential of RADARSAT-2 data for operational sea ice monitoring. *Canadian Journal of Remote Sensing*, 30, 3, 448-461.
- Scheuchl, B., R. Caves, D. Flett, R. De Abreu, M. Arkett and I. Cumming (2004b). The potential of Cross-polarization information for operational sea ice monitoring. In Proceedings of the 2004 *Envisat Symposium*, September 6-10, 2004. Salzburg, Austria.

- Scheuchl, B., R. Caves, D. Flett, R. De Abreu, M. Arkett and I. Cumming (2004c). ENVISAT ASAR AP Data for Operational Sea Ice Monitoring. *IEEE 2004 International Geoscience and Remote Sensing Symposium Proceedings*, 3, 2142-2145.
- Serreze, M., and R. Barry (2005). *The Arctic Climate System*. Cambridge: Cambridge University Press.
- Serreze, M.C., A.P. Barrett, J.C. Stroeve, D.N. Kindig and M.M. Holland (2009). The emergence of surface-based Arctic amplification. *The Cryosphere*, 3, 11-19.
- Shokr, M.E., L.J. Wilson and D.L. Surdu-Miller (1995). Effect of Radar Parameters on Sea Ice Tonal and Textural Signatures Using Multi-Frequency Polarimetric SAR data. *Photogrammetric Engineering & Remote Sensing*, 61, 12, 1463-1473.
- Skriver, H., and L.T. Pedersen (1995). Polarimetric Signatures of Sea Ice in the Greenland Sea. *IEEE 1995 International Geoscience and Remote Sensing Symposium Proceedings*, 3, 1792-1794.
- Stirling, I., and C.L. Parkinson (2006). Possible effects of climate warming on selected populations of polar bears (*Ursus maritimus*) in the Canadian Arctic. *Arctic*, 59, 3, 261-275.
- Stroeve, J., M.M. Holland, W. Meier, T. Schambos and M. Serreze (2007). Arctic sea ice decline: Faster than forecast. *Geophys. Res. Letters*, 34, L09501, doi: 10.1029/2007GL029703.
- Thomsen, B.B., S.V. Nghiem and R. Kwok (1998). Polarimetric C-band SAR observations of Sea Ice in the Greenland Sea. *IEEE 1998 International Geoscience and Remote Sensing Symposium Proceedings*, 5, 2502-2504.
- Vachon, P.W., and J. Wolfe (2010). A SAR-Derived Wind Speed Model for C-band Cross-Polarized Ocean Backscatter. Paper presented at the 44th Annual CMOS Congress, May 31 to June 4, 2010.

- Ottawa, Canada. Abstract retrieved from
<https://www1.cmos.ca/abstracts/abstract_print_view.asp?absId=3740>
- Wadhams, P. (2000). *Ice In The Ocean*. London: Gordon and Breach Science Publishers.
- WMO (1970). WMO Sea-Ice Nomenclature. WMO-No. 259. Geneva: World Meteorological Organization.
- WMO (1989). WMO Sea-Ice Nomenclature, Supplement No. 5. WMO – No. 259. Geneva: World Meteorological Organization.
- WMO (2004). Ice Chart Colour Code Standard. WMO/TD-No. 1215. Geneva: World Meteorological Organization.
- WMO (2006). Sea-Ice Information Services in the World, Third Edition. Report WMO-No. 574. Geneva: World Meteorological Organization.
- Woodhouse, I.H. (2006). *Introduction to Microwave Remote Sensing*. Boca Raton: CRC Press, Taylor & Francis Group.
- Yu, P. (2009). Segmentation of RADARSAT-2 Dual-Polarization Sea Ice Imagery. Masters Thesis, University of Waterloo, Waterloo, Ontario, Canada. 98 pp.
- Yu, P., A.K. Qin and D.A. Clausi (submitted). Data fusion of dual-polarized RADARSAT-2 sea ice imagery. Submitted to *IEEE Transactions on Geoscience and Remote Sensing*.